

The Pennsylvania State University

The Graduate School

Department of Chemistry

**LIPID CHARACTERIZATION WITH TIME-OF-FLIGHT SECONDARY ION
MASS SPECTROMETRY (TOF-SIMS)**

A Dissertation in

Chemistry

by

Melissa Kathleen Passarelli

Submitted in Partial Fulfillment
of the Requirements
for the Degree of

Doctor of Philosophy

December 2011

The dissertation of Melissa K. Passarelli was reviewed and approved* by the following:

Nicholas Winograd
Evan Pugh Professor of Chemistry
Dissertation Advisor
Chair of Committee

Barbara J. Garrison
Head, Department of Chemistry
Shapiro Professor of Chemistry

T. C. Michael Chung
Professor of Material Science and Engineering

Miriam Freedman
Assistant Professor of Chemistry

*Signatures are on file in the Graduate School

Abstract

The normal function of a cell and tissue depends upon an elaborate series of interconnected biochemical interactions and reactions. Lipids, the main component of cell membranes, not only provide structural support, but also participate directly in complex cellular chemistry. As a result, secondary ion mass spectrometry (SIMS), an analytical technique capable of providing information on the chemical composition and spatial distribution of these molecules, will be a powerful tool for elucidating complex biochemical processes.

In this thesis, cluster SIMS is used to map lipid distributions in a cellular and a tissue model system. SIMS is an established technique in the field of lipid imaging. In Chapter 1, the successful applications of SIMS in lipid-based investigation are reviewed and the challenges associated with the technique are discussed. The basic principles of SIMS and design of the QSTAR mass spectrometer are discussed in Chapter 2. Also, recent instrument developments to improve the analytical power of the SIMS technique are discussed. The C₆₀-QSTAR instrument combines the advantages associated with cluster ion sources, continuous ion sources and tandem MS capabilities. This ability of this instrument to analyze lipids is examined in Chapter 3. Specifically, the ability to assist with *in situ* lipid identification and issues plaguing quantification efforts are discussed. In Chapter 4 and 5 the lipid profiles and distribution of lipids across the surface of normal functioning tissues and cells are characterized. In addition, the chemical composition and distribution of lipids in a diseased brain tissue after a traumatic brain injury are discussed in Chapter 5. The future direction of the technique in

the analysis of lipids is discussed in Chapter 6. The development of additional protocols aimed toward improving lipid-related molecular ion sensitivity, such as cryogenic sample preparation techniques and molecular depth profiling are illustrated with preliminary data.

TABLE OF CONTENTS

LIST OF FIGURES	viii
LIST OF TABLES.....	xiii
ACKNOWLEDGEMENTS.....	xiv
Chapter 1 Lipid Imaging with Time-of-Flight Secondary Ion Mass Spectrometry (ToF-SIMS).....	1
Abstract:	1
1.1 Introduction.....	2
1.2. Sample preparation	4
1.2.1 Cryofixation	5
1.2.2. Cryosectioning and freeze-drying	5
1.2.3. Frozen hydration method	6
1.3. Modes of operation and instrumentation.....	9
1.3.1. Cluster ion sources	11
1.4. Tissue imaging experiments.....	13
1.5. Single cell imaging experiments.....	21
1.6. Sensitivity issues.....	24
1.7. Dynamic SIMS.....	30
1.8. Challenges associated with the SIMS analysis of lipids	31
1.9. Recent developments in instrumentation	33
1.10. Conclusions.....	39
1.11. References.....	40
Chapter 2 C ₆₀ -QSTAR Instrument Development	49
Abstract:	49
2.1. Introduction.....	50
2.1.1 Fluence	51
2.1.2. Sputtering and ionization theory	52
2.1.3 Secondary electrons.....	53
2.1.4. Secondary ions	53
2.1.5. ToF mass analyzers	55
2.1.6. Secondary ion detection	56
2.1.7. Projectiles.....	56
2.1.8. Cluster ions.....	57
2.2. The Basic Instrument Design of the QSTAR-XL	58
2.2.1 Differential pumping and collisional cooling.....	58
2.3. Interfacing C ₆₀ SIMS and a QSTAR XL commercial mass spectrometer	60
2.3.1. Orthogonal ToF and duty cycles	62
2.3.2. Ion transmission	63

2.3.3. Mass range.....	64
2.3.4. Tandem MS analyses	65
2.4. SIMS-based Imaging Mass Spectrometry.....	67
2.4 Improvements.....	68
2.4.1 Focusing the ion beam using rastering plates and an SED.....	68
2.4.2. Imaging Software Improvements	70
2.5. Conclusions.....	74
2.6. References.....	75
Chapter 3 <i>In Situ</i> Identification of Glycerophospholipids with the C ₆₀ -QSTAR	
Instrument	77
Abstract:	77
3.1. Introduction.....	78
3.2. Experimental	84
3.2.1. Materials.....	84
3.3. Results and discussion	86
3.3.1. Identification	86
3.3.1.1. Standard lipids spectra: positive tandem MS	86
3.3.1.2. Standard lipids spectra: negative tandem MS	89
3.3.1.3. Standard lipids spectra: salt adducts tandem MS	90
3.3.1.4. Thin Film Analysis.....	94
3.3.2. Ion Abundance and Quantification.....	95
3.4. Conclusions.....	98
3.5. Reference	99
Chapter 4 The Characterization of Lipid Directly off the Surface of Tissue with Cluster SIMS Imaging and Tandem MS analyses.....	101
Abstract:	101
4.1 Introduction.....	102
4.2 Methods/ Procedures.....	104
4.2.1. Materials.....	104
4.2.2. Matrix application	105
4.2.3. Instrumentation.....	105
4.3.0 Results and Discussion.....	106
4.3.1. High resolution imaging.....	106
4.3.2. The Analysis of lipids on tissue using Hybrid QSTAR instrument	109
4.3.3. Lipid distributions	109
4.3.4. Lipid chemistry in the white matter	112
4.3.5. Lipid chemistry in the gray matter	116
4.3.6. Lipid chemistry in the ventricles	119
4.3.7. PCA analysis	119
4.3.8 The effects of matrix on the image and spectral quality of SIMS analysis	124
4.4. Conclusions.....	127
4.5. References.....	128
Chapter 5 Characterization Lipids on a cell model with Imaging Cluster SIMS.....	130

Abstract	130
5.1. Introduction.....	131
5.2 Experimental	134
5.2.1. Sample preparation.....	134
5.2.2. Instrumentation.....	134
5.3. Results and discussion	135
5.3.1 Lipid identification.....	135
5.3.2. Lipid imaging with C ₆₀ -SIMS	142
5.4. Conclusions.....	146
5.5. Reference	147
Chapter 6 Conclusions and Future Directions of C ₆₀ -SIMS	149
Abstract:	149
6.1. Depth profiling.....	149
6.2. Cold stage for the C ₆₀ -QSTAR instrument	153
6.3. References.....	160
Appendix Glycerophospholipid Reference Spectra	161

LIST OF FIGURES

- Figure 1.1. The diagram describes overlaps and unique areas of MALDI, DESI and SIMS. Lipids are detectable for all three methodologies.4
- Figure 1.2. Bird’s eye view (left) and profile (right) of freeze fracturing device in the closed position (bottom) before a fracture and opened (top) position after a fracture. (Note: Yellow areas = silicon shards) ⁴⁴8
- Figure 1.3. Sagittal section of rat brain. (Top row, left to right) SIMS images obtained in the positive mode—phosphocholine headgroup (m/z 184), cholesterol (m/z 385) and m/z 796.8—and optical image of the tissue. (bottom row: left to right) SIMS images obtained in the negative mode—Stearic (18:0) fatty acid fragment (m/z 283), vitamin E (m/z 429.3) and sulfoglycosphingolipid (sulfatide, d18:1/24:1)—and the overlay of these ions. [fatty acid (red), vitamin E (green) and sulfatide (blue)].⁶¹ 14
- Figure 1.4. Negative ToF-SIMS images of cerebellum tissue (a) summed pixel intensities of sulfatides from m/z 778.5 to 934.6 red (b) ion intensities of cholesterol at m/z 385 green and (c) overlay of panels a and b. Regions of the cerebellum are outlined; molecular layers (m), white matter (w) and the gray mater (g). ⁶⁶ 16
- Figure 1.5. Microscopy (DIC) image of a mating *tetrahymena thermophila* (a) and SIMS image depicting localizations of an ubiquitous organic ion at m/z 69 (C₅H₉, b). Lipid heterogeneities at the mating junction includes a depletion of phosphocholine (c) and an accumulation of 2-AEP (d). (Scale bar: 25 μm) ⁸⁸ 23
- Figure 1.6. SIMS images of a cultured neuron obtained from the superior cervical ganglia of a mouse. Ion contribution from the phosphocholine headgroup (m/z 206.1, m/z 224.1 and m/z 246.1) is distinguished from the SM headgroup (m/z 206.1) fragments.⁹³ 24
- Figure 1.7. 3D biochemical images of freeze-dried oocyte depicting phosphocholine signal from m/z 58, 86, 166, and 184 (a) and cholesterol signal at m/z 369 (d).⁹⁹ 27
- Figure 1.8. Image acquired with dynamic SIMS, illustrates the distribution of isotopically traceable monosaturated fatty acid, oleate, in a single 3T3F442A adipocyte ¹⁰⁶. The oleate is localized to the cell membrane and discrete lipid droplets inside the cell..... 31
- Figure 1.9. Schematic of the C₆₀⁺-QSTAR instrument shows how the commercial triple quadrupole orthogonal ToF mass spectrometer was interfaced with a C₆₀ ion source.¹¹⁰ 35
- Figure 1.10. Lipid profile obtained from a single neuron with SIMS (a) and from a compilation of neurons with MALDI (b). The tandem MS spectrum shows that m/z 709 and 184 are major fragments of m/z 768.5, the sodiated adduct of major lipid component m/z 746.5 (c). Optical image (d, left) and black and white SIMS total ion

image (d, right) of cultured aplysia neuron on silicon wafer (image size 2.00×4.75 mm). ¹⁰⁴	36
Figure 1.11. Schematic of Ionoptika J105 3D Chemical Imager (a) and close up diagram of time focusing buncher, collision cell for tandem MS acquisitions and ToF mass analyze (b). ¹⁰⁹	38
Figure 1.12. 3D biochemical images of frozen hydrated HeLa M cells depicting localizations of phosphocholine headgroup (m/z 184, green) on the cell membranes and adenine (m/z 136.1, red) localized to the nucleus obtained on the Ionoptika J105 3D Chemical Imager. ^{22, 111}	38
Figure 2.1. Sample stage and diagram demonstration the basic scheme of SIMS.....	54
Figure 2.2. An extension block was used to interface the 20 keV C_{60} ion gun and the QSTAR XL mass spectrometer. The insert shows the sample region in detail; the mosquito nose cone protects the ion beam from the high pressure in the sample region. ²⁰	61
Figure 2.3. The efficiency of the orthogonal injection process is captured in the duty cycle equation. The ion transmission of ions given a m/z maximum of 1 kDa, 2kDa, 5 kDa, 10 kDa and 40 kDa. The wider the mass range, the lower the relative transmission for a given ion. Due the instrumental dimentiosn of the QSTAR instrument, the maximum transmission is 25%.	62
Figure 2.4. ToF-MS spectrum of high mass CsI cluster (left) and bar graph showing the relative intensity of CsI clusters as a function of cluster size (right). A large range of $Cs(CsI)_n$ clusters were detected from $n=0$ at m/z 132 to $n = 151$ at m/z 39,364.....	65
Figure 2.5. The tandem MS spectra of a lipid, 1,2-dihexadecanoyl-sn-glycero-3-phosphate (PA(16:0/16:0)) obtained using C_{60} -QSTAR (left) has the same signature peaks as the ESI-QTRAP acquired spectrum obtained from the Lipid MAPS spectral library (right). (CE= -30 volts).....	66
Figure 2.6. The photograph illustrates the orientation of the ion gun, quadrupoles, SED, MALDI laser and camera (left). An SEM image of a grid shows that the 20 keV C_{60}^+ ion source can be focused to 1.6 micron resolution (right).	68
Figure 2.7. SEM images of a grid at 5.0×10^{-4} , 1.0×10^{-4} and 5.0×10^{-3} torr in the Q0 region (top) and the sample region (bottom). Pressures in the sample region needed for collisional cooling is not conducive to ion beam focusing efforts. However, the sweeping gas, injected into the Q_0 , had little effect on the ion beam's focus.	70
Figure 2.8. Stage rastering patterns available in the upgraded oMALDI server 5.1 software. In the spot mode, the stage is moved in a serpentine pattern and the beam is turned off while the stage is moving to the next pixel. In the rastering mode, line scans acquired by a dc beam are stacked vertically to produce an image. The new	

- imaging pattern improved the instrument lateral resolution and reduced acquisition times by taking advantage of the instrument's dc ion beam capabilities. 71
- Figure 2.9. The ToF-MS image of 200 mesh finder grid (pitch= bar and square = 127 μm) coated in cesium iodide (green, m/z 132) on a indium foil (blue, m/z 114.9) (top left) had a measured lateral resolution of 6.7 microns (top right). Cellular imaging is feasible at this resolution (bottom). The optical image of the freeze dried cheek cells was obtained under 20x magnification (left). The high resolution ToF-MS image of unknown compound at m/z 165 was localized to the cells (right). 73
- Figure 3.1. The diagram illustrates the basic composition of glycerophospholipids. Three major structural components include the headgroup (green), glycerol-fatty acid linkage (blue) and fatty acid composition (purple). The fatty acid moiety can vary in chain length, as well as in the number and location of double bonds. 80
- Figure 3.2. Characteristic SIMS Fragment Peaks for Various Lipids.¹ 82
- Figure 3.3. Precursor ion scan of the phosphocholine headgroup, m/z 184, isolates the glycerophosphocholine species from other species in complex lipid mixture. 88
- Figure 3.4. Tandem MS spectrum of sodiated lipid adduct GPCho (16:0/16:0) [M] in the positive ion mode. The spectrum provides information about the headgroup (m/z 184 and 86) and fatty acid constituent (m/z 577.5 and 599.5). The spectra also reveals a high-mass fragment associated with the loss of tri-methylamine [M + alkali metal – TMA]⁺. 93
- Figure 3.5. Structure, image and tandem MS spectra of PS(16:0/18:2) and PC(16:0/18:1) films. In the tandem MS spectra of m/z 760.5, the unique fragmentation characteristics of glycerophosphoserine (m/z 575.5) and glycerophosphocholine (m/z 184) allowed for the separation of the isobaric lipids. The overlaid image of fragment m/z 575.5 (green) and m/z 184 (blue) shows the spatial separation of the two isobaric lipids. 95
- Figure 3.6. Tandem MS spectra were obtained at various collision energies; the variation in integral count of the main fragments— m/z 551 for GPEthn(16:0/16:0), m/z 184 for GPCho(16:0/16:0) and m/z 713 for potassiated GPCho(16:0/16:0)—is plotted. 97
- Figure 4.1. ToF-SIMS image of phosphocholine signal at m/z 184 across the surface of a coronal rat brain section. Three images at varying lateral resolutions were obtained; each pixel in the whole tissue images are $50 \mu\text{m}^2$ (8.2 x 11.6 mm) (a), the hippocampus region image are $10 \mu\text{m}$ (4.5 mm x 2 mm) (b) and the pixels in the image of the corpus collosium are $10 \mu\text{m} \times 1.5 \mu\text{m}$ (500 $\mu\text{m} \times 350 \mu\text{m}$) (c). 108
- Figure 4.2. MeSIMS images of galactoceramides in the coronal brain tissue. 113
- Figure 4.3. The tandem MS spectrum reveals that more than one lipid is detected at m/z 850.5. The peak at m/z 486, which is 2 Da mass units higher than the m/z 484 peak that represent galactoceramides with d18:1 backbone, confirms the presence of

- galactocerebrosides with sphinanine (d18:0) backbones. The lipid structures were created using Chemdraw 12.0 software. 114
- Figure 4.4. MeSIMS image overlaying Cer(18:1/18:0) at m/z 548.5 (red), SM(d18:1/18:0) at m/z 694.5 (blue) and Cer(d18:1/22:0) at m/z 604.4 (green). 118
- Figure 4.5. Principle component analysis of the lipid region obtained from a native tissue analyzed with ToF-SIMS (Loading 5, 0.24 percent variance). In this analysis, the chemical signature of the gray matter (positive loadings) was separated from the chemical signature of the white matter (negative loadings). In general, the gray matter contained glycerophospholipids related species and the white matter contained galactoceramide related lipid species. For clarity, peaks with relative intensity less than 0.001 in both the positive and negative direction were filtered out. 121
- Figure 4.6. Principle component analysis of the isolated third ventricle region obtained from the matrix-coated tissue analyzed with ToF-SIMS (Loading 2, 4.5 % variance). Peaks in the positive regime are localized to the ventricle region and have been identified as ceramides. 123
- Figure 4.7. The SIMS (blue) and MeSIMS (purple) spectra of the lipid region have the same lipid peaks with similar relative intensities for the glycerophosphocholine-related peaks. However, the molecular ion intensity of galactoceramides related peaks at m/z 810, 822 and 850 are enhanced in the presence of the matrix (circle). 124
- Figure 4.8. ToF-SIMS image of a coronal rat brain section with alpha-cyano matrix, an overlay of lipid fragment phosphocholine at m/z 184 (black and white) and sodiated galactoceramide at m/z 850.5. Tissue section 16.4 x 11.6 mm 126
- Figure 5.1. The topographical distribution of identified neurons in the abdominal ganglia as view from the dorsal surface is illustrated. The R2 neuron is the largest cell in the right hemisphere (red), its axons extend into the right connective tissue and the branchial nerve. 133
- Figure 5.2. ToF-SIMS spectrum (A) obtained from a single aplysia neuron and MALDI spectrum (B) taken from a collection of aplysia neurons 136
- Figure 5.3. Tandem MS spectra of the protonated molecular ion, sodiated adducted and high mass fragment of the major membrane lipid of the R2 neuron. Based on the three spectra that lipid can be identifies as GPCho(16:0 e/ 18:1). Also the structure of GPCho(16:0 e/ 18:1) with locations of fragmentation marked. 139
- Figure 5.4. The glycerophosphocholine fractions was separated from the other lipids in the lipid extract using normal phase LC/MS/MS, retention time was 27 minutes. Tandem MS spectrum of the lipid acetate adduct at m/z 804 was obtained in the negative ion mode. The higher ratio of the 281.2 (18:1 fatty acid) 140
- Figure 5.5. ToF-SIMS images of an isolated aplysia R2 neuron from the abdominal ganglia are examined. The optical(a) image was taken at 20 x magnificantion with a dissecting microscope. The SIMS total ion image is also shown, the soma is

approximately 450 x 380 micron (l x w) in size. (b). The summed intensity of all the peaks related to the newly identified ether lipid, GPCho(16e:0/18:1), were overlaid using MatLab (d). Unknown fragment ion at m/z 128 was homogenously distributed across the surface of the neurons soma and axon (blue, d-f). The distribution of cholesterol at m/z 369.3 (d), Vitamin E at 430.3 (e) and high mass fragment of GPCho(16:0e/18:1) at m/z 709.5 (f) was overlaid with the m/z 128 species using TissueView. In the bottom row are the ToF-SIMS images showing the distribution of the lipid headgroup's for GPEthn at m/z 142(g), GPCho at m/z 184 (h) and CAEPn at m/z 124(i)..... 144

- Figure 6.1. The molecular depth profile analysis of trehalose. The intensity of the molecular ion of trehalose at m/z 325 and a silicon peak at m/z 28 are plotted as a function of C_{60}^+ ion fluence. Based on atomic force microscope measurements, the crater's dimensions were approximately 300 μm x 300 μm x 240 nm, (length x width x depth). 152
- Figure 6.2. Molecular depth profile of Trehalose film on a silicon wafer. The intensity of the sodiated-molecular ion of trehalose at m/z 365 and a silicon oxide peak at m/z 87 (Si_2O_2^+) are plotted as a function of primary ion fluence. An atomic force microscope (AFM) was used to measure the dimensions of the crater produced during the analysis. The film was approximately 44.8 μm x 48.2 μm x 171.8 nm, 5 pA beam current..... 152
- Figure 6.3. Molecular depth profile of a thin film of lipid standard DPPC at room temperature and at cryogenic temperatures. The secondary ion yields of the GPCho(32:0) protonated molecular ion was higher for films examined under cryogenic conditions compared to a film analyzed at room temperature for both static and dynamic analyzes. 154
- Figure 6.4. The schematic depicts the prototype cold stage for the C_{60} -QSTAR instrument. The sample is cooled via a copper cold finger that is inserted into the back of the sample stage. In this device, nitrogen gas (initially at room temperature) is cooled as it travels through a coil of copper tubing submerged in a dewar of liquid nitrogen. After the nitrogen is cooled it travels to the cold finger attached to the stage. 155
- Figure 6.5. The prototype C_{60} -QSTAR cold stage was tested using a thin film of GPCho (16:0/16:0). The temperature and the integral intensity of the GPCho (16:0/16:0) protonated molecular ion peak at m/z 734.5 were recorded as a function of time. In approximately 1 minute, the stage temperature was reduced by 40 $^\circ\text{C}$ and the intensity of GPCho (16:0/16:0) was more than doubled. 156
- Figure 6.6. Preliminary data obtained analyzing a tissue section using the prototype C_{60} -QSTAR cold stage. The left hemisphere was acquired at room temperature; the right hemisphere was acquired at temperatures below 25 C. Below room temperature, the cholesterol signal disappeared..... 158

LIST OF TABLES

Table 1.1. Lipid species –protonated ions, adducts and pseudomolecular ions— identified in various mammalian tissue sections using ToF-SIMS and organized using the lipid classification system established by the Lipid MAPS consortium	18
Table 1.2. Lipid species identified from bacterial and microbial colonies using ToF-SIMS and organized using the lipid classification system established by the Lipid MAPS consortium.....	20
Table 1.3. Lipid species –protonated ions, adducts, pseudomolecular ions and fragments—identified in various mammalian and non-mammalian cell lines using ToF-SIMS and organized using the lipid classification system established by the Lipid MAPS consortium.....	28
Table 3.1. Characteristic fragment peaks of lipid species from the major sub- classes of glycerophospholipids, GPA, GPCho, GPEthn, GPSer, GPGro and GPIs obtained using positive ion mode tandem MS. All of the lipids with the expectation of GPCho experience the neutral loss of the headgroup moiety.	87
Table 3.2. Characteristic fragment peaks of lipid species from the major sub- classes of glycerophospholipids (GPA, GPCho, GPEthn, GPSer, GPGro and GPIs) obtained using negative ion mode tandem MS.	90
Table 3.3. Characteristic fragment peaks of sodiated adducted lipid species from the major sub-classes of glycerophospholipids (GPCho, GPSer, GPGro and GPA) obtained using positive ion mode tandem MS.	92
Table 4.1. Lipid species detected from the surface of a coronal tissue section using SIMS.	110
Table 5.1. Summary of lipids found on the surface of a single neuron from an <i>aplysia californica</i>	136

ACKNOWLEDGEMENTS

I would like to thank my advisor, Professor Nicholas Winograd, for all his guidance throughout the years. Also I am grateful to my dissertation committee Professor Barbara Garrison, Professor Mike T. C. Chung, Professor Andrew Ewing and Professor Miriam Freedman. I would like to thank all the Winograd group members past and present; especially Chris “Grimey” Szakal, my officemates, Anita Durairaj and Jung-Hwan Kim, and classmates Dan Mao, Daniel Brenes and Andrew Kucher. A special thanks to Sabrina Glasgow for all her help.

A special thanks to Alexandre (Sasha) Loboda from Applied Biosystems/ Sciex for this work would not be possible without his expertise on the QSTAR XL instrument. I would also like to thank Julie Wingate from Applied Biosystems/ Sciex for initiating the collaboration and providing the instrument used in these investigations. I would also like to thank Rowland Hill and Paul Blankensop from Ionoptika for support with the ion gun. I would also like to thank the Lipid MAPS community for funding and insight on lipid biochemistry, especially Professor Bob Murphy and Joe Hankin at the University of Colorado, Denver. I would also like to thank my undergraduate research advisors, Professor Mary Carroll and Ann Anderson and the Union College aerogel team for initiating my path in the research field.

A number of colleagues and collaborators have contributed to the completion of this thesis; including Alex Henderson for his PCA analysis scripts and assistance with MATLAB, Missy Hazen at the PSU Electron Microscopy facility for

training on the cryomicrotome and Michael Heine for instruction on animal dissections.

I would also like to acknowledge Rodney Kreuter, Jim Miller and Larry Johns.

I also thank Josh Antoline and Michael Ibele for the countless lunches and laughs at the Waffleshop. I would like to thank my family, siblings Michael and Lisa and babies Brady and Toby too. Most importantly, I would like to thank my parents Kathleen and Nicholas Passarelli for always encouraging me to, “go for broke”. I love and miss you always.

Chapter 1

Lipid Imaging with Time-of-Flight Secondary Ion Mass Spectrometry (ToF-SIMS)

This chapter has been adapted from the review paper, Lipid Imaging with Time-of-Flight Secondary Ion Mass Spectrometry (ToF-SIMS) by M. K. Passarelli and N. Winograd, published in *Biochimica et Biophysica Acta*, June 2011.

Abstract:

Fundamental advances in secondary ion mass spectrometry (SIMS) now allow for the examination and characterization of lipids directly from biological materials. The successful application of SIMS-based imaging in the investigation of lipids directly from tissue and cells are demonstrated. Common complications and technical pitfalls are discussed. In this chapter, we examine the use of cluster ion sources and cryogenically compatible sample handling for improved ion yields and to expand the application potential of SIMS. Methodological improvements, including pre-treating the sample to improve ion yields and protocol development for 3-dimensional analyses (i.e. molecular depth profiling), are also included in this discussion. New high performance SIMS instruments showcasing the most advanced instrumental developments, including tandem MS capabilities and continuous ion beam compatibility, are described and the future direction for SIMS in lipid imaging is evaluated.

1.1 Introduction

Time-of-flight secondary ion mass spectrometry (ToF-SIMS) is a surface analysis technique capable of producing high resolution chemical images and is a well-suited platform for the analysis of lipids directly from the surface of biological materials. With this technique the sample surface is bombarded with a focused high energy primary ion beam (1-40 keV), causing desorption of secondary ions. A mass spectrometry-based image is then produced by rastering the ion beam across the sample surface. The high lateral resolution and sensitivity attributed to SIMS allows for the detection of lipid molecules at the nanometer scale and at attomolar concentrations.^{1,2} The ToF detection scheme also offers parallel detection of multiple lipid species, ideal for the analysis of complex biological samples.

In addition to ToF- SIMS, matrix-assisted laser desorption ionization (MALDI) and desorption electrospray ionization (DESI) are imaging mass spectrometry (IMS) techniques utilized in the analysis of biological materials. Like ToF-SIMS, MALDI³⁻⁶ and DESI⁷⁻¹⁸ have proven to be particularly successful in the detection and analysis of lipids. The pitfalls, advantages and successful applications of each technique are reviewed in detail elsewhere and are only briefly discussed in this review.¹⁹⁻²⁴ In terms of spatial resolution, MALDI and DESI are capable of resolving features as small as 20 μm and 100 μm , respectively. In many cases for tissue imaging, ToF-SIMS offers a complementary perspective to these alternative IMS techniques since the lateral resolution of ToF-SIMS can be below 1 micron (see Figure 1.1). Various efforts have been made to improve the spatial resolution of MALDI imaging, including

oversampling,²⁵ laser modulation²⁶ (i.e. smart beam technology) and solvent-free sublimation matrix application techniques.²⁷ Despite these efforts, the technique has not achieved the spatial resolution of ToF-SIMS.

In terms of chemical specificity, however, MALDI and DESI techniques cover a broader range of biomolecules—including proteins, peptides and nucleotides. The ability to detect proteins and peptides directly correlates to the techniques' success in bio-analytical chemistry and biomedicine. Currently, MALDI is the prominent IMS method utilized in medical and bioanalytical research with applications in clinical diagnostics,²⁸⁻³² pharmaceutical research³³ and biomarker discovery.³⁴ Although proteins represent only 20 % (by weight) of a cell, proteomics has traditionally been at the heart of biomedical investigations. However, a recent trend among system biologists from proteomics to lipidomics³⁵ raises the question: Will SIMS, with its higher spatial resolution and equivalent sensitivity to lipids, be more readily accepted into the biochemical and biomedical community?

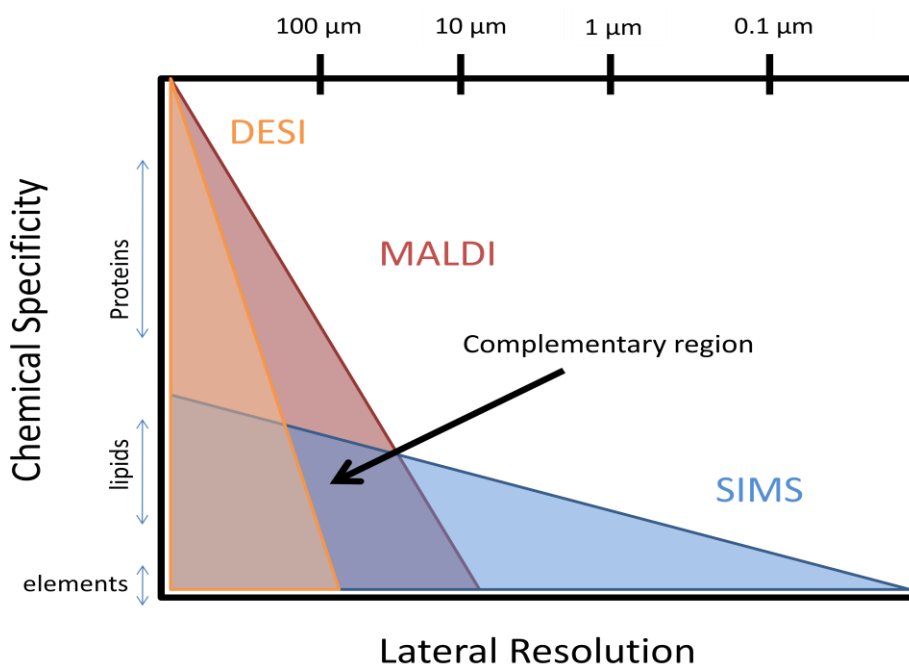


Figure 1.1. The diagram describes overlaps and unique areas of MALDI, DESI and SIMS. Lipids are detectable for all three methodologies.

1.2. Sample preparation

Well-developed sample preparation techniques are crucial for successful ToF-SIMS investigations. The major challenge in proper sample preparation is interfacing the biological samples with biologically unfavorable vacuum conditions while preserving chemical and spatial integrity. A variety of protocols for both tissue and cellular samples have been established; the most frequently employed procedures are reviewed below. In general these techniques contain steps in which the tissue samples are fixed, sectioned, mounted, and dried; a majority of these protocols were derived from

established histological sample preparation techniques. Other techniques include ones where cellular samples are fixed and analyzed in a frozen hydrated state.

1.2.1 Cryofixation

To minimize sample degradation, fixation efforts are required immediately after the sample has been extracted from the specimen or culture media. Traditional chemical-based fixation techniques should be avoided especially for lipid-based analyzes; the consequences of such procedures were examined by Malm and co-workers.³⁶ Instead, plunge freezing, a cryogenic-based fixation technique, is employed to preserve the integrity of the sample. In plunge freezing, the sample is submerged in liquid propane (85 K) or ethane (89 K) and subsequently transferred and stored in liquid nitrogen (77 K). In this method, the freezing process is so rapid that the sample's water content is converted into amorphous ice. This is advantageous since the formation of ice crystals responsible molecular and morphological displacement is avoided. Compared to chemical treatments, plunge-frozen samples produce higher phospholipid molecular-ion signals and retain the native distribution of diffusible ions, such as Na^+ , K^+ and Ca^+ .³⁶

1.2.2. Cryosectioning and freeze-drying

After freeze-fixation, tissue samples are typically sectioned, mounted, and freeze-dried before analysis. During cryosectioning, the sample is brought to -20°C and sliced into 10-50 μm thick sections. Tissue sections are commonly thaw-mounted to a

substrate—typically a conductive indium tin oxide (ITO) coated glass microscope slides or a metal sample plate. Occasionally, a cryoprotectant agent, (e.g. optimal cutting temperature (OCT), 2.3 M sucrose and 10% gelatin) is incorporated into tissues before cryofixation to preserve vitrification at high temperature.

After mounting, tissue sections are freeze-dried. In this process the sample's water content is slowly sublimated under vacuum conditions (mbar); subsequently, the dehydrated samples are brought to room temperature for analysis. It is not clear how this procedure influences the structure of the tissue. During the drying procedure the loss of water undoubtedly leads to some collapse of the material. To improve the freeze drying process, Nygren and coworkers have reported the use of a high pressure freezing technique. Overall image resolution was improved using this freezing method compared to traditional freeze drying techniques.^{37,38} Although freeze drying is an acceptable procedure for the preparation of tissue samples, it is not suitable for micro-analyses or sub-cellular studies.

1.2.3. Frozen hydration method

Chandra and coworkers were the first to describe frozen hydrated sample protocols for the SIMS analysis of cells.^{39,40} Since then, frozen hydration sample preparation has become the gold standard for cell-based investigations.⁴¹ In this technique, cells are cryo-fixed via the freeze plunging method previously described and analyzed without drying. The samples are kept frozen with a liquid nitrogen cooled stage

throughout the analysis. Cell morphology and spatial integrity of diffusible molecules are maintained with this method.

Researchers have reported enhanced molecular ion signals for phospholipids when using frozen hydrated sample preparation techniques. The origin of this enhancement effect is twofold, with the signal increase coming from both an increase in the number of protons generated from the condensed water matrix and the reduced damage accumulation during depth profiling analyses. Under static conditions, studies reveal that a proton transfer between the water matrix and the lipid molecules is responsible for the enhanced phospholipid signals observed at cryogenic temperatures. During depth profiling, damage accumulation is responsible for reduced ion signals and degraded depth resolution at increased depths.⁴² Cooling the sample to liquid nitrogen temperatures has been found to reduce the damage accumulation. Studies performed by Piwowar and co-workers show that the molecular ion signal for 1,2-dipalmitoyl-sn-glycero-3-phosphocholine (DPPC) was enhanced by a factor of three when examined under cryogenic and dynamic conditions.⁴³

Contamination from ambient condensation, typically occurring during sample transfer, is a common complication associated with this frozen hydrated sample preparation method. To combat this, freeze etching and C_{60}^+ etching techniques have been employed to remove condensation.⁴¹ However, condensation contamination can be avoided altogether by employing freeze-fracturing techniques and preparing samples in controlled atmospheres (i.e. glove boxes). To freeze-fracture a sample, the hydrated cells are sandwiched and frozen between two silicon shards. Once in vacuum, the sandwich is fractured and fresh unperturbed cells are exposed to the surface for analysis. Recently,

Lanekoff and co-workers developed an *in situ* freeze fracture device for the analysis of frozen hydrated cells with ToF-SIMS (see Figure 1.2).⁴⁴ This spring-loaded mechanical device eliminates human and external influences during the freeze fracturing event and generates more consistent, reliable and reproducible fractures.

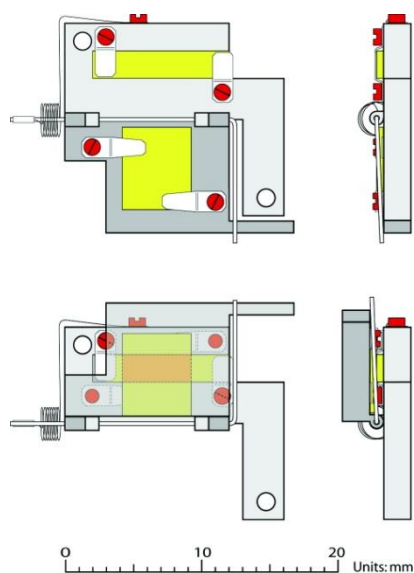


Figure 1.2. Bird's eye view (left) and profile (right) of freeze fracturing device in the closed position (bottom) before a fracture and opened (top) position after a fracture. (Note: Yellow areas = silicon shards)⁴⁴

Another common problem associated with *in situ* MS-analyses of tissues and other biological materials is the overwhelming presence of biological salts. In the lipid region, salt adducts contribute to isobaric interferences and impede quantification efforts by dividing a single lipid species into multiple channels. Protocols have been established to remove biological salts by washing tissue with various solvents.^{36,45,46}

The most successful and widely accepted washing solution is pH and osmolarity-balanced ammonium formate (pH = 7.4, concentration = 10 mM). Care should be taken since washing techniques may alter the lipid distribution, obscuring spatial information.

1.3. Modes of operation and instrumentation

In the field of SIMS there are two fundamental modes of operation based on the primary ion fluence termed static and dynamic. Static SIMS represents acquisitions with primary ion fluencies below 10^{12} ions/cm². In this mode, less than 1 % of surface molecules are perturbed, as a result, the probability of impacting the same area twice is extremely low. Intact molecular ion species are typically observed under static conditions; as a result this mode of operation is often used in lipid investigations. In dynamic mode, high fluence bombardment erodes the sample's surface and chemical information is acquired as a function of depth. The dynamic mode is highly destructive, which limits the analyses to elemental and isotopic information. Based on the mode of operation, there are two types of SIMS instruments commercially available: instruments designed for static acquisitions and those designed for dynamic acquisitions.

Static SIMS instruments typically employ pulsed primary ion sources and ToF mass analyzers. For *in situ* lipid analysis, the parallel detection associated with the ToF mass analyzer is beneficial for probing complex biological samples with multiple lipid species. ToF-SIMS instruments are able to obtain chemical and spatial information as a function of depth; however, they are unable to collect data during the sputtering

process. Alternatively, depth profiles are obtained by continuously alternating between data acquisition and sputtering cycles, resulting in low duty cycle depth profiles.

High fluence instruments typically employ continuous primary ion beams and scanning-based mass analyzers. The continuous generation and detection of secondary ions results in efficient, high duty cycle acquisitions. Although instruments with scanning-based mass analyzers are able to continuously monitor secondary ion generation during sputtering, they are limited in the number of ions detected per depth profile.

Only a few SIMS mass spectrometers are available commercially. Static instruments with reflectron ToF mass analyzers are available from IonToF GmbH (i.e. the ToF-SIMS IV and ToF-SIMS 300/300R instruments) and Kore Technology Ltd (i.e. the SurfaceSeer and Bio-ToF instruments). Also available commercially is a static ToF-SIMS instrument from Physical Electronic (i.e. the Trift V nanoToF), which employs three electrostatic analyzers to accelerate secondary ions into a linear ToF mass analyzer. Cameca SAS has a variety of dynamic SIMS instruments, including a line of ion microscope (IMS 7F, IMS 1270/1280) and NanoSIMS 50/50 L instruments, which employ a double-focusing sector, consisting of an electrostatic sector for filtering and a magnetic sector for mass analysis.

Newly developed SIMS instruments, the C_{60}^+ -QSTAR and J105 (Ionoptika Ltd.), combine the advantages associated with a continuous primary ion beam and ToF mass analyzers. In addition, unlike any of the aforementioned instruments, these new instruments are capable of performing tandem MS analyses. Design and operational

advantages associated with both instruments are discussed in detail in Section 9 of this review.

1.3.1. Cluster ion sources

Early ToF-SIMS studies focused on experiments in inorganic chemistry and material science, where the technique was successfully applied to semiconductors^{47,48} and polymers.^{49,50} The analyses of organic materials with these early generation-SIMS instruments were less successful, as they often suffered from low sensitivity and a high degree of molecular fragmentation. As a result, the analysis of intact lipid molecules was limited to lipids protected in liquid matrices (e.g., liquid SIMS and the analogous technique of fast atom bombardment (FAB)).⁵¹⁻⁵³ Fortunately, progress in instrumentation, particularly in the development of cluster ion sources, has made modern ToF-SIMS instruments more compatible with fragile and labile molecules.

The emergence of cluster ion sources— C_{60}^+ , Bi_3^+ , Au_3^+ and SF_5^+ —has drastically changed the direction of SIMS research and has ushered in a new era of biologically relevant studies.^{54,55} The bombardment dynamic associated with cluster projectiles is different than that of atomic projectiles. Cluster projectiles distribute the incident energy among the individual atoms in the cluster and dissociate upon impact with the sample's surface. Compared to the collision cascade of atomic projectiles, this new bombardment dynamic leads to higher sputter yields for intact organic molecular species. In addition, the incident energy of cluster projectiles are deposited closer to the surface, which reduces the physical and chemical damage cross section.^{56,57} These

features allow for increased molecular ion sensitivity and allow for the construction of 3-dimensional chemical images. In the analysis of lipids, the ability to detect intact molecular species spatially in 2 or 3 dimensions is an ability unique to cluster SIMS.

Ostrowski and co-workers experimentally measured the degree of molecular ion enhancement afforded by cluster ion sources for a select number of lipids commonly detected with SIMS.⁵⁸ In all cases, lipid molecular-ion signals were enhanced; although the degree of enhancement was not uniform among or within the various lipid classes. For instance, C_{60}^+ improved the ion yields of cholesterol and sulfatides by a factor of 70 and 10^3 compared to Ga bombardment, respectively.⁵⁸ In addition, the detection of glycerophospholipid molecular-ions was enhanced by 240- to 800- fold, with the degree of enhancement being dependent on the lipid's headgroup composition.

Due to the emergence of cluster sources, various intact lipids, including glycerophospholipids, cholesterol and vitamin E are routinely detected and identified in tissue. However, the ability to analyze single cells is still limited and very few intact lipid species from cells have been observed. Recent scientific advances in instrumentation and sample preparation protocols are pushing the limits of spatial resolution and sensitivity in order to expand the analytical capabilities of SIMS to a point where lipids can be routinely analyzed on a cellular and sub-cellular level.

1.4. Tissue imaging experiments

Rat brain sections, a well-established model system for tissue-based IMS studies, have been employed to illustrate the potential of ToF-SIMS imaging for lipid-based investigations. Sjovall and co-workers were the first to report a number of sulfoglycosphingolipids (sulfatides) and cholesterol in the white matter of a rat brain as well as glycerophospholipids molecules, specifically glycerphosphocholines (GPCho) and glycerophosphoinositols (GPIs), in the gray matter of a rat brain section using a Bi_3^+ source.^{59,60} More recently, Benabdellah and coworkers confirmed these findings while imaging a sagittally sliced rat brain section (see Figure 1.3).⁶¹ In addition to the variety of lipids identified in the sample, their analysis of this model system demonstrated the connection between spatial and chemical information allowing inferences to be made between anatomical features and physiological functions. For example, the most striking feature observed in the coronal brain sections was the large region of cholesterol (m/z 369.3 and 385.3) which correlated to the corpus callosum. The corpus callosum is a bundle of nerve fibers that bridges the right and left hemispheres of the brain. To ensure efficient electrical signal conduct across the corpus callosum, the neural fibers are coated with myelin sheath. The high level of cholesterol localized to this region confirms that it is an essential structural and biochemical component of the myelin. Overall, the corpus callosum is easily distinguished from the cerebral cortex and other regions of the brain in SIMS images based on its distinct chemical composition.

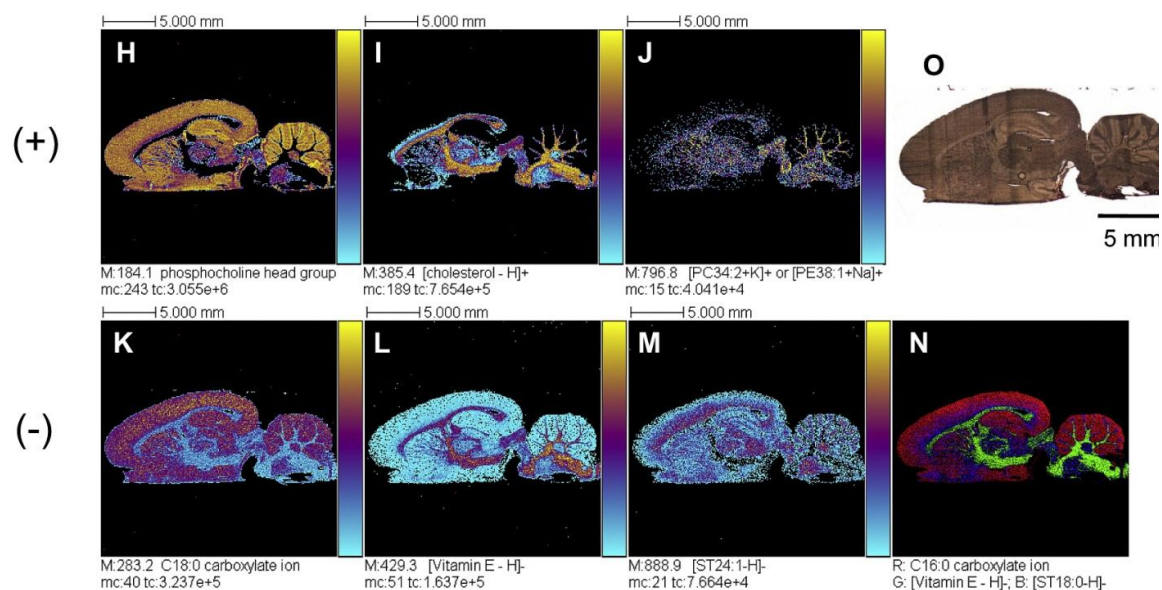


Figure 1.3. Sagittal section of rat brain. (Top row, left to right) SIMS images obtained in the positive mode—phosphocholine headgroup (m/z 184), cholesterol (m/z 385) and m/z 796.8—and optical image of the tissue. (bottom row: left to right) SIMS images obtained in the negative mode— Stearic (18:0) fatty acid fragment (m/z 283), vitamin E (m/z 429.3) and sulfoglycosphingolipid (sulfite, d18:1/24:1)—and the overlay of these ions. [fatty acid (red), vitamin E (green) and sulfite (blue)].⁶¹

The connection between spatial and chemical composition is lost with separation-based analysis techniques such as thin layer chromatography (TLC) and liquid chromatography mass spectrometry (LC-MS) since these techniques require the homogenization and extraction of the lipids from tissue before analysis. In order to retain spatial and chemical information with these methods, difficult and tedious micro-dissections are required.⁶² As a result, these methods are only effective on the macroscale and require highly skilled technicians. In the analysis of tissues, ToF-SIMS is capable of both macroscopic and microscopic-scale analyses.

In the characterization of tissue, ToF-SIMS offers dual functionality: For macro-scale studies where the whole tissue is of interest, the beam can be defocused to cover a large field of view. For micro-scale analyses selected regions of interest can be probed with a highly focused ion beam for a more detailed view. Overall, the ability to elucidate finer structural and chemical features within the tissue provides insight into the biochemical complexity of the cerebellum. For example, in the macroscale, cholesterol and sulfatides are homogeneously co-localized to the white matter of the cerebellum.⁶⁰ However, in a more detailed analysis of brain tissue, Nygren and coworkers were able to probe the chemistry of finer structures within the cerebellum as shown in Figure 1.4.^{37,63-}

⁶⁶ The histological layers (the molecular layer, Purkinje layer and the granular layer) were distinguished by their chemical signatures. Heterogeneous distributions of lipids within these histological structures were also observed. Dot-like sub-cellular distributions of galactosylceramides in the Purkinje and granular layers were speculated to be the result of intracellular vesicles, lipid rafts or ion channels. These subtle features were missed in the macroscale image and only observed due to the high spatial resolution afforded by SIMS technology.

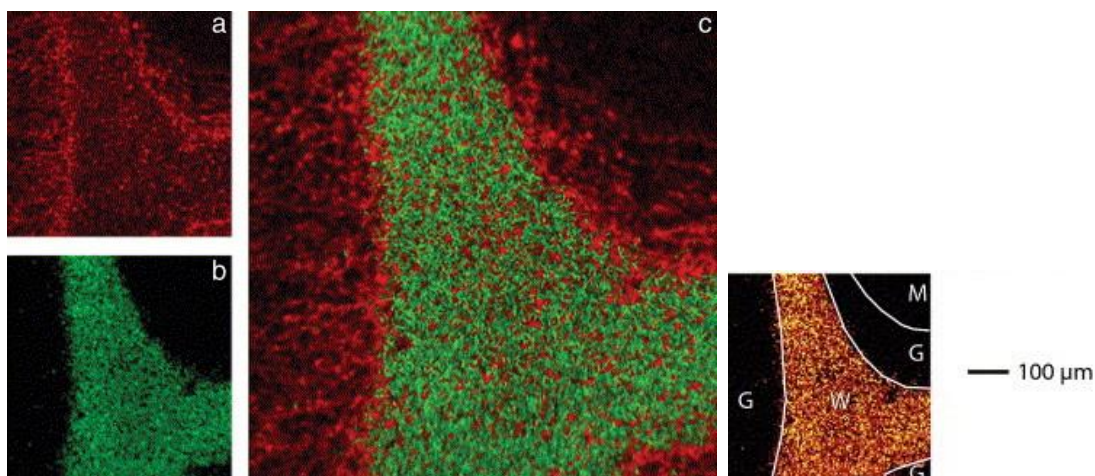


Figure 1.4. Negative ToF-SIMS images of cerebellum tissue (a) summed pixel intensities of sulfatides from m/z 778.5 to 934.6 red (b) ion intensities of cholesterol at m/z 385 green and (c) overlay of panels a and b. Regions of the cerebellum are outlined; molecular layers (m), white matter (w) and the gray matter (g).⁶⁶

Lipid species detected and identified from various mammalian tissues, including brain^{59,60,63,64,66-68}, spinal cord,⁶⁹ liver,⁷⁰ kidney,^{38,71,72} adipose,^{73,74} skeletal muscle,^{75,76} aorta⁷⁷ and retina,⁷⁸ with SIMS is concatenated in Table 1.1. Additional lipids detected from non-mammalian samples, *bacillus subtilis* and microbial mats, are reported in Table 1.2. Almost every major class of lipid is represented within these two tables. However, there are some notable absences from these lists, including saccharolipids, cholesterol esters, glycerophosphoethanolamine (GPEthn), phosphosphingolipids and all lipids with poly unsaturated fatty acid chains. Gas phase basicity and ion stability are major factors that contribute to a lipid's ability to be detected with SIMS. The lack of GPEthn and cholesterol esters may be due to the fragile nature of these molecules. Phosphoethanolamines have the propensity to

decompose, losing their phosphoethanolamine headgroups, thus producing a high mass fragment that isobarically interferes with diacylglycerides (DAGS). Similarly, the fatty acid moiety in cholesterol esters is readily hydrolyzed, producing a fragment ion that isobarically interferes with the high mass pseudomolecular ion of cholesterol (m/z 369).

ToF-SIMS has also been utilized in examining lipid-related diseases, such as Duchenne muscular dystrophy,^{76,79} Fabry disease,⁸⁰ non-alcoholic fatty liver disease,⁷⁰ atherosclerosis⁷⁷ and cystic fibrosis,⁸¹ as well as cancers. These diseases stem from dysfunctional metabolic processes (i.e. uptake, de novo synthesis or exportation) and result in abnormal concentrations of biomolecules. Chemical images across diseased tissue reveal areas of abnormal chemistry; such scarcity or over-abundance of a particular biomarker can link cellular dysfunction with anatomical specificity. Le Naour and coworkers found a higher concentration of unsaturated DAGS and triacylglycerides (TAGS), as well as increased cholesterol signals, in steatotic vesicles taken from an individual with fatty liver disease compared to normal tissue.⁷⁰ Also, in the analysis of aortic tissue, Malmberg and coworkers found that human atherosclerotic plaques contained irregular distribution of cholesterol and elongated DAGS.⁷⁷ The increased DAG concentration suggests increased phospholipase A (*PLA*) activity, which has been previously linked to the disease progression of atherosclerosis.

Table 1.1. Lipid species –protonated ions, adducts and pseudomolecular ions—identified in various mammalian tissue sections using ToF-SIMS and organized using the lipid classification system established by the Lipid MAPS consortium

Class/ Sub-Class [LM_ID]	Label (C:DB)	Mass	Formula	Species	Tissue
Glycerophospholipid/					
Glycerophosphates/	PA(34:0)	675.5	C ₃₇ H ₇₂ O ₈ P	[M-H] ⁻	Muscle ⁷⁹
Diacylglycerophosphates/ [GP1001]	PA(34:1)	673.5	C ₃₇ H ₇₀ O ₈ P	[M-H] ⁻	Brain ⁶⁰
	PA(36:1)	701.5	C ₂₉ H ₇₄ O ₈ P	[M-H] ⁻	Muscle ⁷⁹
Glycerophosphoinositols/	PI(36:4)	857.5	C ₄₅ H ₇₈ O ₁₃ P	[M-H] ⁻	Brain ^{59, 60}
Diacylglycerophosphoinositols/ [GP0601]	PI(38:4)	885.6	C ₄₇ H ₈₂ O ₁₃ P	[M-H] ⁻	Brain ^{59, 60} , Adipose ⁷⁴ , Liver ⁷⁰
	PI(38:3)	887.6	C ₄₇ H ₈₄ O ₁₃ P	[M-H] ⁻	Liver ⁷⁰
Glycerophosphoinositol monophosphates/ Diacylglycerophosphoinositol monophosphates/ [GP0701]	PIP(38:4)	965.6	C ₄₇ H ₈₃ O ₁₆ P ₂	[M-H] ⁻	Brain ⁵⁹
Glycerophosphocholines /	PC(34:2)	758.6	C ₄₂ H ₈₁ NO ₈ P	[M+H] ⁺	Liver ⁷⁰
Diacylglycerophosphocholines/ [GP0101]	PC(34:1)	760.6	C ₄₂ H ₈₃ NO ₈ P	[M+H] ⁺	Muscle ⁷⁹ , Brain ^{59, 60} , Liver ⁷⁰
	PC(34:1)	699.6	C ₃₉ H ₇₂ O ₈ P	[M-H-TMA] ⁻	Brain ⁶⁰
	PC(36:1)	788.6	C ₄₄ H ₈₇ NO ₈ P	[M+H] ⁺	Brain ^{59, 60}
	PC(32:0)	734.6	C ₄₀ H ₈₁ NO ₈ P	[M+H] ⁺	Muscle ⁷⁹ , Brain ^{59, 60, 71}
Glycerolipids/					
Monoradylglycerols/	MAG(16:1)	311.3	C ₁₉ H ₃₅ O ₃	[M+H-OH] ⁺	Liver ⁷⁰
Monoacylglycerols/ [GL0101]	MAG(16:0)	313.3	C ₁₉ H ₃₇ O ₃	[M+H-OH] ⁺	Liver ⁷⁰
	MAG(18:1)	339.3	C ₂₁ H ₃₉ O ₃	[M+H-OH] ⁺	Liver ⁷⁰
	MAG(18:0)	341.3	C ₂₁ H ₄₁ O ₃	[M+H-OH] ⁺	Liver ⁷⁰
Diradylglycerols/ Diacylglycerols/ [GL0201]	DAG(30:2)	519	C ₃₃ H ₅₉ O ₄	[M+H-OH] ⁺	Liver ⁷⁰
	DAG(30:1)	521	C ₃₃ H ₆₁ O ₄	[M+H-OH] ⁺	Liver ⁷⁰
	DAG(30:0)	523	C ₃₃ H ₆₃ O ₄	[M+H-OH] ⁺	Liver ⁷⁰ , Adipose ⁷⁴
	DAG(32:2)	547	C ₃₅ H ₆₃ O ₄	[M+H-OH] ⁺	Liver ⁷⁰
	DAG(32:1)	549	C ₃₅ H ₆₅ O ₄	[M+H-OH] ⁺	Liver ⁷⁰
	DAG(32:0)	551	C ₃₅ H ₆₇ O ₄	[M+H-OH] ⁺	Adipose ^{73, 74} , Liver ⁷⁰ , Muscle ⁷⁵
	DAG(34:3)	573	C ₃₇ H ₆₅ O ₄	[M+H-OH] ⁺	Liver ⁷⁰
	DAG(34:2)	575	C ₃₇ H ₆₇ O ₄	[M+H-OH] ⁺	Liver ⁷⁰
	DAG(34:1)	577	C ₃₇ H ₆₉ O ₄	[M+H-OH] ⁺	Adipose ⁷³ , Liver ⁷⁰ , Muscle ⁷⁵
	DAG(34:0)	579	C ₃₇ H ₇₁ O ₄	[M+H-OH] ⁺	Adipose ⁷⁴
	DAG(36:4)	599	C ₃₉ H ₆₇ O ₄	[M+H-OH] ⁺	Liver ⁷⁰
	DAG(36:3)	601	C ₃₉ H ₆₉ O ₄	[M+H-OH] ⁺	Liver ⁷⁰
	DAG(36:2)	603	C ₃₉ H ₇₁ O ₄	[M+H-OH] ⁺	Adipose ⁷³ , Liver ⁷⁰ , Muscle ⁷⁵
	DAG(36:0)	607	C ₃₉ H ₇₅ O ₄	[M+H-OH] ⁺	Adipose ⁷⁴
Triradylglycerols/ Triacylglycerols/ [GL0301]	TAG(48:0)	805	C ₅₁ H ₉₇ O ₆	[M-H] ⁻	Adipose ⁷⁴
	TAG(50:3)	851	C ₅₃ H ₉₇ O ₆ Na	[M+Na] ⁺	Liver ⁷⁰
	TAG(50:2)	829	C ₅₃ H ₉₇ O ₆	[M-H] ⁻	Muscle ⁷⁹
	TAG(50:2)	853	C ₅₃ H ₉₈ O ₆ Na	[M+Na] ⁺	Liver ⁷⁰

	TAG(50:1)	855	C ₅₃ H ₁₀₀ O ₆ Na	[M+Na] ⁺	Liver ⁷⁰
	TAG(50:0)	833	C ₅₃ H ₁₀₁ O ₆	[M-H] ⁻	Adipose ⁷⁴
	TAG(50:0)	857	C ₅₃ H ₁₀₂ O ₆ Na	[M+Na] ⁺	Liver ⁷⁰
	TAG(52:4)	877	C ₅₅ H ₉₈ O ₆ Na	[M+Na] ⁺	Liver ⁷⁰
	TAG(52:3)	855	C ₅₅ H ₉₉ O ₆	[M-H] ⁻	Adipose ⁷⁴
	TAG(52:3)	879	C ₅₅ H ₁₀₀ O ₆ Na	[M+Na] ⁺	Liver ⁷⁰
	TAG(52:2)	857	C ₅₅ H ₁₀₁ O ₆	[M-H] ⁻	Adipose ⁷³ , Muscle ⁷⁹
	TAG(52:2)	881	C ₅₅ H ₁₀₂ O ₆ Na	[M+Na] ⁺	Liver ⁷⁰
	TAG(52:1)	883	C ₅₅ H ₁₀₄ O ₆ Na	[M+Na] ⁺	Liver ⁷⁰
	TAG(52:0)	861	C ₅₅ H ₁₀₅ O ₆	[M-H] ⁻	Adipose ⁷⁴
	TAG(52:0)	885	C ₅₅ H ₁₀₆ O ₆ Na	[M+Na] ⁺	Liver ⁷⁰
	TAG(54:4)	881	C ₅₇ H ₁₀₁ O ₆	[M-H] ⁻	Muscle ⁷⁵
	TAG(54:3)	883	C ₅₇ H ₉₉ O ₆	[M-H] ⁻	Adipose ⁷³
Fatty Acyls/					
Fatty Acids and Conjugates/ Straight chain fatty acid/	FA(14:0)	227.2	C ₁₄ H ₂₇ O ₂	[M-H] ⁻	Liver ⁷⁰
	FA(16:0)	255.2	C ₁₆ H ₃₁ O ₂	[M-H] ⁻	Adipose ^{73, 74} , Muscle ^{75, 79} , Liver ⁷⁰
[FA0101]	FA(18:0)	283.2	C ₁₈ H ₃₅ O ₂	[M-H] ⁻	Muscle ^{75, 79} , Adipose ⁷⁴ , Liver ⁷⁰
Fatty Acids and Conjugates/	FA(16:1)	253.2	C ₁₆ H ₂₉ O ₂	[M-H] ⁻	Adipose ⁷³ , Muscle ^{75, 79} , Liver ⁷⁰
Unsaturated fatty acid/ [FA0103]	FA(16:2)	251.2	C ₁₆ H ₂₇ O ₂	[M-H] ⁻	Muscle ⁷⁹
	FA(18:3)	277.2	C ₁₈ H ₂₉ O ₂	[M-H] ⁻	Muscle ⁷⁹
	FA(18:2)	279.2	C ₁₈ H ₃₁ O ₂	[M-H] ⁻	Adipose ⁷³ , Muscle ⁷⁹ , Liver ⁷⁰
	FA(18:1)	281.2	C ₁₈ H ₃₃ O ₂	[M-H] ⁻	Adipose ⁷³ , Muscle ⁷⁹ , Liver ⁷⁰
	FA(20:4)	303.2	C ₂₀ H ₃₁ O ₂	[M-H] ⁻	Muscle ⁷⁹
Sterol Lipids/					
Cholesterol and derivatives / [ST01010001]	CH	369.3	C ₂₇ H ₄₅	[M+H-H ₂ O] ⁺	Adipose ⁷³ , Liver ⁷⁰ , Brain ^{59, 63, 71}
	CH	385.3	C ₂₇ H ₄₆ O	[M-H] ⁻	Muscle ⁷⁹ , Brain ⁵⁹
	CH	385.3	C ₂₇ H ₄₆ O	[M-H] ⁺	Brain ^{59, 63} , Liver ⁷⁰
	7-keto-cholesterol	399.3	C ₂₇ H ₄₃ O ₂	[M+H] ⁺	Aorta ⁷⁷
Prenol Lipids/					
Quinones and hydroquinones/ Vitamin E/ [PR02020001]	α-tocopherol	429.3	C ₂₉ H ₄₉ O ₂	[M-H] ⁻	Muscle ⁷⁹ , Liver ⁷⁰
		430.3	C ₂₉ H ₅₀ O ₂	[M] ⁺	Retina ⁷⁸ , Liver ⁷⁰
Quinones and hydroquinones/ Ubiquinones/ [PR02010004]	coenzyme Q9	795.6	C ₅₄ H ₈₃ O ₄	[M-H] ⁻	Muscle ⁷⁹
Sphingolipids/					
Acidic glycosphingolipids/ Sulfoglycosphingolipids (sulfatides)/ [SP0602]	C16 ^a	778.5	C ₄₀ H ₇₆ SNO ₁₁	[M-H] ⁻	Brain ⁶⁶
	C16-OH ^b	794.6	C ₄₀ H ₇₆ SNO ₁₂	[M-H] ⁻	Brain ⁶⁶
	C18	806.6	C ₄₂ H ₈₀ SNO ₁₁	[M-H] ⁻	Brain ^{59, 60, 66}
	C18-OH	822.5	C ₄₂ H ₈₀ SNO ₁₂	[M-H] ⁻	Brain ^{59, 60, 66}
	C20	834.6	C ₄₄ H ₈₄ SNO ₁₁	[M-H] ⁻	Brain ^{59, 60, 66}
	C22-OH	850.6	C ₄₄ H ₈₄ SNO ₁₂	[M-H] ⁻	Brain ^{59, 60, 66}
	C22	862.6	C ₄₆ H ₈₈ SNO ₁₁	[M-H] ⁻	Brain ^{59, 60, 66}
	C23	876.7	C ₄₇ H ₉₀ SNO ₁₁	[M-H] ⁻	Brain ^{59, 66}
	C22-OH	878.6	C ₄₆ H ₈₈ SNO ₁₂	[M-H] ⁻	Brain ^{59, 60, 66}
	C24:1	888.6	C ₄₈ H ₉₀ SNO ₁₁	[M-H] ⁻	Brain ^{59, 60, 66}
	C24	890.6	C ₄₈ H ₉₂ SNO ₁₁	[M-H] ⁻	Brain ^{59, 60, 66}
	C25:1	902.6	C ₄₉ H ₉₂ SNO ₁₁	[M-H] ⁻	Brain ⁶⁶

	C24:1-OH or C25	904.6	C ₄₈ H ₉₀ SNO ₁₂	[M-H] ⁻	Brain ^{59, 60, 66}
	C24-OH	906.6	C ₄₈ H ₉₂ SNO ₁₂	[M-H] ⁻	Brain ^{59, 60, 66}
	C26:1	916.6	C ₅₀ H ₉₄ SNO ₁₁	[M-H] ⁻	Brain ⁶⁶
	C25:1-OH or C26	918.6	C ₄₉ H ₉₂ SNO ₁₂	[M-H] ⁻	Brain ⁶⁶
	C26:1-OH	932.7	C ₅₀ H ₉₄ SNO ₁₂	[M-H] ⁻	Brain ⁶⁶
	C26-OH	934.6	C ₅₀ H ₉₆ SNO ₁₂	[M-H] ⁻	Brain ⁶⁶
Neutral glycosphingolipids/ Simple G/c series/ [SP0501]	C18:0	750.6	C ₄₂ H ₈₁ NO ₆ Na	[M+Na] ⁺	Brain ⁶³ , Aorta ⁷⁷
	C24:0 ^c	834.6	C ₄₈ H ₉₃ NO ₆ Na	[M+Na] ⁺	Brain ^{63, 64} , Aorta ⁷⁷
	C24:1	832.6	C ₄₈ H ₉₁ NO ₆ Na	[M+Na] ⁺	Brain ^{63, 64}
	Ch24:0 ^d	850.6	C ₄₈ H ₉₃ NO ₆ Na	[M+Na] ⁺	Brain ^{63, 64} , Aorta ⁷⁷
	Ch24:1	848.6	C ₄₈ H ₉₁ NO ₆ Na	[M+Na] ⁺	Brain ^{63, 64}
	Ch23:0	836.6	C ₄₇ H ₉₁ NO ₆ Na	[M+Na] ⁺	Brain ⁶⁴
	Ch22:0	822.6	C ₄₆ H ₈₉ NO ₆ Na	[M+Na] ⁺	Brain ⁶⁴
Phosphosphingolipids/ Ceramide phosphocholines	SM(34:1)	616.5	C ₃₄ H ₆₇ NO ₆ P	[M-]	Liver ⁷⁰
Sphingomyelin [SP0301]	SM(34:1)	642.6	C ₃₆ H ₆₉ NO ₆ P	[M-(N(CH ₃) ₃)] ⁻	Liver ⁷⁰
	SM(34:1)	687.6	C ₃₈ H ₇₆ N ₂ O ₆ P	[M-CH ₃] ⁻	Liver ⁷⁰

^a C16 = (3'-Sulf)Galβ-Cer(d18:1/16:0)

^b C16-OH = (3'-Sulf)Galβ-Cer(d18:1/2-OH-16:0)

^c C24:0 = GalCer(d18:1 / 2-OH-24:0)

^d Ch24:0 = GalCer(d18:1 / 2-OH-24:0)

Table 1.2. Lipid species identified from bacterial and microbial colonies usingToF-SIMS and organized using the lipid classification system established by the Lipid MAPS consortium.

Class/sub-class	Labels	Mass	Formula	Species	Tissue
Polyketides/					
Surfactin/	M13	1006.6	C ₅₁ H ₈₈ N ₇ O ₁₃	[M-H] ⁻	<i>B. subtilis</i> ⁸²
	M14	1020.6	C ₅₂ H ₉₀ N ₇ O ₁₃	[M-H] ⁻	<i>B. subtilis</i> ⁸²
	M14	1042.6	C ₅₂ H ₈₈ N ₇ O ₁₃ Na	[M-]	<i>B. subtilis</i> ⁸²
	M15	1034.6	C ₅₃ H ₉₂ N ₇ O ₁₃	[M-H] ⁻	<i>B. subtilis</i> ⁸²
	M15	1056.6	C ₅₃ H ₉₀ N ₇ O ₁₃ Na	[M-]	<i>B. subtilis</i> ⁸²
	M15	1072.6	C ₅₃ H ₉₀ N ₇ O ₁₃ K	[M-2H+K] ⁻	<i>B. subtilis</i> ⁸²
	M16	1048.6	C ₅₄ H ₉₄ N ₇ O ₁₃	[M-H] ⁻	<i>B. subtilis</i> ⁸²
Flavonoids/	Quercetin 3-o-galactoside	463.16	C ₂₁ H ₁₉ O ₁₂	[M-H] ⁻	<i>P. sativum</i> seed ⁸³
Flavones and Flavonols/ [PK12111]	Quercetin 3-o-rhamnoside	447.12	C ₂₁ H ₁₉ O ₁₁	[M-H] ⁻	<i>A. thaliana</i> seed ⁸³
	Apigenin glycoside	431.34	C ₂₁ H ₁₉ O ₁₀	[M-H] ⁻	<i>P. sativum</i> seed ⁸³
	Protocatechuic acid glycoside	315.08	C ₁₂ H ₁₅ O ₉	[M-H] ⁻	<i>P. sativum</i> seed ⁸³
[PK12110003]	Kaempferol	285.01	C ₁₅ H ₉ O ₆	[M-H] ⁻	<i>A. thaliana</i> and
[PK12110004]	Quercetin	301.05	C ₁₅ H ₉ O ₇	[M-H] ⁻	<i>A. thaliana</i> and
Flavonoids/ Flavans, Flavonols and Leucoanthocyanidins/ [PK1202]	(+) catechin or (-) epicatechin [PK12020001 or PK12020003]	288.98	C ₁₅ H ₁₃ O ₆	[M-H] ⁻	<i>P. sativum</i> seed ⁸³
Glycerolipids/					
Diradylglycerols/	Dihydroxyarchaeol	707	C ₄₃ H ₈₈ O ₅	[M+Na] ⁺	microbial mats ⁸⁴
Dialkylglycerols/ [GL0203]	Archaeol [GL02030035]	675	C ₄₃ H ₈₈ O ₃	[M+Na] ⁺	microbial mats ⁸⁴

	Hydroxyarchaeol	691	C ₄₃ H ₈₈ O ₄	[M+Na] ⁺	microbial mats ⁸⁴
Di-glycerol tetraether/ [GL0205]	C40 isoprenoid GDGT 0 ^a	1324	C ₈₆ H ₁₇₂ O ₆	[M+Na] ⁺	microbial mats ⁸⁴
	C40 isoprenoid GDGT 1	1322	C ₈₆ H ₁₇₀ O ₆	[M+Na] ⁺	microbial mats ⁸⁴
	C40 isoprenoid GDGT 2	1320	C ₈₆ H ₁₆₈ O ₆	[M+Na] ⁺	microbial mats ⁸⁴
	C40 isoprenoid GDGT 3	1318	C ₈₆ H ₁₆₆ O ₆	[M+Na] ⁺	microbial mats ⁸⁴
	C40 isoprenoid GDGT 4	1316	C ₈₆ H ₁₆₄ O ₆	[M+Na] ⁺	microbial mats ⁸⁴
Diradylglycerols/ Di-glycerol tetraether/ [GL0206]	gentiobiosyl-GDGT 0	1648	C ₉₈ H ₁₉₂ O ₁₆	[M+Na] ⁺	microbial mats ⁸⁴
	gentiobiosyl-GDGT 1	1646	C ₉₈ H ₁₉₀ O ₁₆	[M+Na] ⁺	microbial mats ⁸⁴
	gentiobiosyl-GDGT 2	1644	C ₉₈ H ₁₈₈ O ₁₆	[M+Na] ⁺	microbial mats ⁸⁴
	gentiobiosyl-GDGT 3	1642	C ₉₈ H ₁₈₆ O ₁₆	[M+Na] ⁺	microbial mats ⁸⁴
	gentiobiosyl-GDGT 4	1640	C ₉₈ H ₁₈₄ O ₁₆	[M+Na] ⁺	microbial mats ⁸⁴
Glycosyldiradylglycerols/ gentiobiosyl-archaeol	999	C ₅₅ H ₁₀₈ O ₁₃	[M+Na] ⁺	microbial mats ⁸⁴	

^a GDGT = Glycerol dialkyl glycerol tetra ether

1.5. Single cell imaging experiments

Currently, ToF-SIMS is the only mass spectrometry imaging technique capable of characterizing the lateral distribution of lipids on a cellular and subcellular level.^{85,86} The first ToF-SIMS images of cells were obtained using atomic projectile sources. These high resolution images of isolated cells provided useful elemental distributions and isotopic information. However, the extensive molecular fragmentation from the energetic impact and the resulting chemical damage accumulation hampered technique's utility in lipid research. One major drawback that limited the potential application of the technique was its inability to detect intact glycerophospholipids. In these early studies, this large and diverse class of molecules was routinely reduced to the detection of the headgroup fragment, such as m/z 142 for the GPEthn and m/z 184 for GPCho. In addition, the sample's fatty acid contribution was often evaluated separately in the negative ion SIMS spectra. The separated detection of headgroups and fatty acid constituents prevented lipid identification and made it difficult to extract useful biochemical information from systems under study.

Despite these difficulties, Ostrowski and co-workers were able to study changes in the cellular membrane lipid composition during mating of *tetrahymena thermophila*, which was prepared in a freeze-fractured frozen hydrated state.⁸⁷ This task was accomplished by examining the GPCho headgroup fragment, phosphocholine, at m/z 184 ($C_5H_{15}NPO_4$) and the 2-aminoethylphosphonolipids (2-AeP) headgroup fragment at m/z 126 ($C_2H_9NPO_3$) (see Figure 1.5). These workers found an accumulation of highly contoured, non-lamellar, 2-AeP lipids and a depletion of lamellar GPCho lipids at the conjugation junction during mating. In order to elucidate the driving force behind these lipid heterogeneities, time-based studies on this system were performed.⁸⁸ These studies concluded that structural changes in the membrane preceded chemical changes. More specifically, pore formation—most likely initiated by membrane bound protein activity—created structural deformations in the membrane that attracted high-curvature lipids and displaced phosphocholine. This study provides important insight concerning the role of lipids in complex biological processes and established a clear link between chemical structure and function. Since the observed lipid segregation was dependent upon the biophysical characteristics of the lipid's headgroup, it is possible that the chemical composition of the lipid's fatty acid constituents was also a contributing factor. Therefore, future studies in which intact lipid species are detected would be beneficial to better understanding this system.

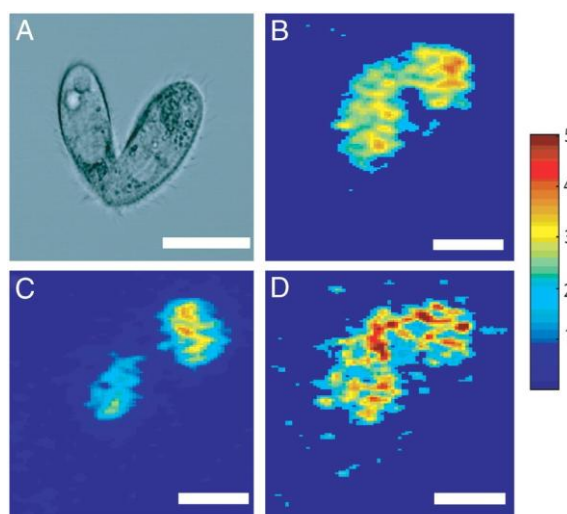


Figure 1.5. Microscopy (DIC) image of a mating *tetrahymena thermophila* (a) and SIMS image depicting localizations of an ubiquitous organic ion at m/z 69 (C_5H_9 , b). Lipid heterogeneities at the mating junction includes a depletion of phosphocholine (c) and an accumulation of 2-AEP (d). (Scale bar: 25 μm)⁸⁸

Although the detection of glycerophospholipids is difficult at the cellular level, mass spectrometric-friendly lipid molecules, such as cholesterol and vitamin E, are easily detectable at the cellular level.^{89,90} Monroe and coworkers demonstrated heterogeneous localizations of cholesterol on the surface of a single *aplysia californica* neuron using SIMS. The ability to readily detect vitamin E at the cellular level is important, since vitamin E is implicated in lipid oxidation, which is a process linked to a variety of diseases including Alzheimer's and Parkinson's disease.^{91,92}

Yang and co-workers were able to successfully detect intact glycerophosphocholine species directly from the surface of a cultured neuron obtained from the superior cervical ganglia of a mouse.⁹³ The protonated and sodiated molecular-

ion of various GPCho molecules were detected. The identifications were made by reconciling the most abundant headgroup in positive ion mode with the most abundant fatty acid constituents obtained in negative ion mode. In addition, Yang and coworkers were able to distinguish the GPCho from the sphingomyelin (SM) contribution in the lipid profiles by focusing on fragment ions m/z 224.1 and 246.1 that are distinct to glycerophosphocholine (see Figure 1.6). This group reported that although the shared phosphocholine and SM components (m/z 206) are homogeneously distributed throughout the neuritis, the signal that was unique to GPCho was heterogeneous with strong intensity in the neurites surrounding the soma.

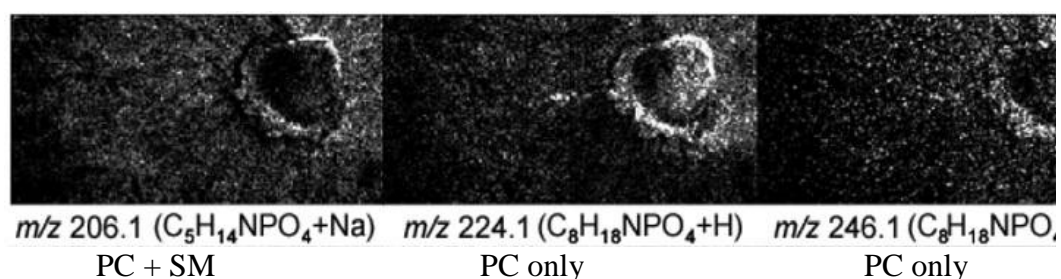


Figure 1.6. SIMS images of a cultured neuron obtained from the superior cervical ganglia of a mouse. Ion contribution from the phosphocholine headgroup (m/z 206.1, m/z 224.1 and m/z 246.1) is distinguished from the SM headgroup (m/z 206.1) fragments.⁹³

1.6. Sensitivity issues

At the cellular level, instrument performance is greatly limited by sensitivity. The trade-off between high resolution and secondary ion yields has often limited the detection of intact phospholipids at the cellular level. As smaller and smaller

regions are probed for high lateral resolution, the number of molecules available to be desorbed, ionized and detected is reduced. The production of secondary ions is often the limiting factor in sensitivity. The search for methods to enhance ionization probability is, therefore, continuously underway. The benefit of improving sensitivity is twofold: It allows for the detection of abundant lipids at a sub-cellular level and it allows for the detection of low abundant lipid species, typically involved in signaling pathways.

Recently, novel approaches have been developed to improve the sensitivity of the system and push the detection limits beyond the technical capabilities of the instrument. Surface treatments involving thin layers of metals and matrices, known as metal assisted (MetA) and matrix enhanced (Me) SIMS, have been shown to improve the desorption/ionization of analytes. Complications associated with these methods, such as molecular specific enhancements and spectral interference from matrix clusters and adducts, tend to complicate quantification and identification efforts. The exact mechanism behind ion enhancement with these methods is currently unknown. Although matrix application methods have become more sophisticated in recent years, the incorporation of matrix into a sample ultimately reduces the lateral resolution because of chemical displacement.

Heeren and coworkers have utilized the ion yield enhancements afforded by MetA- and Me-SIMS to detect intact phospholipids and sterol from single cells.⁹⁴ Neuroblastoma cells, approximately 50 microns in diameter, were coated with a nanometer of gold using a high resolution sputter coater typically employed for secondary electron microscopy (SEM) and transmission electron microscopy (TEM)

analyses. A highly focused 15 keV In source was employed to provide sub-cellular details. Without metal or matrix treatment, high mass intact phospholipids were not observed and the detection of lipids was limited to fragments, such as phosphocholine (m/z 184) and DAG (m/z 550-650) fragment ions. However, with the application of matrix, the group could identify several glycerophospholipid species in the positive ion mode, including 32:0, 34:1, 34:2, 36:1, 36:2, 38:4 and 38:5 GPCho and 36:1 GPEtn. Also, despite desalting procedures involving a sucrose washing, the sodium adduct of 34:1 GPCho was a dominant mass peak. Without high mass resolution or tandem MS verification, however, these assignments must be taken with caution due to possible isobaric interferences.

Molecular depth profiling^{42,45,68,95-98} has also been employed to improve the detection limits at high resolution and has done so without sample manipulation. With depth profiling methods, the advantage is obtained by turning a pixel into a voxel. Cluster ion sources, like C_{60}^+ , are capable of interrogating the surface and sub-surface of a sample with limited damage accumulation and chemical mixing. In the end, a larger portion of the sample is probed without degrading lateral spatial resolution. This approach does not improve the ionization probability, rather it simply increases the amount of material available. The capability to analyze lipid distributions in three-dimensional space on a cellular level was demonstrated by Fletcher and coworkers (see Figure 1.7).⁹⁹ The distribution of cholesterol (m/z 369), phospholipid-related fragment molecules accumulated over the m/z 540-570 mass range and fatty acid side chain fragments in an oocyte were mapped.

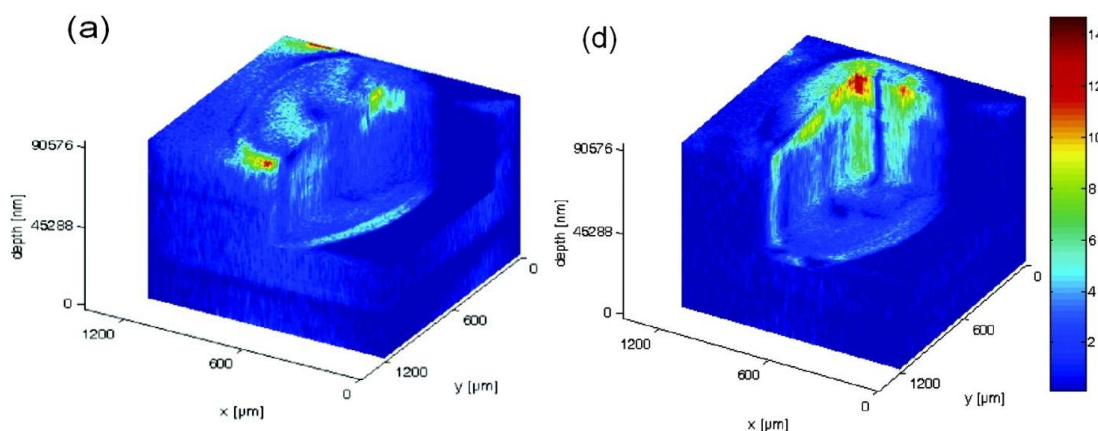


Figure 1.7. 3D biochemical images of freeze-dried oocyte depicting phosphocholine signal from m/z 58, 86, 166, and 184 (a) and cholesterol signal at m/z 369 (d).⁹⁹

Lipid species –protonated ions, adducts, pseudomolecular ions and fragments—identified in various mammalian and non-mammalian cell lines using ToF-SIMS are organized by the lipid classification system established by the Lipid MAPS consortium in Table 1.3. On the cellular level, very few intact lipid species are observed other than the mass spectrometry-friendly lipid species: cholesterol, vitamin E and GPCho. At this level, lipid fragments are commonly observed and used to identify whole classes of lipid species. However, this method is not always reliable since several classes of lipid share common fragment ions. Reoccurring themes in lipid chemical structure not only produce isobaric interferences, but also result in common fragments ions. For example, fragment ions at m/z 126 and 142 represent both GPETHn and phosphosphingolipids. In protozoan cell lines, these fragments are identified as the headgroup of phosphosphingolipids and in mammalian-derived cell lines these lipid

fragments are assigned to GPEthn. Without intact lipids, previous knowledge of species and its lipid content is needed for such assignments.

Table 1.3. Lipid species –protonated ions, adducts, pseudomolecular ions and fragments—identified in various mammalian and non-mammalian cell lines using ToF-SIMS and organized using the lipid classification system established by the Lipid MAPS consortium.

Class/ Sub-class [LM_ID]	Label (C:DB)	Mass	Formula	Species	Cell type
Fatty Acyls/					
Fatty Acids and Conjugates/	FA(16:0)	255.2	C ₁₆ H ₃₁ O ₂	Fragment	Mouse neuron ⁹³ , <i>Xenopus laevis</i> oocyte ⁹⁹
Straight chain fatty acids/ [FA0101]	FA(18:0)	283.2	C ₁₈ H ₃₅ O ₂	Fragment	Mouse neuron ¹⁰⁰
Fatty Acids and Conjugates/	FA(18:1)	281.2	C ₁₈ H ₃₃ O ₂	Fragment	Mouse neuron ⁹³ , <i>Xenopus laevis</i> oocyte ⁹⁹
Unsaturated fatty acid/ [FA0103]	FA(18:2)	279.2	C ₁₈ H ₃₁ O ₂	Fragment	<i>Xenopus laevis</i> oocyte ⁹⁹
Glycerophospholipids/					
Glycerophosphocholines/ [GP01]		59	C ₃ H ₉ N	Fragment	Mouse neuron ⁹³ , PMNL ^b ¹⁰¹ , <i>Xenopus laevis</i> oocyte ⁹⁹
		86	C ₅ H ₁₂ N	Fragment	PC-12 ^c ¹⁰² , Mouse neuron ⁹³ , <i>Xenopus laevis</i> oocyte ⁹⁹
		104	C ₅ H ₁₄ NO	Fragment	Mouse neuron ⁹³
		166	C ₅ H ₁₃ NPO ₃	Fragment	PC-12 ⁴⁴ , <i>Xenopus</i> <i>laevis</i> oocyte ⁹⁹
		184	C ₅ H ₁₅ NPO ₄	Fragment	PMNL ¹⁰¹ , PC-12 ⁴⁴ ¹⁰² , J774 ¹⁰³ , <i>Aplysia</i> <i>californica</i> neuron ⁸⁹ , <i>Xenopus laevis</i> oocyte ⁹⁹ , Mouse neuron ¹⁰⁰
		206	C ₅ H ₁₄ PO ₄ Na	Fragment	Mouse neuron ⁹³
		224	C ₈ H ₁₉ NPO ₄	Fragment	PC-12 ⁴⁴ , Mouse neuron ⁹³
	246	C ₈ H ₁₈ NPO ₄ Na	Fragment	Mouse neuron ⁹³	
Glycerophosphocholine / Diacylglycerophosphocholines/ [GP0101]	GPCho(32:1)	732 ^a	C ₄₀ H ₇₉ NO ₈ P	[M+H] ⁺	neuroblastoma cells ⁹⁴
	GPCho(34:2)	758 ^a	C ₄₂ H ₈₁ NO ₈ P	[M+H] ⁺	neuroblastoma cells ⁹⁴
	GPCho(34:1)	760 ^a	C ₄₂ H ₈₃ NO ₈ P	[M+H] ⁺	neuroblastoma cells ⁹⁴
	GPCho(34:1)	782 ^a	C ₄₂ H ₈₃ NO ₈ PNa	[M+Na] ⁺	neuroblastoma cells ⁹⁴ , Mouse neuron ¹⁰⁰
	GPCho(36:1)	788 ^a	C ₄₄ H ₈₇ NO ₈ P	[M+H] ⁺	neuroblastoma cells ⁹⁴
	GPCho(38:5)	808 ^a	C ₄₆ H ₈₃ NO ₈ P	[M+H] ⁺	neuroblastoma cells ⁹⁴
	GPCho(38:4)	810 ^a	C ₄₆ H ₈₅ NO ₈ P	[M+H] ⁺	neuroblastoma cells ⁹⁴
Glycerophosphocholine /	GPCho(16:0e/18:1)	709	C ₃₉ H ₇₅ O ₇ PNa	[M+Na- TMA] ⁺	<i>Aplysia californica</i> neuron ¹⁰⁴

1-alkyl,2-	GPCho(16:0e/18:1)	725	C ₃₉ H ₇₅ O ₇ PK	[M+K-TMA] ⁺	<i>Aplysia californica</i> neuron ¹⁰⁴
Acylglycerophosphocholines/ [GP0102]	GPCho(16:0e/18:1)	746	C ₄₂ H ₈₅ NO ₇ P	[M+H] ⁺	<i>Aplysia californica</i> neuron ¹⁰⁴
	GPCho(16:0e/18:1)	768	C ₄₂ H ₈₄ NO ₇ PNa	[M+Na] ⁺	<i>Aplysia californica</i> neuron ¹⁰⁴
	GPCho(16:0e/18:1)	784	C ₄₂ H ₈₄ NO ₇ PK	[M+K] ⁺	<i>Aplysia californica</i> neuron ¹⁰⁴
Glycerophosphoethanolamines [GP02]		126	C ₂ H ₉ NPO ₃	Fragment	PC-12 ⁴⁴
		142	C ₂ H ₉ NPO ₄	Fragment	PC-12 ⁴⁴ , J774 ¹⁰³
Glycerophosphoethanolamines/ Diacylglycerophosphoethanolamines/ [GP0201]	GPEthn(36:1)	746	C ₄₁ H ₈₁ NO ₈ P	[M+H] ⁺	neuroblastoma cells ⁹⁴
Sphingolipids/					
Phosphosphingolipids/ Ceramide phosphocholines (sphingomyelins)/ [SP0301]		86	C ₅ H ₁₂ N	Fragment	Mouse neuron ⁹³
		102	C ₅ H ₁₂ NO	Fragment	Mouse neuron ⁹³
		104	C ₅ H ₁₄ NO	Fragment	Mouse neuron ⁹³
		184	C ₅ H ₁₅ NPO ₄	Fragment	Mouse neuron ⁹³
		206	C ₅ H ₁₄ PO ₄ Na	Fragment	Mouse neuron ⁹³
Phosphosphingolipids/ [SP04]	(2-AeP)	126	C ₂ H ₉ NPO ₃	Fragment	<i>Tetrahymena thermophila</i> ^{87, 88}
		142	C ₂ H ₉ NPO ₄	Fragment	<i>Tetrahymena thermophila</i> ^{87, 88}
Sterol Lipids/					
Cholesterol and derivatives/ [ST01010001]	CH	95	C ₇ H ₁₁	Fragment	J774 ¹⁰⁵
		109	C ₈ H ₁₃	Fragment	J774 ¹⁰⁵
		147	C ₁₁ H ₁₅	Fragment	J774 ¹⁰⁵
		161	C ₁₂ H ₁₇	Fragment	J774 ¹⁰⁵
		369.3	C ₂₇ H ₄₅	[M+H-H ₂ O] ⁺	PC-12 ¹⁰² , J774 ¹⁰⁵ , <i>Xenopus laevis</i> oocyte ⁹⁹
		385.3	C ₂₇ H ₄₆ O	[M-H] ⁺	PC-12 ¹⁰²
		583	C ₂₇ H ₄₆ O ₂ Au	[M+Au] ⁺	PMNL ¹⁰¹ , neuroblastoma cells ⁹⁴
		970	C ₅₄ H ₉₃ O ₂ Au	[2M+Au] ⁺	PMNL ¹⁰¹ , neuroblastoma cells ⁹⁴
		1167	C ₅₄ H ₉₃ Au ₂	[2M+2Au] ⁺	neuroblastoma cells ⁹⁴
Prenol Lipids/					
Quinones and hydroquinones/ Vitamin E/ [PR02020001]	α-tocopherol	165	C ₁₀ H ₁₃ O ₂	Fragment	<i>Aplysia californica</i> neuron ⁸⁹
		205	C ₁₃ H ₁₇ O ₂	Fragment	<i>Aplysia californica</i> neuron ⁸⁹
		430.3	C ₂₉ H ₅₀ O ₂	[M] ⁺	<i>Aplysia californica</i> neuron ⁸⁹

^aFor consistency, masses were adjusted from the reported values for the neuroblasmtoma cells to compensate for rounding error.

^bPMNL = polymorphonuclear leukocytes

^cPC-12 = pheochromocytoma

1.7. Dynamic SIMS

Although this review mainly focuses on studies employing static SIMS, dynamic SIMS has also been successfully employed in lipid studies. As previously mentioned, this method employs a continuous primary ion beams that produces mostly atomic and diatomic species. Despite the highly destructive secondary ion generation process, this method is capable of achieving spatial resolution of at least 50 nm. In order to investigate lipid processes, halogen-based or stable isotopic tracers (^{13}C , ^{14}N or deuterium) are required. Incorporating these tracers into the analyte of interest is a major challenge associated with this technique. Traceable lipids are added to cell culturing media and incorporated into cell lines during incubation. Lechene and coworkers were able to study the distribution of monounsaturated fatty acid, by incubating 3T3F442A adipocytes with isotopically traceable oleate fatty acids (^{13}C).¹⁰⁶ The movement of fatty acids within cells can be traced and measured to sub-cellular locations using the signal $^{13}\text{C}/^{12}\text{C}$ ratio (see Figure 1.8). These experiments are time-limited since dynamic metabolic and catabolic processes quickly redistribute the tracers, obscuring the analyte or biological process under investigation. This technique has been used to study the formation of lipid domain in model systems.^{107,108} Like MALDI, this method provides a complementary perspective to ToF-SIMS. Although this technique does not provide molecular ion information, the high lateral resolution associated to this method is valuable for sub-cellular investigations.

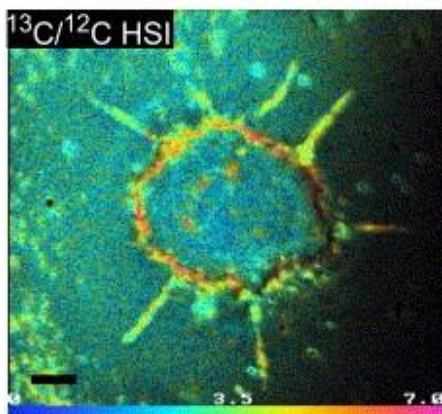


Figure 1.8. Image acquired with dynamic SIMS, illustrates the distribution of isotopically traceable monosaturated fatty acid, oleate, in a single 3T3F442A adipocyte¹⁰⁶. The oleate is localized to the cell membrane and discrete lipid droplets inside the cell.

1.8. Challenges associated with the SIMS analysis of lipids

The increased sensitivity to intact lipid species afforded by the technical and methodological advances described above brings about new challenges in the analyses of lipids. For instance, the ability to properly identify lipid molecules from a complex mixture is crucial for *in situ* lipidomics-based investigation. In SIMS-based investigations, lipid assignments are typically based on standard reference spectra, mass accuracy of the molecular-ion peaks and previous knowledge of the sample's biochemistry. However, these methods of identification are not sustainable as researchers continue to probe deeper into increasingly complex and unknown biological systems. Lipid profiles obtained from *in situ* mass spectrometry imaging experiments are plagued by isobaric interference in addition to matrix effects and ion suppression effects.

High mass resolution and tandem MS capabilities, functionalities commonly employed in MALDI and DESI experiments, can be utilized to deconvolute isobaric interferences and help identify the detected lipid species. Traditional ToF-SIMS instruments have limited mass resolution and lack tandem MS capabilities. Newly developed SIMS instruments are emerging to overcome these inadequacies, as discussed in the next section.

High mass resolution is needed to separate and distinguish individual lipid molecules in complex mixtures. For certain classes of lipids it is not uncommon to have multiple molecular signatures at the same nominal mass unit. For example, the number of potential phospholipids at each mass unit in the 650-900 Dalton mass region can range from 2 to 200, depending on the phospholipid class. The large number of possible lipid species stems from the variability of the three fundamental structural components – the headgroup, the glycerol-fatty acid linkage, and the two fatty acid components. Structurally, the headgroup of a glycerophospholipid consists of a phosphate group attached to one of the following functional groups: choline, serine, ethanolamine, glycerol or inositol. The headgroup is attached to the *sn*-3 site of the glycerol moiety. The *sn*-1 and *sn*-2 glycerol sites are typically attached to the fatty acid functional groups. There are three types of glycerol-fatty acid linkages: 1-2-diacyl, 1-alkyl-2-acyl, and 1-alk-1-enyl-2-acyl; these linkages are described as diacyl, ether, and plasmalogen lipids, respectively. The fatty acid moieties vary in fatty acid chain length, degree of saturation and double bond position.

Tandem MS analyses have proven to be vital to identifying the molecular nature of lipid molecules. In this method, the unknown lipid molecule is selected and

fragmented in a collision-induced dissociation (CID) chamber. The resulting spectrum reveals vital structural information that assists in the identification of the lipid molecule.

1.9. Recent developments in instrumentation

Although many traditional ToF-SIMS instruments have been updated with cluster ion sources, their overall design and capabilities are still generally underdeveloped for the complex nature of biological-based applications. Currently, technical design flaws associated with traditional static ToF-SIMS instruments hinder the technique's ability to effectively and efficiently analyze lipids and other bio-molecules. For example, traditional ToF-SIMS instruments employ pulsed primary ion beams and delayed extraction optics to combat energy spreads associated with variations in ion formation times. In this configuration, mass resolution is dependent on, and ultimately limited by, the temporal width of the primary ion beam. As a result, high mass resolution is achieved at the expense of primary ion beam duty cycle, which is a performance efficiency factor defined by the time the beam is on as a function of total acquisition time. In addition, this configuration is incompatible with tandem MS analyses and continuous ion beam generation. Within this new area of lipid applications, design changes are needed. For these complex systems, it is necessary to have high throughput and high mass resolution instruments with tandem MS capabilities. With these factors in consideration, two new high performance ToF-SIMS instruments, the J105¹⁰⁹ and the C₆₀⁺ QSTAR,¹¹⁰ were developed. In both systems, high throughput was achieved by employing a continuous

primary ion beam. High mass resolution was achieved in conjunction with high throughput by decoupling the ionization event from the spectral acquisition.

The C_{60}^+ QSTAR instrument combines a 20 keV C_{60}^+ source with a commercial triple quadrupole orthogonal ToF Mass Spectrometer from Applied Biosystems/MDS Sciex Q-STAR XL (see Figure 1.9).¹¹⁰ Tandem MS information is obtained by selecting the parent ion in quadrupole 1 (Q_1) and subsequently fragmenting the ion via CID in quadrupole 2 (Q_2). A differential pumping system in the C_{60}^+ QSTAR instrument is used to sweep desorbed ions into the mass spectrometer without the assistance of a high voltage extraction. The lack of high voltage extraction optics mitigates sample charging issues in the positive ion mode. Orthogonal extraction is responsible for decoupling the secondary ion generation event from the detection scheme; resulting in high mass resolution spectra ($m/\Delta m$ 12,000-15,600).¹¹⁰ Dual sources, C_{60}^+ gun and N_2 laser, allow for parallel SIMS and MALDI-based investigations. Since both methods are suitable platforms for lipid imaging, complementary datasets for both techniques can be compiled in order to extract the greatest amount of information from a common system. In addition, this platform allows for the study of the fundamental aspects of MALDI, such as the effects of different matrix application techniques on the spatial resolution and desorption characteristics.

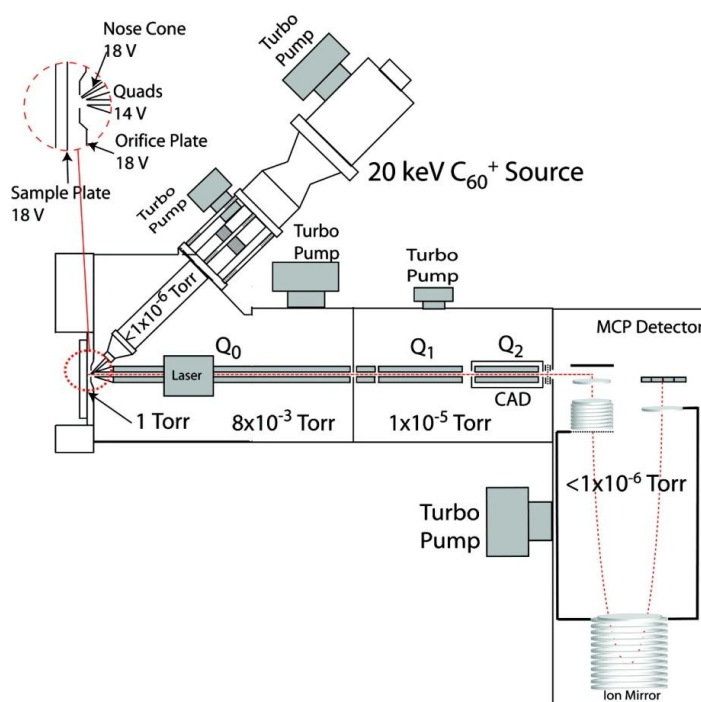


Figure 1.9. Schematic of the C_{60}^+ -QSTAR instrument shows how the commercial triple quadrupole orthogonal ToF mass spectrometer was interfaced with a C_{60} ion source.¹¹⁰

The ability of this instrument to successfully analyze lipids directly from tissue and cells has been recently demonstrated.¹⁰⁴ Intact phospholipids of a single neuron from an *aplysia californica* sea slug (see Figure 1.10) were resolved. With the help of MALDI, tandem MS, and knowledge of matrix effects and respective fragmentation pathways, peaks at m/z 768 and m/z 784 were identified as the sodium- and potassium-adducts of ether-containing glycerophosphocholine at m/z 746, respectively. In addition, the peaks at m/z 709.5 and m/z 725 were identified as a high mass fragments of m/z 768 and m/z 784, respectively.

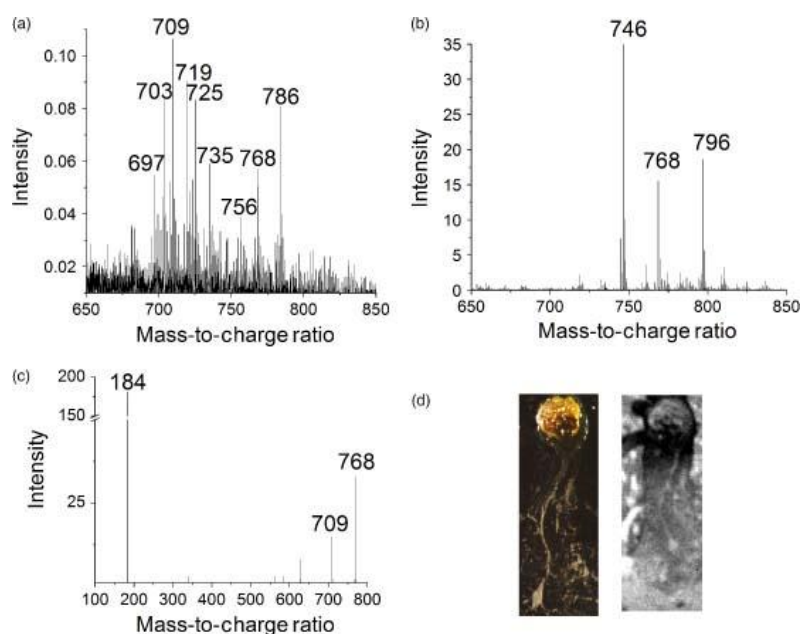


Figure 1.10. Lipid profile obtained from a single neuron with SIMS (a) and from a compilation of neurons with MALDI (b). The tandem MS spectrum shows that m/z 709 and 184 are major fragments of m/z 768.5, the sodiated adduct of major lipid component m/z 746.5 (c). Optical image (d, left) and black and white SIMS total ion image (d, right) of cultured aplysia neuron on silicon wafer (image size 2.00×4.75 mm).¹⁰⁴

The Vickerman group at the Surface Analysis Centre in Manchester, in cooperation with Ionoptika Ltd. and Scientific Analysis Instruments (SAI), has developed a new SIMS instrument called the Ionoptika J105 3D Chemical Imager (see Figure 1.11).¹⁰⁹ The instrument employs a 40 keV C_{60}^+ ion gun that is operated in a direct current (dc) mode under high vacuum conditions. Secondary ions extracted with high voltage are collisionally cooled and energy-filtered before being pulsed into a buncher; where they are focused in the time domain and subsequently injected into a harmonic

field ToF mass analyzer. A collision cell is positioned after the buncher for tandem MS analysis.

The time focusing buncher is the crucial element to the versatility and performance of the instrument. The buncher is responsible for decoupling the secondary ion beam with the ion formation event, a necessary procedure for combining a continuous secondary ion beam with a ToF mass analyzer. In addition, the resolution of the buncher's time focus defines the spectral mass resolution, which for the J105 Chemical Imager is specified to be 10000 at mass 500. High ion transmission through the buncher makes the system highly sensitive and reduces duty cycle, making analyses quick and easy.

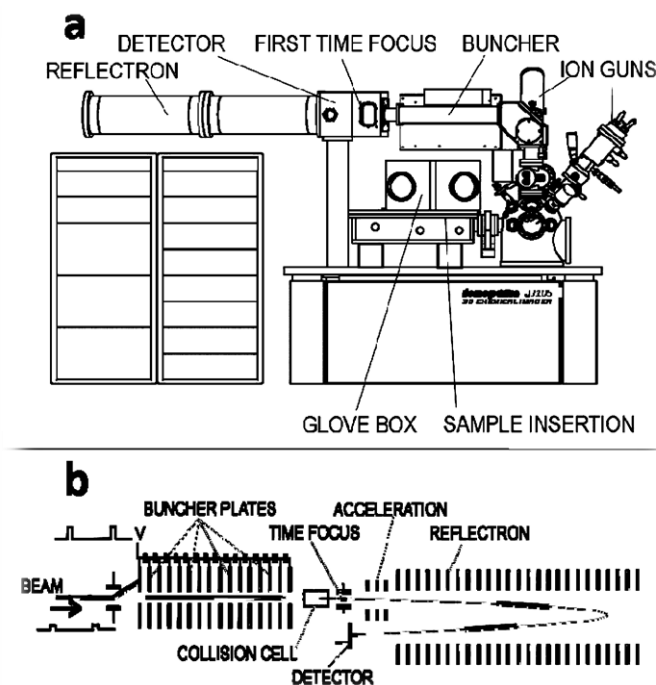


Figure 1.11. Schematic of Ionoptika J105 3D Chemical Imager (a) and close up diagram of time focusing buncher, collision cell for tandem MS acquisitions and ToF mass analyze (b).¹⁰⁹

The Ionoptika J105 3D Chemical Imager has been designed with the specific purpose of analyzing biological samples. Accessories such as a glove box for storing and facilitating the transfer of frozen hydrated samples into the vacuum and a cryogenic compatible stage for maintaining sample integrity throughout the analysis are incorporated for optimal biological sample management. The ability of the instrument to construct 3-dimensional images of lipid fragments directly from frozen hydrated cells is demonstrated in Figure 1.12.¹¹¹

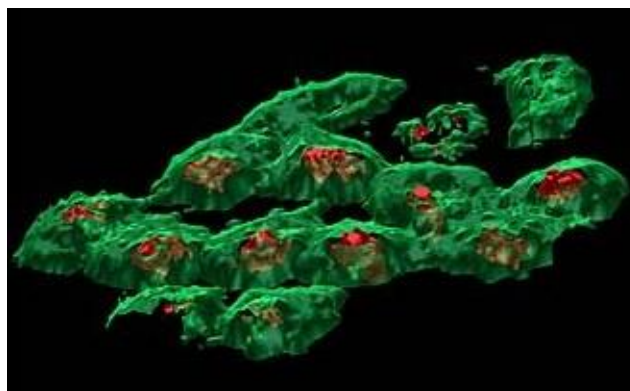


Figure 1.12. 3D biochemical images of frozen hydrated HeLa M cells depicting localizations of phosphocholine headgroup (m/z 184, green) on the cell membranes and adenine (m/z 136.1, red) localized to the nucleus obtained on the Ionoptika J105 3D Chemical Imager.^{22, 111}

1.10. Conclusions

Since lipids play a significant role in basic cellular processes, it is important to study and understand these molecules. As illustrated here, ToF-SIMS is an emerging platform for lipid-based imaging studies. The technique has been successfully applied to elucidating a number of biological quandaries and complex biological processes. Several recent achievements in both technology and methodology promise to further expand the impact of these studies.

Although these are important qualities associated with the techniques, ToF-SIMS has still not been widely applied to solving biological problems or in clinical research. Hopefully the advent of newer high performance instruments, such as the C_{60}^+ QSTAR and J105, which are designed specifically to target biological sample applications, will break down this wall and push ToF-SIMS further into the field of biochemistry and biomedicine.

1.11. References

1. Braun, R. M.; Beyder, A.; Xu, J. Y.; Wood, M. C.; Ewing, A. G.; Winograd, N., Spatially resolved detection of attomole quantities of organic molecules localized in picoliter vials using time-of-flight secondary ion mass spectrometry. *Analytical Chemistry* **1999**, *71* (16), 3318-3324.
2. Kollmer, F., Cluster primary ion bombardment of organic materials. *Applied Surface Science* **2004**, *231*, 153-158.
3. Fuchs, B.; Suss, R.; Schiller, J., An update of MALDI-TOF mass spectrometry in lipid research. *Prog. Lipid. Res.* **2010**, *49* (4), 450-475.
4. Murphy, R. C.; Hankin, J. A.; Barkley, R. M., Imaging of lipid species by MALDI mass spectrometry. *J. Lipid Res.* **2009**, *50*, S317-S322.
5. Sullards, M. C.; Chen, Y.; Liu, Y.; Merrill, A. H., Imaging of lipids directly from brain tissue via matrix assisted laser desorption ionization Time-of-Flight Mass Spectrometry (MALDI TOF MS). *J. Neurochem.* **2010**, *113*, 92.
6. Woods, A. S.; Jackson, S. N., Brain tissue lipidomics: Direct probing using matrix-assisted laser desorption/ionization mass spectrometry. *Aaps Journal* **2006**, *8* (2), E391-E395.
7. Dill, A. L.; Ifa, D. R.; Manicke, N. E.; Zheng, O. Y.; Cooks, R. G., Mass spectrometric imaging of lipids using desorption electrospray ionization. *Journal of Chromatography B-Analytical Technologies in the Biomedical and Life Sciences* **2009**, *877* (26), 2883-2889.
8. Gerbig, S.; Takats, Z., Analysis of triglycerides in food items by desorption electrospray ionization mass spectrometry. *Rapid Communications in Mass Spectrometry* **2010**, *24* (15), 2186-2192.
9. Girod, M.; Shi, Y. Z.; Cheng, J. X.; Cooks, R. G., Desorption Electrospray Ionization Imaging Mass Spectrometry of Lipids in Rat Spinal Cord. *Journal of the American Society for Mass Spectrometry* **2010**, *21* (7), 1177-1189.
10. Ifa, D. R.; Wiseman, J. M.; Song, Q. Y.; Cooks, R. G., Development of capabilities for imaging mass spectrometry under ambient conditions with desorption electrospray ionization (DESI). *International Journal of Mass Spectrometry* **2007**, *259* (1-3), 8-15.
11. Li, M.; Chen, H.; Yang, X.; Chen, J.; Li, C., Direct quantification of organic acids in aerosols by desorption electrospray ionization mass spectrometry. *Atmospheric Environment* **2009**, *43* (17), 2717-2720.
12. Manicke, N. E.; Nefliu, M.; Wu, C. P.; Woods, J. W.; Reiser, V.; Hendrickson, R. C.; Cooks, R. G., Imaging of Lipids in Atheroma by Desorption Electrospray Ionization Mass Spectrometry. *Analytical Chemistry* **2009**, *81* (21), 8702-8707.

13. Manicke, N. E.; Wiseman, J. M.; Ifa, D. R.; Cooks, R. G., Desorption electrospray ionization (DESI) mass Spectrometry and tandem mass spectrometry (MS/MS) of phospholipids and sphingolipids: Ionization, adduct formation, and fragmentation. *Journal of the American Society for Mass Spectrometry* **2008**, *19* (4), 531-543.
14. Paglia, G.; Ifa, D. R.; Wu, C. P.; Corso, G.; Cooks, R. G., Desorption Electrospray Ionization Mass Spectrometry Analysis of Lipids after Two-Dimensional High-Performance Thin-Layer Chromatography Partial Separation. *Analytical Chemistry* **2010**, *82* (5), 1744-1750.
15. Wiseman, J. M.; Ifa, D. R.; Song, Q. Y.; Cooks, R. G., Tissue imaging at atmospheric pressure using desorption electrospray ionization (DESI) mass spectrometry. *Angewandte Chemie-International Edition* **2006**, *45* (43), 7188-7192.
16. Wiseman, J. M.; Ifa, D. R.; Venter, A.; Cooks, R. G., Ambient molecular imaging by desorption electrospray ionization mass spectrometry. *Nature Protocols* **2008**, *3* (3), 517-524.
17. Wolstenholme, R.; Bradshaw, R.; Clench, M. R.; Francese, S., Study of latent fingermarks by matrix-assisted laser desorption/ionisation mass spectrometry imaging of endogenous lipids. *Rapid Communications in Mass Spectrometry* **2009**, *23* (19), 3031-3039.
18. Wu, C. P.; Ifa, D. R.; Manicke, N. E.; Cooks, R. G., Molecular imaging of adrenal gland by desorption electrospray ionization mass spectrometry. *Analyst* **2010**, *135* (1), 28-32.
19. McDonnell, L. A.; Heeren, R. M. A., Imaging mass spectrometry. *Mass Spectrom. Rev.* **2007**, *26* (4), 606-643.
20. Pol, J.; Strohmalm, M.; Havlicek, V.; Volny, M., Molecular mass spectrometry imaging in biomedical and life science research. *Histochemistry and Cell Biology* **2010**, *134* (5), 423-443.
21. van Hove, E. R. A.; Smith, D. F.; Heeren, R. M. A., A concise review of mass spectrometry imaging. *Journal of Chromatography A* **2010**, *1217* (25), 3946-3954.
22. Vickerman, J. C., Molecular Imaging and Depth Profiling by Mass Spectrometry – SIMS, MALDI or DESI? *Analyst* **2011**.
23. Esquenazi, E.; Yang, Y. L.; Watrous, J.; Gerwick, W. H.; Dorrestein, P. C., Imaging mass spectrometry of natural products. *Natural Product Reports* **2009**, *26* (12), 1521-1534.
24. Heeren, R. M. A.; McDonnell, L. A.; Amstalden, E.; Luxembourg, S. L.; Altelaar, A. F. M.; Piersma, S. R., Why don't biologists use SIMS? A critical evaluation of imaging MS. *Applied Surface Science* **2006**, *252*, 6827-6835.
25. Jurchen, J. C.; Rubakhin, S. S.; Sweedler, J. V., MALDI-MS imaging of features smaller than the size of the laser beam. *Journal of the American Society for Mass Spectrometry* **2005**, *16* (10), 1654-1659.
26. Holle, A.; Haase, A.; Kayser, M.; Hohndorf, J., Optimizing UV laser focus profiles for improved MALDI performance. *Journal of Mass Spectrometry* **2006**, *41* (6), 705-716.

27. Hankin, J. A.; Barkley, R. M.; Murphy, R. C., Sublimation as a method of matrix application for mass spectrometric imaging. *Journal of the American Society for Mass Spectrometry* **2007**, *18*, 1646-1652.
28. Bond, P.; McEwen, A. B.; Wood, S. G.; Clench, M., MALDI- Imaging of Endogenous Lipids in Tumour Xenographs. *Drug Metabolism Reviews* **2010**, *42*, 48-49.
29. Fournier, I.; Wisztorski, M.; Salzet, M., Tissue imaging using MALDI-MS: a new frontier of histopathology proteomics. *Expert Review of Proteomics* **2008**, *5* (3), 413-424.
30. Liu, Y.; Chen, Y.; Momin, A.; Shaner, R.; Wang, E.; Bowen, N. J.; Matyunina, L. V.; Walker, L. D.; McDonald, J. F.; Sullards, M. C.; Merrill, A. H., Jr., Elevation of sulfatides in ovarian cancer: An integrated transcriptomic and lipidomic analysis including tissue-imaging mass spectrometry. *Molecular Cancer* **2010**, *9*, Article No.: 186.
31. Rauser, S.; Deininger, S. O.; Suckau, D.; Hofler, H.; Walch, A., Approaching MALDI molecular imaging for clinical proteomic research: current state and fields of application. *Expert Review of Proteomics* **2010**, *7* (6), 927-941.
32. Stoeckli, M.; Knochenmuss, R.; McCombie, G.; Mueller, D.; Rohner, T.; Staab, D.; Wiederhold, K. H., MALDI MS imaging of amyloid. *Amyloid, Prions, and Other Protein Aggregates, Pt B* **2006**, *412*, 94-106.
33. Reyzer, M. L.; Hsieh, Y. S.; Ng, K.; Korfmacher, W. A.; Caprioli, R. M., Direct analysis of drug candidates in tissue by matrix-assisted laser desorption/ionization mass spectrometry. *Journal of Mass Spectrometry* **2003**, *38* (10), 1081-1092.
34. Wisztorski, M.; Lemaire, R.; Stauber, J.; Menguellet, S. A.; Jardin-Mathe, O.; Day, R.; Salzet, M.; Fournier, I., MALDI imaging: a new technology to discover and validate new biomarkers. *M S-Medecine Sciences* **2007**, *23*, 31-36.
35. Griffiths, W. J.; Wang, Y. Q., Mass spectrometry: from proteomics to metabolomics and lipidomics. *Chemical Society Reviews* **2009**, *38* (7), 1882-1896.
36. Malm, J.; Giannaras, D.; Riehle, M. O.; Gadegaard, N.; Sjoval, P., Fixation and Drying Protocols for the Preparation of Cell Samples for Time-of-Flight Secondary Ion Mass Spectrometry Analysis. *Analytical Chemistry* **2009**, *81* (17), 7197-7205.
37. Nygren, H.; Borner, K.; Malmberg, P.; Hagenhoff, B., Localization of cholesterol in rat cerebellum with imaging TOF-SIMS - Effect of tissue preparation. *Applied Surface Science* **2006**, *252* (19), 6975-6981.
38. Nygren, H.; Borner, K.; Malmberg, P.; Tallarek, E.; Hagenhoff, B., Imaging TOF-SIMS of rat kidney prepared by high-pressure freezing. *Microscopy Research and Technique* **2005**, *68* (6), 329-334.
39. Chandra, S.; Bernius, M. T.; Morrison, G. H., Intracellular-localization of diffusible elements in frozen-hydrated biological species with ion microscopy. *Analytical Chemistry* **1986**, *58* (2), 493-496.
40. Chandra, S., Challenges of biological sample preparation for SIMS imaging of elements and molecules at subcellular resolution. *Applied Surface Science* **2008**, *255* (4), 1273-1284.
41. Kurczyk, M. E.; Piehowski, P. D.; Parry, S. A.; Jiang, M.; Chen, G.; Ewing, A. G.; Winograd, N., Which is more important in bioimaging SIMS experiments-The sample

preparation or the nature of the projectile? *Applied Surface Science* **2008**, *255* (4), 1298-1304.

42. Cheng, J.; Wucher, A.; Winograd, N., Molecular depth profiling with cluster ion beams. *Journal of Physical Chemistry B* **2006**, *110* (16), 8329-8336.

43. Piwowar, A. M.; Fletcher, J. S.; Kordys, J.; Lockyer, N. P.; Winograd, N.; Vickerman, J. C., Effects of Cryogenic Sample Analysis on Molecular Depth Profiles with TOF-Secondary Ion Mass Spectrometry. *Analytical Chemistry* **2010**, *82* (19), 8291-8299.

44. Lanekoff, I.; Kurczy, M. E.; Hill, R.; Fletcher, J. S.; Vickerman, J. C.; Winograd, N.; Sjovall, P.; Ewing, A. G., Time of Flight Mass Spectrometry Imaging of Samples Fractured In Situ with a Spring-Loaded Trap System. *Analytical Chemistry* **2010**, *82* (15), 6652-6659.

45. Jones, E. A.; Lockyer, N. P.; Vickerman, J. C., Depth profiling brain tissue sections with a 40 keV C-60(+) primary ion beam. *Analytical Chemistry* **2008**, *80* (6), 2125-2132.

46. Piwowar, A. M.; Lockyer, N. P.; Vickerman, J. C., Salt Effects on Ion Formation in Desorption Mass Spectrometry: An Investigation into the Role of Alkali Chlorides on Peak Suppression in Time-of-Flight-Secondary Ion Mass Spectrometry. *Analytical Chemistry* **2009**, *81* (3), 1040-1048.

47. McGuinness, C. L.; Shaporenko, A.; Zharnikov, M.; Walker, A. V.; Allara, D. L., Molecular self-assembly at bare semiconductor surfaces: Investigation of the chemical and electronic properties of the alkanethiolate-GaAs(001) interface. *Journal of Physical Chemistry C* **2007**, *111* (11), 4226-4234.

48. Chu, P. K.; Odom, R. W.; Reich, D. F., Analysis of surface particles by time-of-flight secondary ion mass spectrometry. *Materials Chemistry and Physics* **1996**, *43* (2), 87-94.

49. Mahoney, C. M., Cluster secondary ion mass spectrometry of polymers and related materials. *Mass Spectrom. Rev.* **2010**, *29* (2), 247-293.

50. Mathieu, H. J.; Chevolut, Y.; Ruiz-Taylor, L.; Leonard, D., Engineering and Characterization of Polymer Surfaces for Biomedical Applications. *Radiation Effects on Polymers for Biological Use* **2003**, *162*, 1-34.

51. Matsubara, T.; Hayashi, A., FAB Mass-spectrometry of lipids. *Prog. Lipid. Res.* **1991**, *30* (4), 301-322.

52. Barber, M.; Bordoli, R. S.; Sedgwick, R. D.; Tyler, A. N., Fast atom bombardment of solids (FAB) - A new ion-source for mass-spectrometry. *Journal of the Chemical Society-Chemical Communications* **1981**, (7), 325-327.

53. Jensen, N. J.; Tomer, K. B.; Gross, M. L., FAB MS/MS for phosphatidylinositol, -glycerol, phosphatidylethanolamine and other complex phospholipids. *Lipids* **1987**, *22* (7), 480-489.

54. Winograd, N., The magic of cluster SIMS. *Analytical Chemistry* **2005**, *77* (7), 142A-149A.

55. Xu, J.; Ostrowski, S.; Szakal, C.; Ewing, A. G.; Winograd, N., ToF-SIMS imaging with cluster ion beams. *Applied Surface Science* **2004**, *231*, 159-163.

56. Postawa, Z.; Czerwinski, B.; Szewczyk, M.; Smiley, E. J.; Winograd, N.; Garrison, B. J., Microscopic insights into the sputtering of Ag{111} induced by C-60 and Ga bombardment. *Journal of Physical Chemistry B* **2004**, *108* (23), 7831-7838.
57. Postawa, Z.; Czerwinski, B.; Winograd, N.; Garrison, B. J., Microscopic insights into the sputtering of thin organic films on Ag{111} induced by C-60 and Ga bombardment. *Journal of Physical Chemistry B* **2005**, *109* (24), 11973-11979.
58. Ostrowski, S. G.; Szakal, C.; Kozole, J.; Roddy, T. P.; Xu, J. Y.; Ewing, A. G.; Winograd, N., Secondary ion MS imaging of lipids in picoliter vials with a buckminsterfullerene ion source. *Analytical Chemistry* **2005**, *77* (19), 6190-6196.
59. Sjoval, P.; Lausmaa, J.; Johansson, B., Mass spectrometric imaging of lipids in brain tissue. *Analytical Chemistry* **2004**, *76* (15), 4271-4278.
60. Sjoval, P.; Johansson, B.; Lausmaa, J., Localization of lipids in freeze-dried mouse brain sections by imaging TOF-SIMS. *Applied Surface Science* **2006**, *252* (19), 6966-6974.
61. Benabdellah, F.; Seyer, A.; Quinton, L.; Touboul, D.; Brunelle, A.; Laprevote, O., Mass spectrometry imaging of rat brain sections: nanomolar sensitivity with MALDI versus nanometer resolution by TOF-SIMS. *Analytical and Bioanalytical Chemistry* **2010**, *396* (1).
62. Hankin, J. A.; Murphy, R. C., Relationship between MALDI IMS Intensity and Measured Quantity of Selected Phospholipids in Rat Brain Sections. *Analytical Chemistry* **2010**, *82* (20), 8476-8484.
63. Borner, K.; Nygren, H.; Hagenhoff, B.; Malmberg, P.; Tallarek, E.; Mansson, J. E., Distribution of cholesterol and galactosylceramide in rat cerebellar white matter. *Biochimica Et Biophysica Acta-Molecular and Cell Biology of Lipids* **2006**, *1761* (3), 335-344.
64. Nygren, H.; Borner, K.; Hagenhoff, B.; Malmberg, P.; Mansson, J. E., Localization of cholesterol, phosphocholine and galactosylceramide in rat cerebellar cortex with imaging TOF-SIMS equipped with a bismuth cluster ion source. *Biochimica Et Biophysica Acta-Molecular and Cell Biology of Lipids* **2005**, *1737* (2-3), 102-110.
65. Nygren, H.; Malmberg, P., High resolution imaging by organic secondary ion mass spectrometry. *Trends in Biotechnology* **2007**, *25* (11), 499-504.
66. Pernber, Z.; Richter, K.; Mansson, J. E.; Nygren, H., Sulfatide with different fatty acids has unique distributions in cerebellum as imaged by Time-Of-Flight Secondary Ion Mass Spectrometry (TOF-SIMS). *Biochimica Et Biophysica Acta-Molecular and Cell Biology of Lipids* **2007**, *1771* (2), 202-209.
67. Amaya, K. R.; Monroe, E. B.; Sweedler, J. V.; Clayton, D. F., Lipid imaging in the zebra finch brain with secondary ion mass spectrometry. *International Journal of Mass Spectrometry* **2007**, *260* (2-3), 121-127.
68. Debois, D.; Brunelle, A.; Laprevote, O., Attempts for molecular depth profiling directly on a rat brain tissue section using fullerene and bismuth cluster ion beams. *International Journal of Mass Spectrometry* **2007**, *260* (2-3), 115-120.

69. Monroe, E. B.; Annangudi, S. R.; Hatcher, N. G.; Gutstein, H. B.; Rubakhin, S. S.; Sweedler, J. V., SIMS and MALDI MS imaging of the spinal cord. *Proteomics* **2008**, *8* (18), 3746-3754.
70. Debois, D.; Bralet, M. P.; Le Naour, F.; Brunelle, A.; Laprevote, O., In Situ Lipidomic Analysis of Nonalcoholic Fatty Liver by Cluster TOF-SIMS Imaging. *Analytical Chemistry* **2009**, *81* (8), 2823-2831.
71. Fletcher, J. S., Lockyer, N. P. and Vickerman, J. C., Molecular SIMS imaging; spatial resolution and molecular sensitivity: have we reached the end of the road? Is there light at the end of the tunnel? *Surface and Interface Analysis* **2010**.
72. Nygren, H.; Malmberg, P.; Kriegeskotte, C.; Arlinghaus, H. F., Bioimaging TOF-SIMS: localization of cholesterol in rat kidney sections. *Febs Letters* **2004**, *566* (1-3), 291-293.
73. Malmberg, P.; Nygren, H.; Richter, K.; Chen, Y.; Dangardt, F.; Friberg, P.; Magnusson, Y., Imaging of lipids in human adipose tissue by cluster ion TOF-SIMS. *Microscopy Research and Technique* **2007**, *70*, 828-835.
74. Belazi, D.; Sole-Domenech, S.; Johansson, B.; Schalling, M.; Sjoval, P., Chemical analysis of osmium tetroxide staining in adipose tissue using imaging ToF-SIMS. *Histochemistry and Cell Biology* **2009**, *132* (1), 105-115.
75. Magnusson, Y.; Friberg, P.; Sjoval, P.; Dangardt, F.; Malmberg, P.; Chen, Y., Lipid imaging of human skeletal muscle using TOF-SIMS with bismuth cluster ion as a primary ion source. *Clinical Physiology and Functional Imaging* **2008**, *28* (3), 202-209.
76. Tahallah, N.; Brunelle, A.; De La Porte, S.; Laprevote, O., Lipid mapping in human dystrophic muscle by cluster-time-of-flight secondary ion mass spectrometry imaging. *J. Lipid Res.* **2008**, *49* (2), 438-454.
77. Malmberg, P.; Borner, K.; Chen, Y.; Friberg, P.; Hagenhoff, B.; Mansson, J. E.; Nygren, H., Localization of lipids in the aortic wall with imaging TOF-SIMS. *Biochimica Et Biophysica Acta-Molecular and Cell Biology of Lipids* **2007**, *1771* (2), 185-195.
78. Gong, H.; Amemiya, T.; Takaya, K.; Tozu, M.; Ohashi, Y., Time-of-flight secondary ion mass spectrometry of fatty acids in rat retina. *Applied Surface Science* **2003**, *203*, 734-737.
79. Touboul, D.; Brunelle, A.; Halgand, F.; De La Porte, S.; Laprevote, O., Lipid imaging by gold cluster time-of-flight secondary ion mass spectrometry: application to Duchenne muscular dystrophy. *J. Lipid Res.* **2005**, *46* (7), 1388-1395.
80. Touboul, D.; Roy, S.; Germain, D. P.; Chaminade, P.; Brunelle, A.; Laprevote, O., MALDI-TOF and cluster-TOF-SIMS imaging of Fabry disease biomarkers. *International Journal of Mass Spectrometry* **2007**, *260* (2-3), 158-165.
81. Brulet, M.; Seyer, A.; Edelman, A.; Brunelle, A.; Fritsch, J.; Ollero, M.; Laprevote, O., Lipid mapping of colonic mucosa by cluster TOF-SIMS imaging and multivariate analysis in cfr knockout mice. *J. Lipid Res.* **2010**, *51* (10), 3034-3045.
82. Debois, D.; Hamze, K.; Guerineau, V.; Le Caer, J. P.; Holland, I. B.; Lopes, P.; Ouazzani, J.; Seror, S. J.; Brunelle, A.; Laprevote, O., In situ localisation and

quantification of surfactins in a *Bacillus subtilis* swarming community by imaging mass spectrometry. *Proteomics* **2008**, *8* (18), 3682-3691.

83. Seyer, A.; Einhorn, J.; Brunelle, A.; Laprevote, O., Localization of Flavonoids in Seeds by Cluster Time-of-Flight Secondary Ion Mass Spectrometry Imaging. *Analytical Chemistry* **2010**, *82* (6), 2326-2333.

84. Thiel, V.; Heim, C.; Arp, G.; Hahmann, U.; Sjoval, P.; Lausmaa, J., Biomarkers at the microscopic range: ToF-SIMS molecular imaging of Archaea-derived lipids in a microbial mat. *Geobiology* **2007**, *5* (4), 413-421.

85. Colliver, T. L.; Brummel, C. L.; Pacholski, M. L.; Swanek, F. D.; Ewing, A. G.; Winograd, N., Atomic and molecular imaging at the single-cell level with TOF-SIMS. *Analytical Chemistry* **1997**, *69* (13), 2225-2231.

86. Pacholski, M. L.; Cannon, D. M.; Ewing, A. G.; Winograd, N., Static time-of-flight secondary ion mass spectrometry imaging of freeze-fractured, frozen-hydrated biological membranes. *Rapid Communications in Mass Spectrometry* **1998**, *12* (18), 1232-+.

87. Ostrowski, S. G.; Van Bell, C. T.; Winograd, N.; Ewing, A. G., Mass spectrometric imaging of highly curved membranes during Tetrahymena mating. *Science* **2004**, *305* (5680), 71-73.

88. Kurczy, M. E.; Piehowski, P. D.; Van Bell, C. T.; Heien, M. L.; Winograd, N.; Ewing, A. G., Mass spectrometry imaging of mating Tetrahymena show that changes in cell morphology regulate lipid domain formation. *Proceedings of the National Academy of Sciences of the United States of America* **2010**, *107* (7), 2751-2756.

89. Monroe, E. B.; Jurchen, J. C.; Lee, J.; Rubakhin, S. S.; Sweedler, J. V., Vitamin E imaging and localization in the neuronal membrane. *Journal of the American Chemical Society* **2005**, *127* (35), 12152-12153.

90. Carado, A.; Kozole, J.; Passarelli, M.; Winograd, N.; Loboda, A.; Bunch, J.; Wingate, J.; Hankin, J.; Murphy, R., Biological tissue imaging with a hybrid cluster SIMS quadrupole time-of-flight mass spectrometer. *Applied Surface Science* **2008**, *255* (4), 1572-1575.

91. Arlt, S.; Beisiegel, U.; Kontush, A., Lipid peroxidation in neurodegeneration: new insights into Alzheimer's disease. *Curr. Opin. Lipidology* **2002**, *13* (3), 289-294.

92. Dexter, D. T.; Carter, C. J.; Wells, F. R.; Javoyagid, F.; Agid, Y.; Lees, A.; Jenner, P.; Marsden, C. D., BASAL LIPID-PEROXIDATION IN SUBSTANTIA NIGRA IS INCREASED IN PARKINSONS-DISEASE. *J. Neurochem.* **1989**, *52* (2), 381-389.

93. Yang, H. J.; Ishizaki, I.; Sanada, N.; Zaima, N.; Sugiura, Y.; Yao, I.; Ikegami, K.; Setou, M., Detection of characteristic distributions of phospholipid head groups and fatty acids on neurite surface by time-of-flight secondary ion mass spectrometry. *Medical Molecular Morphology* **2010**, *43* (3), 158-164.

94. Altelaar, A. F. M.; Klinkert, I.; Jalink, K.; de Lange, R. P. J.; Adan, R. A. H.; Heeren, R. M. A.; Piersma, S. R., Gold-enhanced biomolecular surface imaging of cells and tissue by SIMS and MALDI mass spectrometry. *Analytical Chemistry* **2006**, *78* (3), 734-742.

95. Sun, S.; Szakal, C.; Roll, T.; Mazarov, P.; Wucher, A.; Winograd, N., Use of C-60 cluster projectiles for sputter depth profiling of polycrystalline metals. *Surface and Interface Analysis* **2004**, *36* (10), 1367-1372.
96. Sun, S.; Wucher, A.; Szakal, C.; Winograd, N., Depth profiling of polycrystalline multilayers using a Buckminsterfullerene projectile. *Applied Physics Letters* **2004**, *84* (25), 5177-5179.
97. Cheng, J.; Winograd, N., Depth profiling of peptide films with TOF-SIMS and a C-60 probe. *Analytical Chemistry* **2005**, *77* (11), 3651-3659.
98. Mao, D.; Wucher, A.; Winograd, N., Molecular Depth Profiling with Cluster Secondary Ion Mass Spectrometry and Wedges. *Analytical Chemistry* **2010**, *82* (1), 57-60.
99. Fletcher, J. S.; Lockyer, N. P.; Vaidyanathan, S.; Vickerman, J. C., TOF-SIMS 3D biomolecular imaging of *Xenopus laevis* oocytes using buckminsterfullerene (C-60) primary ions. *Analytical Chemistry* **2007**, *79* (6), 2199-2206.
100. Yang, H. J.; Sugiura, Y.; Ishizaki, I.; Sanada, N.; Ikegami, K.; Zaima, N.; Shrivastava, K.; Setou, M., Imaging of lipids in cultured mammalian neurons by matrix assisted laser/desorption ionization and secondary ion mass spectrometry. *Surface and Interface Analysis* **2010**, *42* (10-11), 1606-1611.
101. Sjovall, P.; Lausmaa, J.; Nygren, H.; Carlsson, L.; Malmberg, P., Imaging of membrane lipids in single cells by imprint-imaging time-of-flight secondary ion mass spectrometry. *Analytical Chemistry* **2003**, *75* (14), 3429-3434.
102. Roddy, T. P.; Cannon, D. M.; Meserole, C. A.; Winograd, N.; Ewing, A. G., Imaging of freeze-fractured cells with in situ fluorescence and time-of-flight secondary ion mass spectrometry. *Analytical Chemistry* **2002**, *74* (16), 4011-4019.
103. Kurczyk, M. E.; Kozole, J.; Parry, S. A.; Piehowski, P. D.; Winograd, N.; Ewing, A. G., Relative quantification of cellular sections with molecular depth profiling ToF-SIMS imaging. *Applied Surface Science* **2008**, *255* (4), 1158-1161.
104. Passarelli, M. K.; Winograd, N., Characterizing *in situ* Glycerophospholipids with SIMS and MALDI Methodologies. *Surf. Interface Anal.* **2010**.
105. Piehowski, P. D.; Carado, A. J.; Kurczyk, M. E.; Ostrowski, S. G.; Heien, M. L.; Winograd, N.; Ewing, A. G., MS/MS Methodology To Improve Subcellular Mapping of Cholesterol Using TOF-SIMS. *Analytical Chemistry* **2008**, *80* (22), 8662-8667.
106. Kleinfeld, A. M.; Kampf, J. P.; Lechene, C., Transport of C-13-oleate in adipocytes measured using multi imaging mass Spectrometry. *Journal of the American Society for Mass Spectrometry* **2004**, *15* (11), 1572-1580.
107. Boxer, S. G.; Kraft, M. L.; Weber, P. K., Advances in Imaging Secondary Ion Mass Spectrometry for Biological Samples. *Annual Review of Biophysics* **2009**, *38*, 53-74.
108. Kraft, M. L.; Weber, P. K.; Longo, M. L.; Hutcheon, I. D.; Boxer, S. G., Phase separation of lipid membranes analyzed with high-resolution secondary ion mass spectrometry. *Science* **2006**, *313* (5795), 1948-1951.

109. Fletcher, J. S.; Rabbani, S.; Henderson, A.; Blenkinsopp, P.; Thompson, S. P.; Lockyer, N. P.; Vickerman, J. C., A New Dynamic in Mass Spectral Imaging of Single Biological Cells. *Analytical Chemistry* **2008**, *80* (23), 9058-9064.
110. Carado, A.; Passarelli, M. K.; Kozole, J.; Wingate, J. E.; Winograd, N.; Loboda, A. V., C-60 Secondary Ion Mass Spectrometry with a Hybrid-Quadrupole Orthogonal Time-of-Flight Mass Spectrometer. *Analytical Chemistry* **2008**, *80* (21), 7921-7929.
111. Fletcher, J. S.; Rabbani, S.; Henderson, A.; Lockyer, N. P.; Vickerman, J. C., Three-dimensional mass spectral imaging of HeLa-M cells - sample preparation, data interpretation and visualisation. *Rapid Communications in Mass Spectrometry* **2011**, *25* (7), 925-932.

Chapter 2

C₆₀-QSTAR Instrument Development

A portion of this chapter have been modified from its original source: Carado, A.; Passarelli, M. K.; Kozole, J.; Wingate, J. E.; Winograd, N.; Loboda, A. V. *Anal. Chem.* 2008, 80, 7921.

Abstract:

For the past decade, cluster SIMS and commercial mass spectrometers have been developing independently from each other. In the field of SIMS, the emergence of cluster sources greatly improved the molecular ion yields of biologically-relevant molecules and has propelled the technique into the field of bioanalytics. Simultaneously, the success of MALDI and ESI methodologies in mass spectrometry-based proteomics research has led to the world-wide commercialization of mass spectrometers. As a result, these systems are now found in most bioanalytical labs. This chapter will review the basic theories of SIMS, the development of cluster SIMS, and the merging of a state-of-the-art C₆₀ SIMS source with a commercial hybrid mass spectrometer. The overall design elements of this instrument are discussed and its performance, including ion transmission, signal-to-noise, mass resolution, mass accuracy, and tandem mass spectrometry capabilities, is demonstrated.¹

Since the development of the prototype SIMS mass spectrometer, several modifications have been made to improve the performance and expand functionality. The installation of a new C₆₀⁺ ion source, secondary electron/ion detector (SED) and

updated stage rastering software all improved imaging capabilities. The new setup allows for visualization of the ion beam in real-time, resulting in quick focusing and profile optimization. The inclusion of updated stage rastering software, e.g. oMALDITM Server 5.1, significantly reduces the acquisition time and improved lateral resolution by taking advantage of the continuous secondary ion beam generation.

2.1. Introduction

SIMS is a versatile ionization technique capable of analyzing a variety of materials, including inorganic samples, such as semiconductors and polymers, as well as organic samples, such as biological tissues, bacterial colonies and pharmaceuticals. The versatility of the technique stems from the variety of projectiles and analysis modes (e.g. static, dynamic and imaging). Depending upon the nature of the sample and analytical inquiry, researchers can select the projectile and analysis mode that would best suit their investigation. Regardless of the variations within the ionization technique, the basic principles that govern SIMS experiments are the same. In this section, the concepts of fluence, sputtering yields, and ion yields are described. By understand the underlining principle of technique, the correct combination of projectile and analysis mode can be selected. In addition, novel methods can be devised to expand the analytical power of the technique.

2.1.1 Fluence

In the field of SIMS there are two fundamental modes of operation based on the primary ion fluence: static and dynamic. Fluence, the quantity of primary ion impacts as a function of sample area, is formulated in Equation 2.1, whereas I_p is the measured primary ion beam current in amperes, T_s is the sputter time in seconds, and the field of view (FoV) is measured in cm^2 .

$$\mathbf{fluence} \left(\frac{\text{ions}}{\text{cm}^2} \right) = \frac{I_p \cdot T_s}{1.6 \times 10^{-19} \cdot (FoV)^2} \text{ Equation 2. 1}$$

Static SIMS represents acquisitions with primary ion fluencies below 10^{12} ions/ cm^2 , while dynamic SIMS represents primary ion fluencies above this limit.

In the static regime, less than 1 % of surface molecules in the top layer are bombarded. As a result, there is a low probability of impacting the same area twice. Intact molecular ion species are typically observed under static conditions; thus these analyses are suitable for studying high molecular weight organic and polymer samples. Static SIMS instruments, such as the Bio-ToF utilized in our lab¹, the Ion-ToF 5 manufactured by IonTOF Gmb, and the Trift 5 manufactured by Ulvac-Phi, typically employ pulsed primary ion beams and ToF mass analyzers. For pulsed systems, the sputter-time variable in Equation 2.1 is obtained by multiplying the number of pulses by the pulse width.

Above the static limit there is a high probability of sampling a previously sampled area. In this regime, there can be an accumulation of impact related damage, which reduces the ability of the technique to detect intact molecular ions. High fluence instruments, such as those associated with the NanoSIMS (Cameca) and the ADEPT-

1010 (Ulvac-Phi), typically employ continuous primary ion beams and scanning based mass analyzers. Due to damage accumulation, analyses are limited to measurements of elemental and isotopic distributions as a function of depth. Despite the highly destructive secondary ion generation process, this method is capable of achieving spatial resolution of at least 50 nm.

2.1.2. Sputtering and ionization theory

During the sputtering process, the primary ion impact induces a cascade of collisions within the sample. A majority of its energy is deposited deep into the sample; however a small proportion recoils back to the surface causing the ejection of surface molecules. The ability of the projectile to desorb material efficiently is measured in terms of sputter yield (Y), which is a function of the total number of desorbed ions and neutral species per primary ion impact (See Equation 2.2). In this equation, A the sputtered area of the sample (cm^2), d the molecular density for the sample, and I_p is the number of primary ions.

$$Y = \frac{Ad}{I_p} \text{ Equation 2.2}$$

Several factors influence sputter yields, such as sample topography, the incident angle of the projectile, temperature, the nature of the sample, the nature of the projectile (e.g. size, charge, intermolecular forces), the primary ion fluence, and the primary ion energy, to name a few. Obtaining a comprehensive understanding of how these ion-sample interactions impact the efficiency of this process is the main focus of

fundamental SIMS research. Studies aimed at optimizing operational parameters have found that secondary ion yields improve with high incidence energies^{2, 3} and heavy projectile masses^{4,5}, at glancing incident angles,⁶⁻¹⁰ and at cryogenic temperature.^{11, 12}

2.1.3 Secondary electrons

Secondary electrons ejected from the material as the primary ion beam is scanned across the surface can be detected with a secondary electron detector (SED) to produce an image. Although these images do not offer any chemical information, they do provide useful topographical and spatial information. The SED is an essential resource for high lateral resolution imaging acquisitions because it can be used to focus the primary ion beam. As a result, an SED was installed in the C₆₀-QSTAR; the installation and utilization associated with this component is discussed later in this chapter.

2.1.4. Secondary ions

Unfortunately, only a small proportion of the materials desorbed from the surface are ionic species. Ion formation can occur during desorption or shortly after desorption in the plume. Ions can be formed by a number of methods, including protonation or deprotonation, adduction and the radical loss of electrons. Fragmentation pathways can also result in ionized species. The number of secondary ions (I_S) can be calculated by the following equation:¹³

$$I_S = I_p \cdot Y_m \cdot \alpha^\pm \cdot \theta_m \cdot \eta \quad \text{Equation 2.3}$$

In this equation, the formation of secondary ions of molecular species m in the positive mode depends upon the ionization probability of the molecule (α^\pm), the sputter yield (Y_m), and the fractional concentration of species m in the surface layer (θ_m). Additional instrument-dependent variables include transmission (η) and primary ion current (I_p). After desorption, secondary ions are extracted in a mass analyzer using an electrostatic potential.

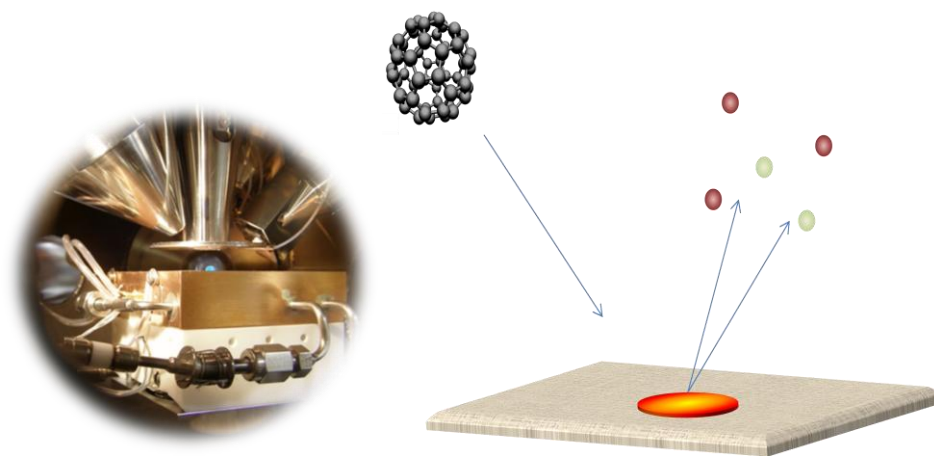


Figure 2.13. Sample stage and diagram demonstration the basic scheme of SIMS

2.1.5. ToF mass analyzers

The ToF detection scheme also offers parallel detection of multiple ionic species, ideal for the analysis of complex biological samples. In a ToF mass analyzer, ions are accelerated with a high voltage, typically 1-5 kV, into a field-free zone where they are separated by their mass-to-charge ratio and subsequently detected. An ion's velocity in the flight tube is directly proportional to its mass and inversely proportional to its charge. This relationship is described in Equation 2.4; where kinetic energy $E_{kinetic}$ is a function of mass (m) and velocity (v), as well as a function of particle charge (q) and potential (V). An ion's time of flight can be calculated, equation 2.5, given the length of the flight tube. For example, a singularly charged ion with a mass of 100 Da accelerated at a 1 keV potential into a 1 meter flight tube, will have a flight time of 45.7 μ s.

$$E_{kinetic} = qV = \frac{1}{2}mv^2 = \frac{1}{2}\left(m\frac{l^2}{t^2}\right) \quad \text{Equation 2.4}$$

$$t = l \cdot \frac{1}{\sqrt{2E}} \cdot \sqrt{\frac{m}{z}} \quad \text{Equation 2.5}$$

Ideally, ions with the same mass-to-charge ratio should have the same flight time, however, the initial temporal, energetic, and spatial distributions among ejected ions can lead to poor mass resolution even for ions with the same mass-to-charge ratio. The first linear-based ToF mass analyzers were not able to control for these factors adequately and their mass resolution suffered significantly as a result. However, technological advances developed over the years, such as delayed extraction techniques and dual stage reflectrons, have greatly improved the resolving power of ToF mass analyzers.

In a reflectron, a series of electrostatic rings decelerates the ion at the end of the flight tube and reflects the ions back into the drift tube. The improvement in mass resolution is two-fold: the reflectron doubles the effective flight tube length and it also corrects for the energy spread among ions with similar mass-to-charge ratios. More specifically, high energy ions penetrate further into the reflectron than lower energy ions with the same mass-to-charge ratio, thus giving them a longer flight path than their less energetic counterparts; the two ions then reach the detector at the same time, with the higher energy ions having traversed a greater distance.

2.1.6. Secondary ion detection

SIMS instruments with time of flight mass analyzers typically employ multi-channel plate (MCP) detectors. Ions separated by their mass-to-charge ratio exiting the field free flight tube are accelerated towards the detector. As the ions hit the MCP plate, a cascade of secondary electrons is initiated down the channels. The secondary electron signal is amplified as it progresses down chevron-shaped channels and is collected by an anode plate at the back of the plate. The signal is collected as a function of time, processes with a time to digital converter (TDC) and interfaced to a computer.

2.1.7. Projectiles

The nature of the projectile plays a pivotal role in the analysis power of SIMS. A wide variety of ion sources each with unique operational capabilities are

commercially available, including C_{60}^+ , Xe^+ , Ar^+ , Ar_n^+ , O^{2-} , SF_5^+ , $(CsI)_nCs^+$, Cs^+ , In^+ , Ga^+ , Au^+ , Au_2^+ , Au_3^+ , Bi^+ , Bi_2^+ and Bi_3^+ . Secondary ion generation is a limiting factor hampering the performance of all SIMS instruments. Improving the efficiency of secondary ion generation will greatly improve instrumental sensitivity, allowing for the detection of minor components in complex samples and probe increasingly smaller samples. Several techniques have been developed to improve sensitivity; one of the most successful is the use of cluster ion sources.

2.1.8. Cluster ions

The development of the cluster ion sources— C_{60}^+ , Bi_3^+ , Au_3^+ and SF_5^+ —has led to a significant increase in the secondary ion yields. Cluster ions have unique characteristics that significantly alter the ion-sample interactions during bombardment. During bombardment, the small atomic projectiles penetrate through the surface layers and are embedded into the bulk of the sample. Conversely, cluster ions shatter upon impact and their incident energy is distributed among the individual atoms in the cluster. For instance, at 20 keV each carbon atom in a C_{60} projectile has the equivalence of $333 \frac{1}{3}$ eV of kinetic energy. Compared to atomic ion projectiles, cluster projectiles offer several advantages, including enhanced sputter yields of organic molecular ions and reduced physical and chemical damage of the sample surface^{14, 15}.

Compared to other cluster sources, C_{60} produces less chemical damage accumulation and is able to retain molecular ion sensitivity in the dynamic regime. As a result, molecular depth profiling and 3-D imaging are a unique new application of C_{60} -

SIMS. During C_{60}^+ bombardment, the impact carves out a crater on the surface of the sample and removes a large volume of material. This special bombardment dynamic localizes energy to the surface, resulting in higher sputter yields and impact induced damage isolated to the surface. Presently, commercially available SIMS instruments do not allow the detection of sputtered material during the sputtering process. Therefore new design considerations are needed for SIMS instruments in order to take advantage of unique properties of the C_{60} .

2.2. The Basic Instrument Design of the QSTAR-XL

The QSTAR XL instrument is a commercial triple quadrupole orthogonal ToF Mass Spectrometer produced by Applied Biosystems MDS/Sciex. The operational modes include, ToF-MS, tandem MS, precursor ion and Q_2 enhancement mode. The multifunctional quadrupoles in the QSTAR allows for the multiple modes of operation and enhance analytical power. In ToF-MS mode the quadrupoles act as ion guides, capable of transmitting a wide mass range of ions simultaneously. In the tandem MS mode, the quadrupoles function as a mass filter, only allowing the transmission of the pre-selected precursor ions.

2.2.1 Differential pumping and collisional cooling

The differential pumping system allows for collisional cooling and focusing of desorbed ions. The QSTAR XL employs a series of apertures and large

turbomolecular pumps, to reduce the pressure between the sample and the ToF mass spectrometer. The low vacuum conditions in the sample and Q_0 regions are responsible for collisional cooling and collisional focusing of the secondary ion during desorption and in the early transmission of the secondary ion beam, respectively. Ions desorbed with excess internal energy, “hot” ions, are prone to fragment or are lost in the quadrupole region due to improper trajectories. In the high pressure region above the sample; these “hot” ions collide with the inert gas and transfer a portion of their energy to the inert gas molecule. A large number of low energy collisions allows for the dissipation of the excess energy with minimal fragmentations. The “cooled” ions have a smaller velocity distribution and are less likely to fragment. The performance advantage of this is twofold; the reduced ion velocity distribution improves the spectral resolution and the reduced fragmentation improves molecular ion sensitivity.

Collisional cooling has been shown to be effective in the analysis of large proteins, ions typically not desorbed in SIMS analyses.¹⁶⁻¹⁸ Experiments performed by Chernushevich and co-workers show that the transmission of large non-covalently bonded complexes in excess of 500 kDa is significantly improved by collisional cooling and collisional focusing.¹⁶ The study reveals a dependence of mass on the pressure required for thermalization. For example, myoglobin, a 16 kDa protein, is sufficiently thermalized and focused at 8 mtorr of pressure, while proeasome 20S, a large protein composed of 28 non-covalently linked subunits and approximately 692 kDa, requires 30 mtorr of pressure. Chernushevich also reported that longer dwell time in the high pressure regions, achieved via ion trapping with a deacceleration field potential, enhances the degree of cooling and decreases the pressure requirement. Unfortunately, this

technique is not effective for ions typically observed with SIMS analyses, like small molecules (< 1000 Da) and large inorganic clusters, such as cesium iodine clusters. As a result, collisional cooling in SIMS-based analyses has proven to be only mildly successful for only a small number of molecules (e. g. progesterone).¹⁹

2.3. Interfacing C₆₀ SIMS and a QSTAR XL commercial mass spectrometer

The QSTAR XL has a highly adaptable source region compatible with various commercially available sources, including atmospheric pressure ionization (API), electrospray ionization (ESI) and matrix-assisted laser desorption ionization (MALDI) and now cluster SIMS. The union of the QSTAR XL mass spectrometer and a C₆₀ ion source is illustrated in the Figure 2.2.²⁰

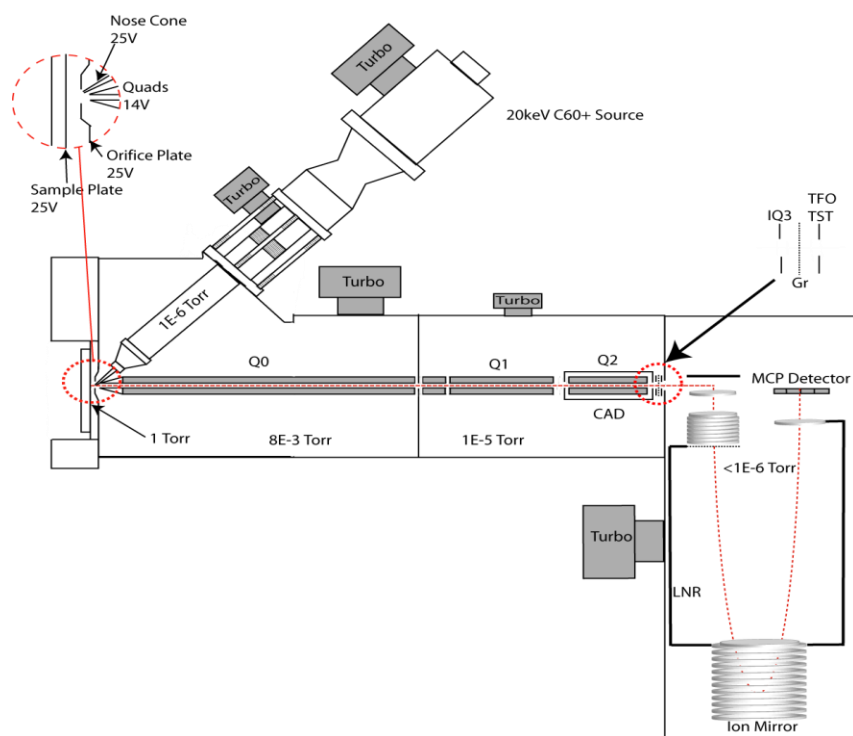


Figure 2.2. An extension block was used to interface the 20 keV C_{60} ion gun and the QSTAR XL mass spectrometer. The insert shows the sample region in detail; the mosquito nose cone protects the ion beam from the high pressure in the sample region.²⁰

Modifications to the commercial instrument were needed in order to interface the ion source. An aluminum extension block was used to mount the C_{60} source to the mass spectrometer. The Q_0 quadrupole was extended (by 10 cm) through the extension block to the sample region. Special consideration was needed to interface the C_{60} ion gun with the instrument's differential pumping system. The ion gun was also modified to protect the source region from the high pressure in the sample region. A mosquito nose cone was used as an aperture and, in the original prototype, defined the beam diameter.

2.3.1. Orthogonal ToF and duty cycles

Orthogonal extraction is responsible for decoupling the secondary ion generation event from the detection scheme; resulting in high mass resolution spectra ($m/\Delta m$ 12000-15600) and flexibility between pulsed and continuous secondary ion generation.²⁰ Unfortunately, the orthogonal orientation results in duty cycle losses. The efficiency or duty cycle for the orthogonal injection of secondary ions into the ToF is calculated using Equation 2.6. In this equation the variable B is $\frac{1}{2}$ the length between the entrance window and the detector and L is length of the ToF entrance window. Since these measurements are 120 mm and 30 mm, respectively for QSTAR instrument, the maximum transmission for a given ion is 25%.

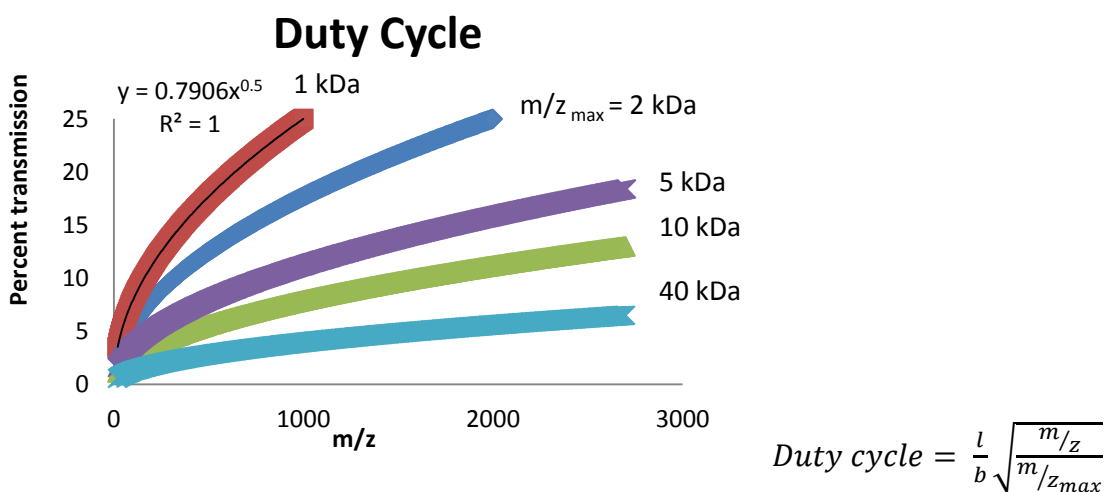


Figure 2.3. The efficiency of the orthogonal injection process is captured in the duty cycle equation. The ion transmission of ions given a m/z maximum of 1 kDa, 2kDa, 5 kDa, 10 kDa and 40 kDa. The wider the mass range, the lower the relative transmission for a given ion. Due to the instrumental dimensions of the QSTAR instrument, the maximum transmission is 25%.

Overall, for a given mass range, the transmission of low mass ions are less efficient than slower high mass ions. The maximum m/z value in the mass range determines the frequency at which the ions are injected; therefore, the larger the mass range, the longer time period between injection pulses, the greater the number of low mass ions are lost. For example, a 1 kDa ion has a higher transmission efficiency (25%) when the mass range maximum is 1 kDa, than when the mass range maximum is 40 kDa (< 5 %).

These duty cycle losses are minor compared to the duty cycle losses associated with pulsed SIMS instruments. For example the duty cycle for operating a pulsed primary ion beam for one second, given a pulsing frequency of 2000 Hz and a 10 ns pulse width, is 2×10^{-5} . The pulse width of the primary ion beam can be increased in order to improve acquisition time and reduce duty cycle losses; however, mass resolution is adversely affected in the process. In the end, the duty cycle losses associated with the orthogonal orientation of the mass spectrometer is significantly less than the duty cycle losses associated with a pulsed ion gun system.

2.3.2. Ion transmission

The ion transmission efficiency of the C_{60} -QSTAR instrument was compared to a coaxial ToF system typically utilized in a commercial SIMS instrument for both inorganic and organic samples. The secondary ion yields for In^+ (m/z 114.9) and gramicidin S (m/z 1141) are 1.5×10^{-3} and 5×10^{-5} secondary ions per C_{60} projectile,

respectively. Compared to a coaxial ToF system, these yields are 10.6x and 3.6x lower for the inorganic and organic samples, respectively. The lower secondary ion yields are caused by duty cycle losses associated with the orthogonal orientation of the instrument. Fortunately due to the versatile functionality of the QSTAR instrument, secondary ion yields can be enhanced by gating and trapping ions in the Q_2 region. This utility enhances the ion yields by a factor of 9 making it equivalent to the coaxial ToF system. The drawback of Q_2 enhancement is its limited mass range, only a 10 Dalton window is accepted. Overall with this function, the sensitivity of the C_{60} -QSTAR instrument is similar to commercial SIMS instruments.

2.3.3. Mass range

As a platform for MALDI and SIMS studies, a versatile mass range capable of detecting high mass ions desorbed with MALDI and low mass ions desorbed with SIMS is necessary. In addition, technical and methodological developments are continuously improving the sensitivity to intact molecules and are extending the mass range utilized with SIMS. Currently only a few systems are capable of producing high mass ions with SIMS, one of these systems, a pressed cesium iodine (CsI) pellet, was used to demonstrate the instrument's dynamic mass range. Three mass spectra of CsI clusters covering different mass ranges are concatenated in Figure 2.4, each spectrum is corrected for variances in primary ion fluence and duty cycle. Overall the instrument is capable of detecting ion from $m/z \sim 100$ to $m/z 40,000$ Daltons. Due to the ability of CsI

to produce cluster ions over a large mass range, it has been used to calibrate the ToF in both the positive and negative ion mode.

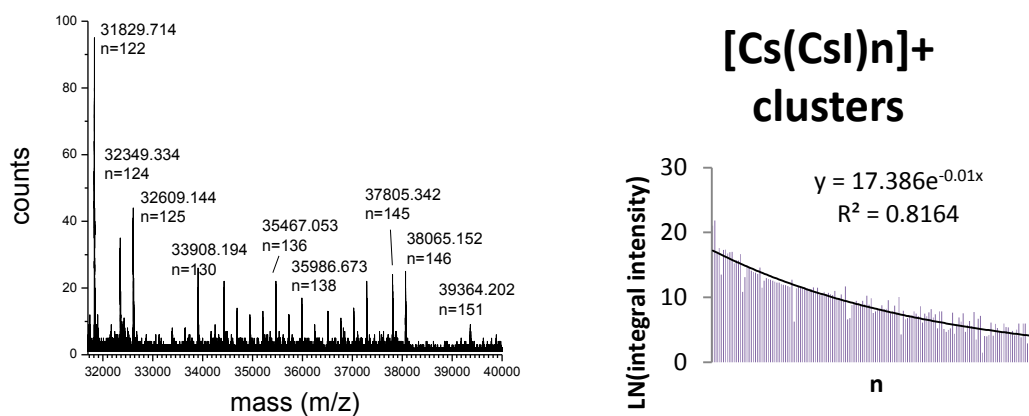


Figure 2.4. ToF-MS spectrum of high mass CsI cluster (left) and bar graph showing the relative intensity of CsI clusters as a function of cluster size (right). A large range of $\text{Cs}(\text{CsI})_n$ clusters were detected from $n=0$ at m/z 132 to $n = 151$ at m/z 39,364.

2.3.4. Tandem MS analyses

One of the most exciting features of this prototype instrument is its tandem MS capabilities. In a product ion scan, the ion of interest is filtered in quadrupole (Q1) and fragmented in the collision cell (Q2). The fragments are subsequently gated into the ToF mass analyzer where they are separated by their mass to charge ratio. Since the desired molecular ion is isolated from reactive secondary ion species before the CID chamber; the resulting tandem MS spectrum is independent of the ionization method. As a result, SIMS-based tandem MS spectra are the same as spectra obtained using ESI and

MALDI ionization methods (see Figure 2.5). This is advantageous to the SIMS community since extensive spectral libraries already exist.

The tandem MS spectra of a lipid, 1,2-dihexadecanoyl-sn-glycero-3-phosphate (PA(16:0/16:0)) obtained using SIMS (left) is similar to the Lipid MAPS lipid library's ESI acquired spectrum (right). The major fragments at m/z 153.0, 255.2, 391.2, and 409.2, correspond to glycerol-phosphate headgroup, the 16:0 Fatty acid, 16:0 LPA-H₂O and 16:0 LPA-H fragments, respectively. The unequivocal identification of the lipid can be made based upon its signature unimolecular fragmentation pattern observed in the tandem MS spectrum.

ToF- MS Spectra of GPA(16:0/16:0) Negative ion mode

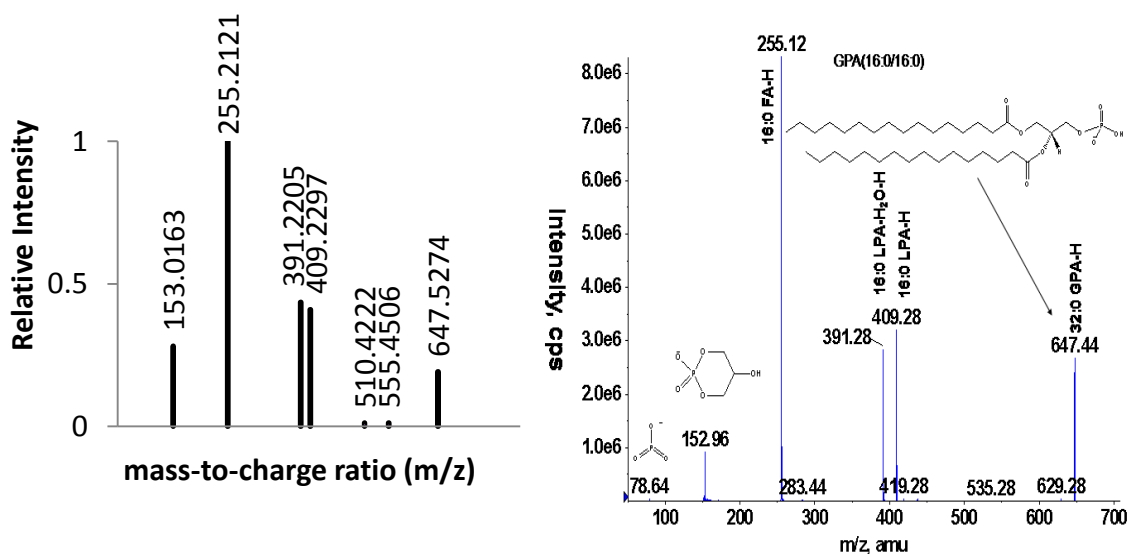


Figure 2.5. The tandem MS spectra of a lipid, 1,2-dihexadecanoyl-sn-glycero-3-phosphate (PA(16:0/16:0)) obtained using C₆₀-QSTAR (left) has the same signature peaks as the ESI-QTRAP acquired spectrum obtained from the Lipid MAPS spectral library (right). (CE= -30 volts)

2.4. SIMS-based Imaging Mass Spectrometry

Focused ion beam systems utilize sophisticated ion optics to focus the ion beam at the sample surface. The focused ion beam, controlled with electrostatic potential, is rastered across the surface of the sample and a mass spectrum is acquired at each pixel. All the ions accumulated in an image acquisition are summed to form a total ion image and a total ion spectra. The mass-to-charge ratio of interest can be selected from the total ion spectra; the resulting image will show only the distribution of that particular ion. Multiple ions can be selected, color coded and overlaid in order to illustrate relative distributions. Conversely, a collection of pixels in the total ion image can be selected to produce a mass spectrum that represents the selected area.

Imaging capabilities in the original prototype were limited due to the inability to focus the beam. In the original prototype, the primary ion beam size was controlled by the diameter of the mosquito nose cone, available in three diameters 100 μm , 50 μm and 10 μm . To change from a high fluence ion beam suitable for spectral acquisitions to a small diameter ion beam suitable for high resolution imaging acquisition the instrument had to be vented, nose cones swapped out and then pumped back down. The whole process took 24 hours.

2.4 Improvements

2.4.1 Focusing the ion beam using rastering plates and an SED

Our beam focusing capabilities were restored with the installation of a new 20 keV C_{60}^+ source from Ionoptika and an SED. Rastering plates, removed from the original prototype due to space restrictions, were placed upstream in the ion optics. The new set-up facilitates focusing efforts by allowing us to visualize the beam in real time for quick focusing and optimizing the ion beams profile. With this new equipment we are able to focus the C_{60} beam to 2-3 μm (see Figure 2.6). The new ion gun is also equipped with a Wein filter to eliminate hydrocarbon contamination and allow us to obtain a 40 and 60 keV beam by selecting the 20 keV C_{60}^{++} and 20 keV C_{60}^{+++} ions, respectively. Overall the new ion gun and SED improves lateral resolution and beam quality.

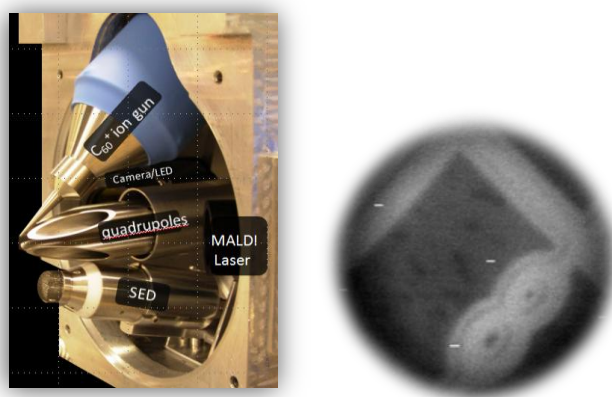


Figure 2.6. The photograph illustrates the orientation of the ion gun, quadrupoles, SED, MALDI laser and camera (left). An SEM image of a grid shows that the 20 keV C_{60}^+ ion source can be focused to 1.6 micron resolution (right).

The high pressure conditions in the sample and Q_0 regions are a potential challenge to high resolution imaging acquisitions. Collisions between the inert nitrogen gas and the primary ion beam can be detrimental to focusing efforts and limit the lateral resolution of SIMS images obtained by the C_{60} -QSTAR instrument. The mean free path, the average distance a molecule travels between collisions, can be calculated using Equation 2.7, where the temperature (T) is 25 °C, d is the molecular diameter of nitrogen (6.2 Å), R is the ideal gas constant and N_A is Avogadro's number. At 5 mtorr the mean free path of the N_2 is 3.6 mm, approximately the distance between the mosquito nose cone and the sample. The SED is used to investigate the effects of collisional cooling and sweeping gas pressure on the focusing abilities of the primary ion beam.

For collisional cooling to be effective, inert gas is injected directly over the sample. Unfortunately, no beam definition is observed when the pressure in the sample region exceeds 5 mtorr (Figure 2.7). Although this design and method is effective for MALDI and ESI ionization techniques, the high pressure injected above the sample is detrimental to the focus of the primary ion beam. As a result, collisional cooling is not compatible with high resolution imaging in the C_{60} -QSTAR instrument.

The sweeping gas allows for ion transmission in the absence of high voltage extraction methods. The C_{60} focusing capabilities were also tested at various Q_0 pressures (Figure 2.7). The SED images show that at operational pressure, the sweeping gas had a minimal effect on the primary ion beams focus.

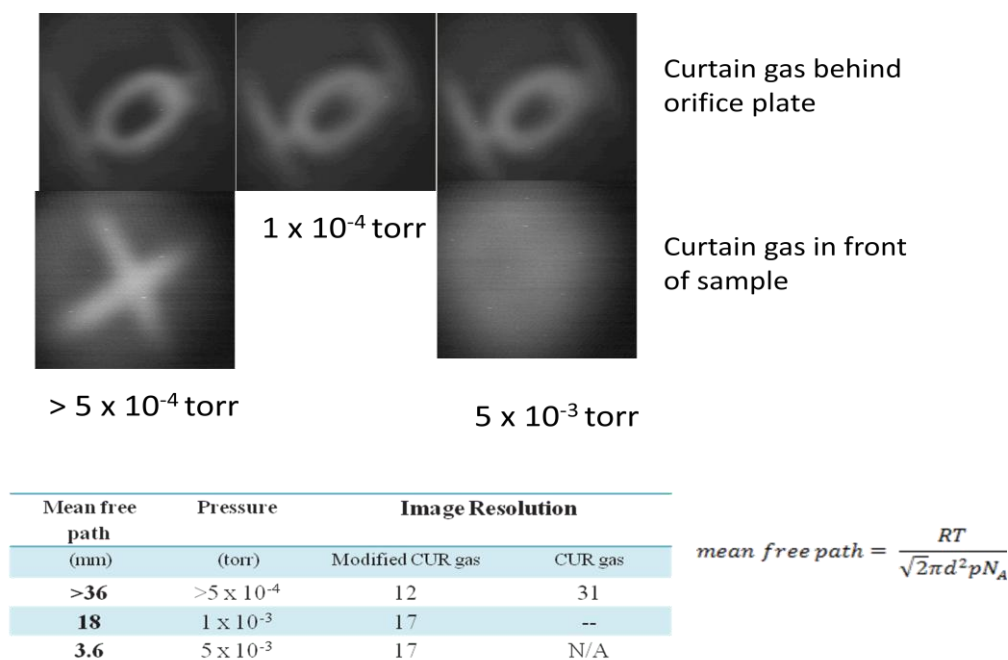


Figure 2.7. SEM images of a grid at 5.0×10^{-4} , 1.0×10^{-4} and 5.0×10^{-3} torr in the Q0 region (top) and the sample region (bottom). Pressures in the sample region needed for collisional cooling is not conducive to ion beam focusing efforts. However, the sweeping gas, injected into the Q₀, had little effect on the ion beam's focus.

2.4.2. Imaging Software Improvements

In an effort to improve imaging acquisition the stage rastering software was updated (oMALDI_{TM} Server 5.1). The new software features a rastering mode that significantly reduces the acquisition time and improves image resolution. In the QSTAR instrument, images are produced by mechanically moving the sample with respect to the stationary ion beam. The upgraded oMALDI server 5.1 is capable of two imaging acquisition modes; spot mode and rastering mode. In the spot mode, the stage is moved in a serpentine pattern and the beam is turned off while the stage moves to the next pixel

(see Figure 2.8, left). Due to the mechanical limitations of the step motors, the minimum spatial resolution in this mode is 10 microns in both the x and y direction. The rastering imaging mode, takes advantage of the instrument dc ion beam compatibility by continually acquiring spectra while the sample stage moves horizontally across the sample (see Figure 2.8, right). The line scans are stacked vertically to produce an image. In this mode the lateral resolution in the y-direction can be as low as 1.5 microns.

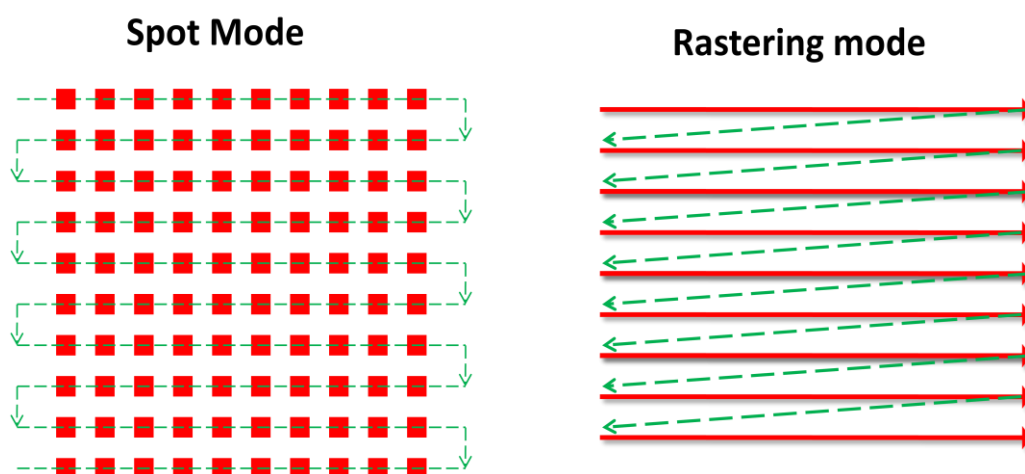


Figure 2.8. Stage rastering patterns available in the upgraded oMALDI server 5.1 software. In the spot mode, the stage is moved in a serpentine pattern and the beam is turned off while the stage is moving to the next pixel. In the rastering mode, line scans acquired by a dc beam are stacked vertically to produce an image. The new imaging pattern improved the instrument lateral resolution and reduced acquisition times by taking advantage of the instrument's dc ion beam capabilities.

There are two advantages of the raster imaging mode; it is capable of 6.4x higher lateral resolution and has faster acquisition times compared to the spot mode imaging acquisitions. The lateral resolution in the x-direction is determined by the minimum stage speed and the flight time of the highest mass in the selected mass range. For a mass range of 60-400 Da, the minimum time per pixel is 54 microseconds. For

example, analyzing a squared millimeter area with a 10 micron resolution in spot mode takes one hour, while the same area analyzed with the rastering imaging mode takes only 12 minutes.

The new rastering scheme is demonstrated in Figure 2.9. In this experiment, a London finder grid dipped in a solution of CsI and air dried was placed on top of a piece of indium foil. The corners of the sample were electrically connected to the sample plate with a drop of melted indium. The image was acquired using the maximum allowed lateral resolution for the O-MALDI stage. As a result the pixels are rectangular, 10 μm in the X-direction and 1.5 μm in the Y-direction. A line scan was taken diagonally across the image using the ionoptika ion imaging software. Based on 16% and 82% of the max height, the lateral resolution of the image is approximately 6.7 microns.

The high resolution imaging technique was also used to image human cheek cells. The cells, approximately 55-60 microns in diameter, were smeared on the surface of an indium tin-oxide (ITO) slide, washed with 10 mM ammonium acetate at 7.4 pH and freeze dried. This experiment shows that cellular imaging is possible with the C₆₀-QSTAR instrument. Although intact lipid species were not observed on the freeze dried cells, alternative sample preparation methods may help to improve the techniques sensitivity at the cellular level.

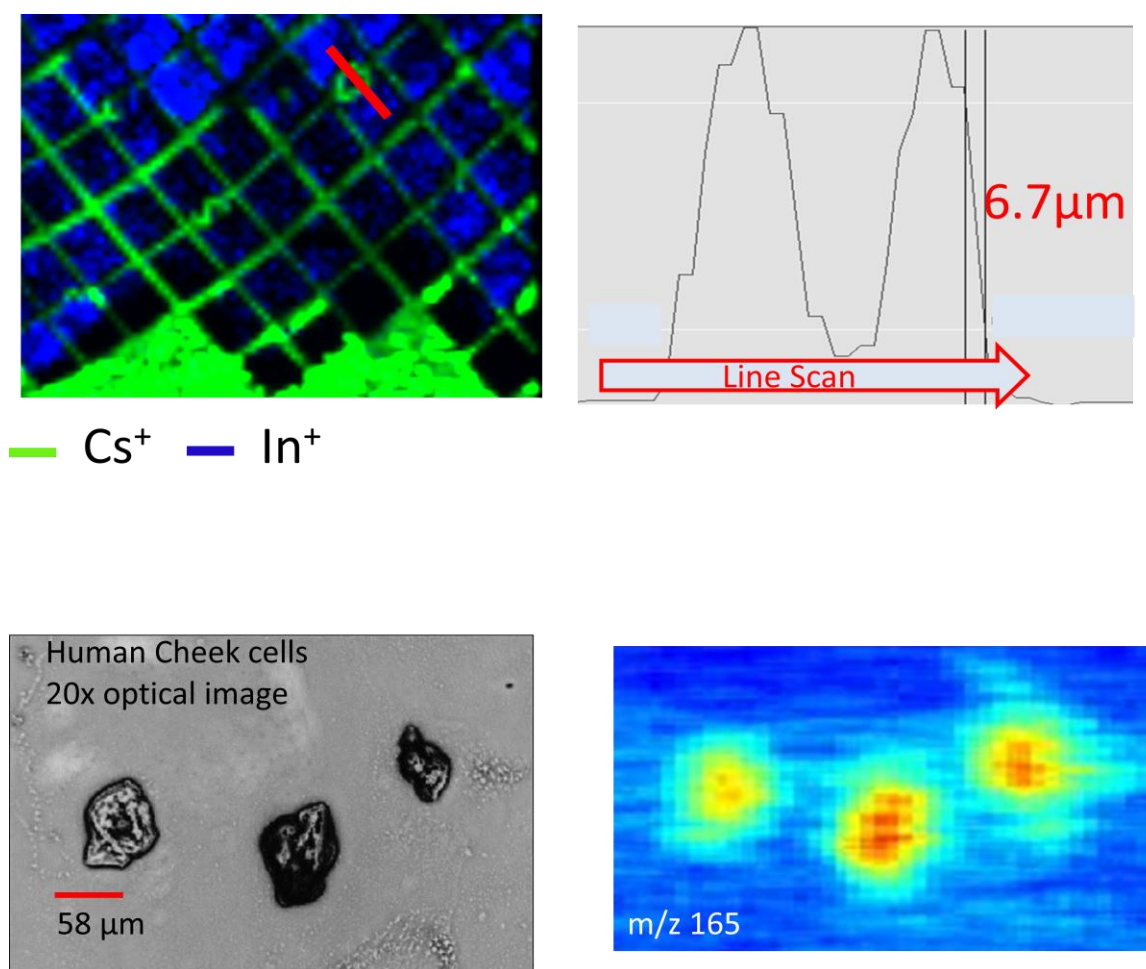


Figure 2.9. The ToF-MS image of 200 mesh finder grid (pitch= bar and square = 127 μm) coated in cesium iodide (green, m/z 132) on a indium foil (blue, m/z 114.9) (top left) had a measured lateral resolution of 6.7 microns (top right). Cellular imaging is feasible at this resolution (bottom). The optical image of the freeze dried cheek cells was obtained under 20x magnification (left). The high resolution ToF-MS image of unknown compound at m/z 165 was localized to the cells (right).

2.5. Conclusions

The union of C_{60} -SIMS and the QSTAR mass spectrometer has produced a multifunctional and powerful bioanalytical instrument. Recent instrumental improvements, including a new C_{60}^+ ion source with a Wein filter and rastering capabilities, a secondary electron/ion detector (SED) and new stage rastering software, enhances performance and expands functionality. The majority of these improvements were aimed at improving imaging capabilities. Although significant progress has been made, the overall lateral resolution is limited by the spatial and temporal accuracy of the sample stage. In order to extract the highest possible lateral resolution capable from a C_{60} source, we must eliminate the stage rastering and rely only on the beam rastering. Not only will this improve the lateral resolution of ToF-MS and tandem MS images, it will also facilitate future depth profiling experiments.

2.6. References

1. Braun, R. M.; Blenkinsopp, P.; Mullock, S. J.; Corlett, C.; Willey, K. F.; Vickerman, J. C.; Winograd, N., Performance characteristics of a chemical imaging time-of-flight mass spectrometer. *Rapid Communications in Mass Spectrometry* **1998**, *12* (18), 1246-+.
2. Garrison, B. J.; Postawa, Z.; Ryan, K. E.; Vickerman, J. C.; Webb, R. P.; Winograd, N., Internal Energy of Molecules Ejected Due to Energetic C-60 Bombardment. *Analytical Chemistry* **2009**, *81* (6), 2260-2267.
3. Russo, M. F.; Szakal, C.; Kozole, J.; Winograd, N.; Garrison, B. J., Sputtering yields for C-60 and Au-3 bombardment of water ice as a function of incident kinetic energy. *Analytical Chemistry* **2007**, *79* (12), 4493-4498.
4. Kotter, F.; Benninghoven, A., Secondary ion emission from polymer surfaces under Ar⁺, Xe⁺ and SF₅⁺ ion bombardment. *Applied Surface Science* **1998**, *133* (1-2), 47-57.
5. Smiley, E. J.; Winograd, N.; Garrison, B. J., Effect of cluster size in kiloelectronvolt cluster bombardment of solid benzene. *Analytical Chemistry* **2007**, *79* (2), 494-499.
6. Kozole, J.; Willingham, D.; Winograd, N., The effect of incident angle on the C-60(+) bombardment of molecular solids. *Applied Surface Science* **2008**, *255* (4), 1068-1070.
7. Kozole, J.; Winograd, N., Controlling energy deposition during the C-60(+) bombardment of silicon: The effect of incident angle geometry. *Applied Surface Science* **2008**, *255* (4), 886-889.
8. Kozole, J.; Wucher, A.; Winograd, N., Energy deposition during molecular depth profiling experiments with cluster ion beams. *Analytical Chemistry* **2008**, *80* (14), 5293-5301.
9. Lu, C. Y.; Wucher, A.; Winograd, N., Molecular Depth Profiling of Buried Lipid Bilayers Using C-60-Secondary Ion Mass Spectrometry. *Analytical Chemistry* **2011**, *83* (1), 351-358.
10. Ryan, K. E.; Smiley, E. J.; Winograd, N.; Garrison, B. J., Angle of incidence effects in a molecular solid. *Applied Surface Science* **2008**, *255* (4), 844-846.
11. Piwowar, A. M.; Fletcher, J. S.; Kordys, J.; Lockyer, N. P.; Winograd, N.; Vickerman, J. C., Effects of Cryogenic Sample Analysis on Molecular Depth Profiles with TOF-Secondary Ion Mass Spectrometry. *Analytical Chemistry* **2010**, *82* (19), 8291-8299.
12. Zheng, L. L.; Wucher, A.; Winograd, N., Chemically alternating Langmuir-Blodgett thin films as a model for molecular depth profiling by mass spectrometry. *Journal of the American Society for Mass Spectrometry* **2008**, *19* (1), 96-102.
13. Vickerman, J. C., *Surface Analysis - The Principal Techniques*. John Wiley & Sons: Chichester, 1997.
14. Postawa, Z.; Czerwinski, B.; Szewczyk, M.; Smiley, E. J.; Winograd, N.; Garrison, B. J., Microscopic insights into the sputtering of Ag{111} induced by C-60 and Ga bombardment. *Journal of Physical Chemistry B* **2004**, *108* (23), 7831-7838.

15. Postawa, Z.; Czerwinski, B.; Winograd, N.; Garrison, B. J., Microscopic insights into the sputtering of thin organic films on Ag{111} induced by C-60 and Ga bombardment. *Journal of Physical Chemistry B* **2005**, *109* (24), 11973-11979.
16. Chernushevich, I. V.; Thomson, B. A., Collisional cooling of large ions in electrospray mass spectrometry. *Analytical Chemistry* **2004**, *76* (6), 1754-1760.
17. Loboda, A. V.; Ackloo, S.; Chernushevich, I. V., A high-performance matrix-assisted laser desorption/ionization orthogonal time-of-flight mass spectrometer with collisional cooling. *Rapid Communications in Mass Spectrometry* **2003**, *17* (22), 2508-2516.
18. Loboda, A. V.; Chernushevich, I. V., Investigation of the mechanism of matrix adduct formation in MALDI at elevated pressure. *International Journal of Mass Spectrometry* **2005**, *240* (2), 101-105.
19. Carado, A. J. New instrumental developments in cluster ToF-SIMS. The Pennsylvania State University, University Park 2010.
20. Carado, A.; Passarelli, M. K.; Kozole, J.; Wingate, J. E.; Winograd, N.; Loboda, A. V., C-60 Secondary Ion Mass Spectrometry with a Hybrid-Quadrupole Orthogonal Time-of-Flight Mass Spectrometer. *Analytical Chemistry* **2008**, *80* (21), 7921-7929.

Chapter 3

In Situ Identification of Glycerophospholipids with the C₆₀-QSTAR Instrument

Abstract:

In this chapter, lipid species from the major sub-classes of glycerophospholipids are characterized using tandem MS. Reference spectra were obtained for protonated, de-protonated and sodiated adducted dipalmitoyl-lipids of each glycerophospholipid sub-class. Common and unique fragments are identified and fragmentation trends are examined. The ability to use *in situ* tandem MS analyses to make an unequivocal identification without using extraction, derivatization or chromatographic methods is also evaluated. Findings indicate that negative ion mode analysis provides valuable structural information about the chemical composition of the fatty acid moieties, allowing for the unequivocal identification of the lipid species. However, without the use of the derivatization method, GPCho lipids are not observed in the negative ion mode. Here the use of salt adducts to assist in the unequivocal identification of GPCho lipids during tandem MS analysis is described. These methods are then used to evaluate the GPCho species in a complex lipid mixture. In addition, the use of tandem MS in conjunction with SIMS imaging to separate isobaric lipids spectrally and spatially is demonstrated.

3.1. Introduction

Biological samples are composed of a complex mixture of lipids. Using a ToF-MS detection scheme, these mixtures can be simultaneously detected in a single mass spectrum. However, due to the redundancy of various structural components among lipid species, certain spectral regions are typically congested. In many cases more than one lipid species can be detected in a single mass channel. This spectral interference hinders identification efforts. Alternative *in situ*-compatible strategies, such as tandem MS, are needed to separate isobaric lipids spectrally based on their fragmentation patterns. In addition, if the isobaric lipids are spatially anti-localized within the sample, imaging-based tandem MS can be used to differentiate them both spectrally and spatially.

The basic composition of glycerophospholipids is illustrated in Figure 3.1. Structural diversity within the class stems from an assortment of headgroups and fatty acid chains attached to a glycerol backbone. The headgroup, typically attached to the *sn*-3 site of the glycerol molecule, consists of a phosphate attached to a choline, serine, ethanolamine, glycerol, hydroxy or inositol functional group. The *sn*-1 and *sn*-2 glycerol sites are attached to fatty acid functional groups. There are three types of fatty acid-glycerol linkages: 1-2-diacyl, 1-alkyl-2-acyl and 1-alk-1-enyl-2-acyl. These linkages are described as diacyl, ether and plasmalogen lipids, respectively. Variations within the fatty acid moieties also contribute to the diverse nature of lipids. The length of the fatty acid chain, the degree of unsaturation and the double bond location are all variable constituents of the fatty acid functional group. Taken as a whole, variability in the

headgroup, fatty acid composition and fatty acid-glycerol linkage can produce a diverse compilation of lipids.

Throughout this thesis, each glycerophospholipid will be referred to by its systematic/common name, denoting the headgroup followed by the number of carbon atoms and double bonds in sn-1 and sn-2 fatty acyl moiety. For instance, 1-palmitoyl,2-oleyl glycerophosphocholine is referred to as GPCho(18:1/16:0). When the length, the degree of saturation, or the stereochemistry of the individual fatty acid continuants are unknown, the overall carbon and double bond counts are summed together, such as GPCho(34:1). This denotation represents a variety of different molecules all having the same molecular weight. In the majority of the cases, the location of the double bond is also not determined; however, it is typically found at the ninth carbon ($\Delta 9$) in mono-saturated lipids.

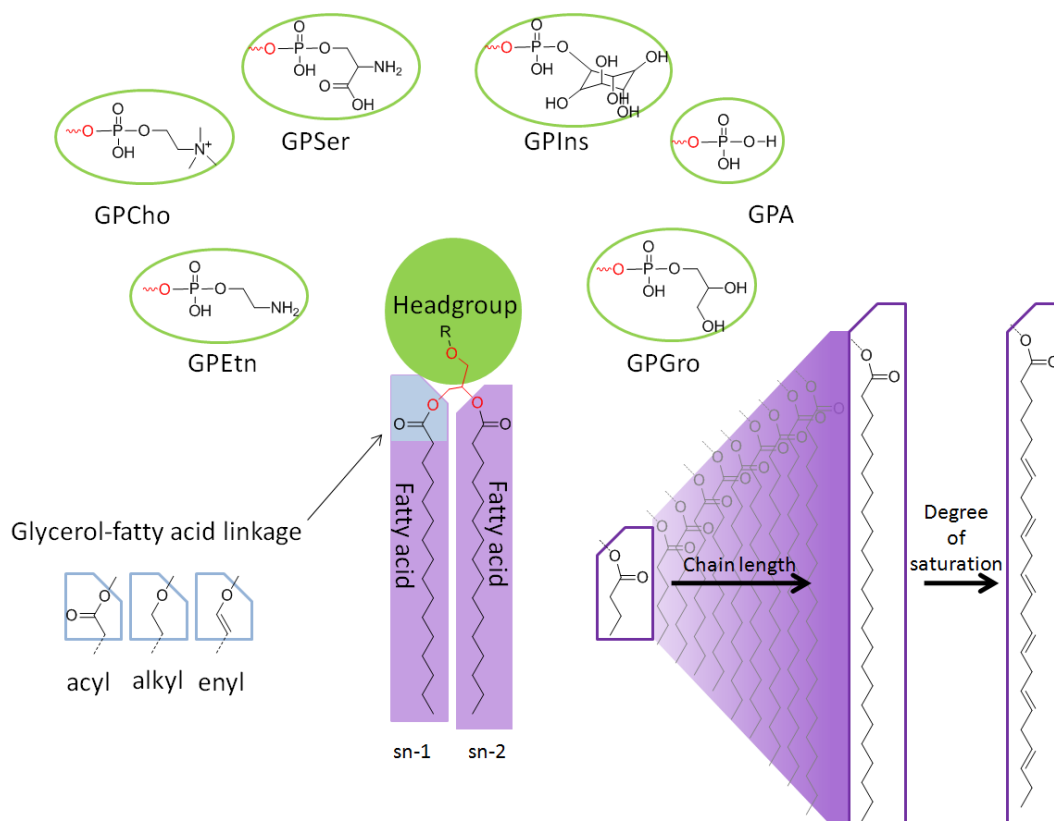


Figure 3.1. The diagram illustrates the basic composition of glycerophospholipids. Three major structural components include the headgroup (green), glycerol-fatty acid linkage (blue) and fatty acid composition (purple). The fatty acid moiety can vary in chain length, as well as in the number and location of double bonds.

As an IMS methodology, SIMS has the ability to extract spectral and spatial information simultaneously, which allows visualization of lipid distributions on the surface of biological samples. The proper identification of lipid molecules is crucial for lipidomics-based research. However, imaging acquisition must be performed *in situ*, which prevents the use of the derivatization and chromatographic methods typically employed within ESI methodology to identify and quantify the lipid content of the sample. As a result, SIMS researchers frequently make assignments based on mass accuracy and on previous knowledge of the sample's biochemistry. This method of

identification often results in erroneous assignments and misrepresents the lipid composition of the sample, due to the congested and convoluted spectra typically observed in these samples. Moreover, the existing method is not sustainable as researchers continue to probe deeper into increasingly complex and unknown biological systems. In this chapter, strategies are developed that will provide unequivocal identifications of lipids *in situ* without the assistance of either the derivatization or the chromatographic separation techniques.

In previous ToF-SIMS investigations, sensitivity issues prevented the detection of intact lipid molecular ions; as a result, signature fragment ions were often used to represent a whole class of lipids. The ToF-SIMS reference spectra for the dipalmitoyl-species of each subclass of glycerophospholipids and characteristic ToF-SIMS-based fragment peaks have been previously reported (see Figure 3.2).¹ It is important to note that in the analysis of a complex mixture of lipids, each fragment ion represents a collection of molecules and not a specific molecular species, since several individual lipids contribute to the fragment ion's intensity. Now, with the use of more sophisticated cluster sources and a mass spectrometer, higher quality reference spectra can be obtained.

Table 1. Characteristic SIMS Fragment Peaks for Various Lipid Classes

lipid	fragment	calculated mass (m/z)
phosphatidylcholine	$C_5H_{12}N^+$	86.0970
phosphatidylcholine	$C_5H_{15}NPO_4^+$	184.0739
phosphatidylcholine	$C_8H_{19}NPO_4^+$	224.1052
phosphatidylethanolamine	$C_2H_7NPO_3^+$	124.0164
phosphatidylethanolamine	$C_2H_9NPO_4^+$	142.0269
phosphatidylethanolamine	$C_2H_5NPO_3^-$	122.0007
phosphatidylethanolamine	$C_2H_7NPO_4^-$	140.0113
phosphatidylglycerol	$C_3H_9PO_6Na^+$	195.0035
phosphatidylglycerol	$C_3H_9PO_6^-$	171.0059
phosphatidylinositol	$C_6H_{10}PO_8^-$	241.0114
phosphatidylinositol	$C_6H_{12}PO_9^-$	259.0219
phosphatidylinositol	$C_9H_{16}PO_9^-$	299.0533
phosphatidylserine	$C_3H_8NPO_6Na^+$	207.9988
cholesterol	$C_{27}H_{45}^+$	369.3521
cholesterol	$C_{27}H_{45}O^+$	385.3470
sulfatide	$C_6H_9SO_8Na^+$	263.9916

Figure 3.2. Characteristic SIMS Fragment Peaks for Various Lipids.¹

Unfortunately, characteristic ToF-SIMS-based fragments cannot be used to assist in the identification of intact species. When examining a known single component film in ToF-MS mode, the fragment peaks can easily be reconciled to the parent ion. However, for spectra obtained from complex lipid mixtures or directly off biological samples, the fragment peaks cannot be reconciled with the original parent ions. For these samples tandem MS analyses is beneficial. Since the parent ion is isolated from the lipid population before it is fragmented a direct association between the fragment ion and parent ion can be made. Throughout this chapter, tandem MS reference spectrums for the same dipalmitoyl-glycerophospholipid standards are obtained. In addition, characteristic tandem MS-related fragment peaks are used to identify lipids in a complex mixture.

Tandem MS analysis has been used to identify lipids for decades; however, this analysis mode has largely been coupled with FAB² and ESI³ ionization

techniques. Even though tandem MS is essential for the analysis of complex biological systems such as lipids, to date this function has not been available in commercial SIMS instruments. The C₆₀-QSTAR instrument is one of the first SIMS instruments with this functionality. Having this capability, SIMS-based lipidomics analysis can utilize some of the techniques and protocols established by shotgun lipidomics^{4, 5} and LC-MS lipidomics.^{6, 7}

The C₆₀-QSTAR instrument has two tandem MS modes: product ion scanning and precursor ion scanning. In a product ion scan, the parent ions are filtered in the Q₁ region and fragmented in the Q₂ region. The resulting fragments are separated and detected in the ToF region. A precursor ion scan is used to identify all the species in a complex mixture that produce a common fragment ion. In this mode, the detector is set to identify only the selected fragment of interest, and the quadrupoles are used to scan the parent ion mass range. Mass hopping based on the mass detection of the parent species reduces acquisition time by eliminating measurements between mass peaks.

Tandem MS spectra are obtained via collision activated dissociation (CAD) or collision induced dissociation (CID). In each case, the ion of interest is activated or excited through collisions with an inert gas. During the collision process, the ion kinetic energy is converted to internal energy. Excess internal energy causes the ion to undergo a series of competitive unimolecular decomposition reactions. These reactions produce characteristic fragment ions that can reveal information about the structure of the ion and assist in the identification of the lipid. The degree of activation can be controlled by two discrete parameters: collision energy (CE) and CAD gas pressure. CE is the voltage difference between the entrance and exit of the collision cell.

As shown in the following equation, increasing the CE accelerates the ion's velocity, increasing its kinetic energy.

$$qV = KE = \frac{1}{2} mv^2 \quad \text{Equation 3.1}$$

Alternatively, the degree of activation can be controlled by adjusting the pressure in the reaction region. At high CAD values, the mean free path is reduced and the number of collisions is greatly increased.

3.2. Experimental

3.2.1. Materials

The following standard lipids, along with Porcine brain lipid extract, were obtained from Avanti and used without further purification:

- 1,2-dihexadecanoyl-sn-glycero-3-phosphate (DPPA, GPA(16:0/16:0));
- 1,2-dihexadecanoyl-sn-glycero-3-phosphocholine (DPPC, GPCho(16:0/16:0));
- 1,2-dihexadecanoyl-sn-glycero-3-phosphoethanolamine (DPPE, GPEthn(16:0/16:0));
- 1,2-dihexadecanoyl-sn-glycero-3-phosphoserine (DPPS, GPSer(16:0/16:0));
- 1,2-dihexadecanoyl-sn-glycero-3-phosphoglycerol (DPPG, GPGro(16:0/16:0));
and
- 1,2-dihexadecanoyl-sn-glycero-3-phosphoinositol (DPPI, GPIIns(16:0/16:0)).

Each lipid standard was dissolved in a 2:1 solution of chloroform to methanol to produce 2 μ M concentration standard solutions. The solutions were spin-coated on a

piranha-etched 5 mm² silicon wafer, or 2 μL of each solution was added to a 2 μL droplet of glycerol.

Isobaric lipid standards 1-hexadecanoyl-2-(9Z,12Z-octadecadienoyl)-sn-glycero-3-phosphoserine PS(16:0/18:2(9Z,12Z)) and 1-hexadecanoyl-2-(6E-octadecenoyl)-sn-glycero-3-phosphocholine PC(16:0/18:1) were obtained from Avanti. Standard lipid solutions (1 mM) were prepared in a 2:1 solution of chloroform to methanol and dry dropped on pre-cut silicon wafers (Ted Pella, Inc).

3.2.2. Instrumentation

The following experiments were performed on the C₆₀-QSTAR mass spectrometer. ToF-MS spectra were taken in both positive and negative ion modes and accumulated for 30 seconds. For tandem MS analysis, the molecular ion was selected with unit resolution, the CAD gas was 3 x 10⁻⁵ torr and the collision energy was ±30 V. For both positive and negative ion modes, the ToF was calibrated using a CsI pellet. For ToF-MS mode spectra, the quadrupole radiofrequencies were weighted to improve the transmission of high mass ions. Imaging acquisitions were acquired by moving the stage in 50 micron increments while accumulating spectral data for one second per pixel.

3.3. Results and discussion

3.3.1. Identification

3.3.1.1. Standard lipids spectra: positive tandem MS

In the positive mode, the protonated lipids species in all five lipid classes decompose in a similar manner (see Table 3.1). They all experience the neutral loss of the headgroup in the *sn*-3 position to produce a diacylglyceride-like ion, which for the dipalmitoyl species is at m/z 551. The exception to this rule is GPCho, the decomposition of which produces a charged headgroup fragment, m/z 184. Precursor ion scanning for m/z 184 can be used to isolate the GPCho from the rest of the glycerophospholipid classes (see Figure 3.3). This method is not effective for isolating other individual lipid classes since all four classes have a common precursor ion. However, in the positive mode, neutral loss scanning tandem MS (a method typically employed in commercial triple quadrupole instruments) can be used to differentiate lipids in the GPEtn, GPSer, GPGro, GPA and GPIIns classes. More specifically, neutral loss scanning of 141, 185, 98 and 260 Da can be used to isolate GPEtn, GPSer, GPA and GPIIns classes, respectively. The mechanisms for the fragmentation of GPA,⁸ GPEtn,⁹ GPGro,¹⁰ GPCho,¹¹ GPSer,^{12,13} and GPIIns¹⁴ have been proposed by Turk and Hsu.

Table 3.1. Characteristic fragment peaks of lipid species from the major sub-classes of glycerophospholipids, GPA, GPCho, GPEthn, GPSer, GPGro and GPIIns obtained using positive ion mode tandem MS. All of the lipids with the expectation of GPCho experience the neutral loss of the headgroup moiety.

	GPCho	GPA	GPEthn	GPGro	GPSer	GPIIns
$[M+H]^+$	734	649	692	723	736	811
$[M+H-98]^+$		551				
$[M+H-142]^+$			551			
$[M+H-173]^+$				551		
$[M+H-185]^+$					551	
$[M+H-260]^+$						551
Headgroup	184					

A critical issue with the tandem MS of protonated lipid species is the lack of structural information about the composition of the fatty acid functional groups. The fragment ion produced in the neutral loss of the headgroup divulges the total number of carbons and the number of double bonds. However, one is unable to determine how they are split between the two fatty acid moieties. For example, the fragment at m/z 551 reveals that the lipid was saturated and contained 32 carbons. Without additional structural information, one cannot unequivocally identify the lipid species.

GPCho content in a complex mixture of lipids, precursor ion scan of m/z 184

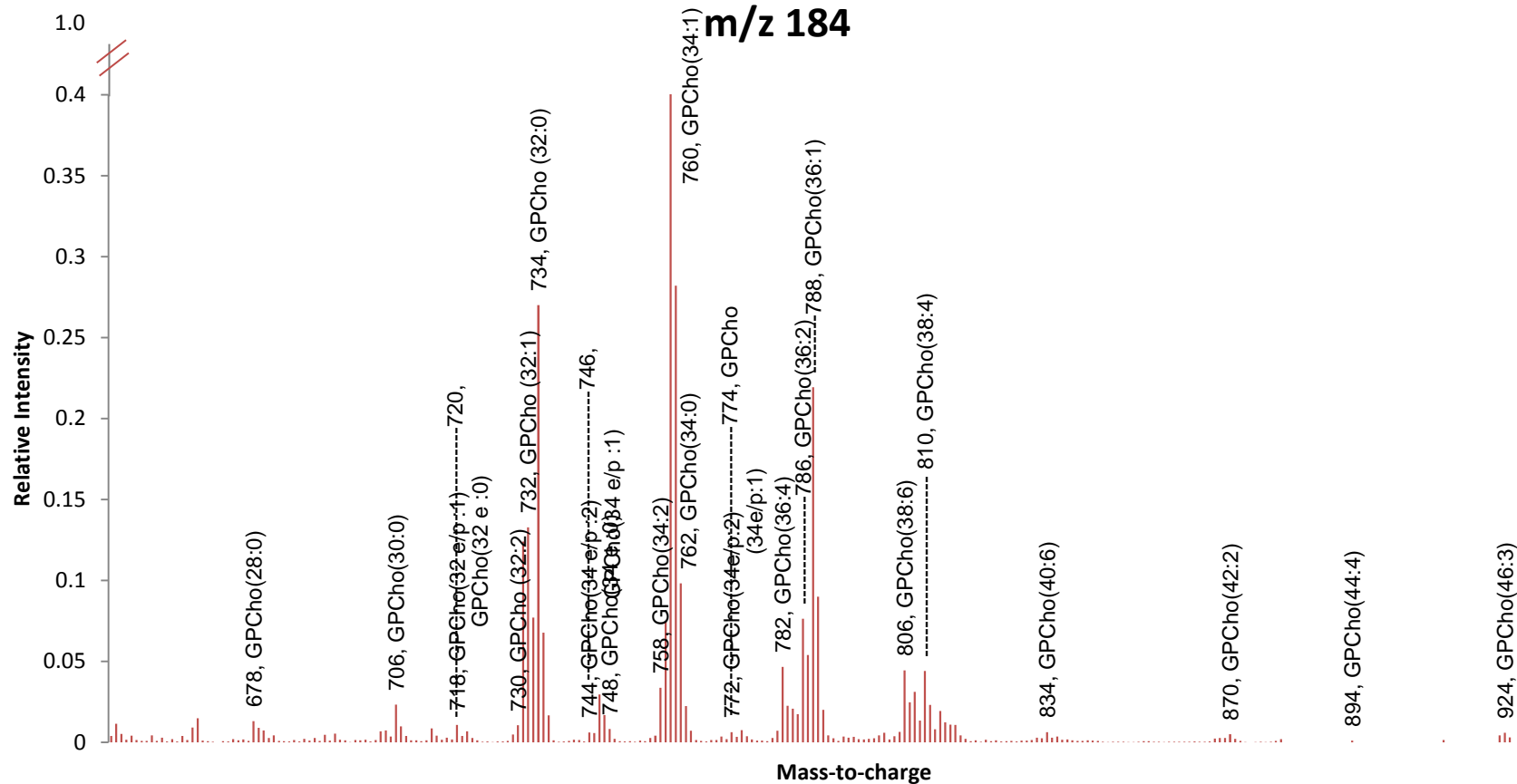


Figure 3.3. Precursor ion scan of the phosphocholine headgroup, m/z 184, isolates the glycerophosphocholine species from other species in complex lipid mixture.

3.3.1.2. Standard lipids spectra: negative tandem MS

For a majority of the glycerophospholipid species, negative ion mode tandem MS analysis can provide crucial structural information and allow for unequivocal identification. The negative ion mode provides valuable structural information about the fatty acid portion of the lipid. Lipid fragmentation patterns obtained in the negative ion mode for the five dipalmitoyl lipids standards are summarized in Table 3.2. For all the lipids, the loss of a fatty acid functional group in the *sn*-1 and *sn*-2 position results in the formation of lyso-fragment $[M-R_1CO_2]^-$ and $[M-R_2CO_2]^-$. For dipalmitoyl-lipids, the neutral loss of the 16:0 fatty acid group in the *sn*-1 position results in fragment m/z 409, 479, 452, 483 and 571 for GPA, GPCho, GPEthn, GPGro and GPIIns lipids, respectively. Similarly, the loss of the 16:0 fatty acid group in the *sn*-2 position results in fragment 391, 461, 434, 465 and 553 for GPA, GPCho, GPEthn, GPGro and GPIIns. All of the lipids have fragment ions at m/z 255.2, representing the fatty acid group $[R_xCO_2]$, with the exception of GPCho. In addition, GPA, GPGro, GPSer and GPIIns are a common fragment at m/z 152.9, representing the glycerol phosphate group. GPEthn and GPIIns are the only lipid species with unique headgroup fragments, at m/z 195.8 and 242.1 respectively.

In the decomposition of GPSer in the negative ion mode, the deprotonated lipid loses its headgroup (m/z 87) to produce a GPA lipid. This molecule proceeds to decay via the same pathway and produces the same fragments as GPA. *In situ* quantification of GPA may be affected if the GPSer molecules are fragmented during the ionization process. Unfortunately a low ion yield in the negative ion mode reduces the

sensitivity of the technique. In addition, charging-related issues with insulating samples are more sensitive in the negative ion mode and cannot be easily corrected with charge compensating devices.

Table 3.2. Characteristic fragment peaks of lipid species from the major sub-classes of glycerophospholipids (GPA, GPCho, GPEthn, GPSer, GPGro and GPIIns) obtained using negative ion mode tandem MS.

	GPA	GPCho	GPEthn	GPGro	GPSer	GPIIns
[M-H] ⁻	647		690	721	734	809
[M-CH ₃ -H] ⁻		717				
[M-87] ⁻					647	
[M-93] ⁻	554		597			
[M-238] ⁻	409	479	452	483		571
[M-256] ⁻	391	461	434	465		553
LPA	409	409			409	409
LPA-H ₂ O	391	391			391	391
16:0 FA	255.2	255.2	255.2	255.2	255.2	255.2
glycerol phosphate	152.9			152.9	152.9	152.9
Headgroup			195.8			241.1

3.3.1.3. Standard lipids spectra: salt adducts tandem MS

The presence of biological salts is a major challenge associated with *in situ* mass spectrometric analyses. Sodium and potassium adducted lipid species are commonly observed in the lipid profiles of biological samples. Although salt is responsible for ion yield suppression and complicates quantification efforts, these adducts are beneficial for identification purposes. The lack of information about fatty acid composition in the positive ion mode and low glycerophosphocholine sensitivity in the

negative ion mode makes *in situ* lipid identification difficult. However, tandem MS spectra of sodiated and potassiated lipid adducts can provide information on fatty acid composition in the positive ion mode. The alkali metal adduct changes the fragmentation dynamics in a way that provides structural information not observable in the tandem MS spectra of a protonated molecular ion.

Currently, tandem MS spectra for sodiated and potassiated adducted glycerophosphocholine are missing from the spectral library of the Lipid MAPS website, www.lipidmaps.org. The addition of these spectra would be beneficial for performing *in situ* analyses.

The tandem MS reference spectrum of sodiated adducted GPCho, GPSer, GPGro and GPA lipids were obtained and the peaks are identified in Table 3.3. The tandem MS spectra for GPSer, GPGro and GPA provide the same structural information on the lipids structure as the tandem MS spectra of the protonated molecular ion. Although the addition of sodium allows for the detection of the headgroup (which otherwise produces an undetected neutral fragment), no additional information is obtained by examining the alkali-adducted lipid species for these classes of lipids. However, this is not the case for the GPCho standard. We are able to obtain enough structural information from the alkali-adducted GPCho tandem MS spectra to make an unequivocal identification.

Table 3.3. Characteristic fragment peaks of sodiated adducted lipid species from the major sub-classes of glycerophospholipids (GPCho, GPSer, GPGro and GPA) obtained using positive ion mode tandem MS.

	GPCho	GPSer	GPGro	GPA
$[M + Na]^+$	756	758	745	671
$[M + Na - TMA]^+$	697			
$[M + Na - 87]^+$		671		
$[M - \text{headgroup}]^+$	573	573		573
$[M - Na - \text{headgroup}]^+$	551	551	551	551
$[M - Na - TMA - R_2CO_2H]^+$	441			
$[M - Na - R_2CO_2H]^+$	500			
Headgroup	184, 146	207	194.9, 60	

The positive ion mode tandem MS spectrum of an alkali adducted phosphocholine is capable of providing enough structural information to correctly identify the lipid species. These scans can also provide steric information that would allow for the differentiation of stereoisomers. For a lipid with uneven fatty acid moieties, the *sn*-1 or *sn*-2 position of each fatty acid branch can be determined by the relative intensity of its respective peaks in the tandem MS spectrum.

From a complex mixture of lipids, a lipid species at m/z 782.5 was selected for tandem MS analyses (see Figure 3.4). This spectrum shows the unimolecular decomposition typical of alkali adducted phosphocholines. As expected, these glycerophosphocholines frequently decompose losing the adducted tri-methylamine, producing a high mass fragment $[M + \text{cation} - N(CH_3)_3]^+$ associated with the loss of a trimethylamine (TMA) species. Also, the peak at m/z 577.5, $[M + H - C_5H_{14}NO_4P]^+$ indicates that the fatty acid chain contains 34 carbons and one double bond, and that m/z 599.5 is the corresponding sodiated-adduct. The fatty acid-related fragment, R_xCO ,

reveals the number of carbons and degree of saturation for each fatty acid moiety. However, the relative abundance of the two R_xCO peaks reveals their position on the lipid molecule. Due to fragmentation dynamics, the fatty acid in the R_1 position is more likely to dissociate than the fatty acid in the R_2 position, producing a higher abundance peak. In the case of the sodiated GPCho(34:1), the 18:1 fatty acid peak has a relatively higher intensity than the 16:0 fatty acid peak. With this information it is possible to unequivocally determine the lipids as GPCho(18:1/16:0). The results obtained in this experiment are similar to the spectra obtained when applying the lithium derivatization method used in shotgun lipidomics to promote intra source decay.^{11, 15}

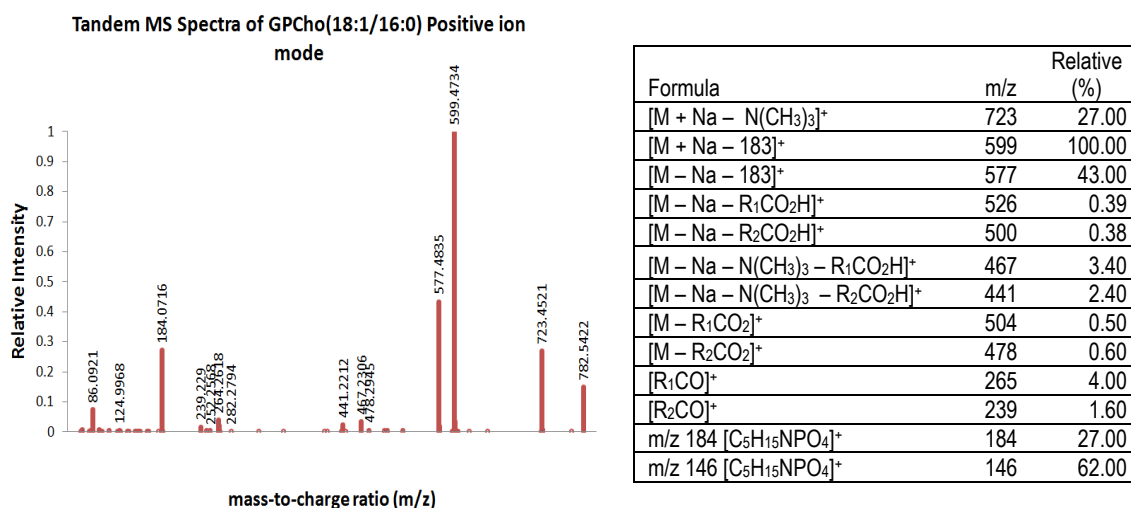


Figure 3.4. Tandem MS spectrum of sodiated lipid adduct GPCho (16:0/16:0) $[M]$ in the positive ion mode. The spectrum provides information about the headgroup (m/z 184 and 86) and fatty acid constituent (m/z 577.5 and 599.5). The spectra also reveals a high-mass fragment associated with the loss of tri-methylamine $[M + alkali\ metal - TMA]^+$.

3.3.1.4. Thin Film Analysis

One useful strategy for separating isobaric lipids *in situ* is the use of tandem MS imaging. The ability to differentiate these lipids spectrally and spatially is demonstrated using thin films of isobaric lipids placed adjacent to each other (see Figure 3.5). Two isobaric lipids were selected—GPSer(16:0/18:2) and GPCho(16:0/18:1)—for which the protonated molecular ions are detected at m/z 760.558 and 760.512, respectively. The resolving power needed to distinguish the two lipids in a ToF-MS spectrum is above 16,500. The imaging can be used to separate the lipids based on their unique fragments. The GPSer(16:0/18:2) lipid produces a fragment at 575.5 (green), after the neutral loss of the phosphoserine headgroup $[M-185]^+$. Conversely, the GPCho(16:0/18:1) produces a fragment at m/z 184 (blue), corresponding to the phosphocholine headgroup. The tandem MS image shows the different spatial distribution of the two isobaric lipids—a feature that is not revealed in the ToF-MS image.

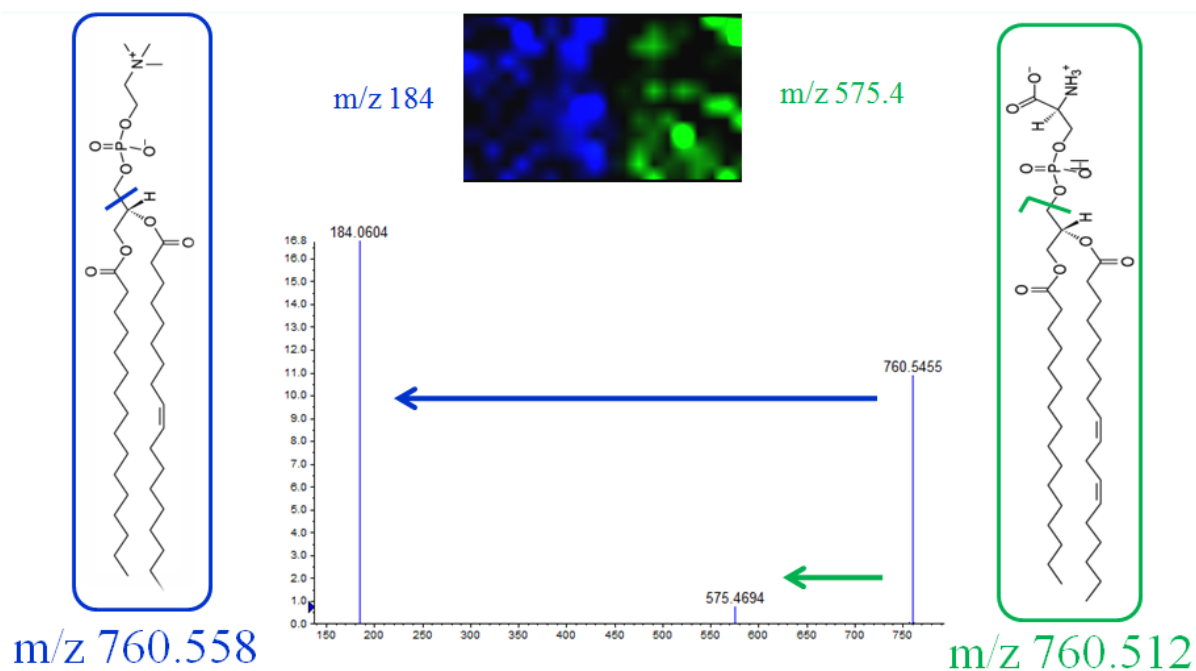


Figure 3.5. Structure, image and tandem MS spectra of PS(16:0/18:2) and PC(16:0/18:1) films. In the tandem MS spectra of m/z 760.5, the unique fragmentation characteristics of glycerophosphoserine (m/z 575.5) and glycerophosphocholine (m/z 184) allowed for the separation of the isobaric lipids. The overlaid image of fragment m/z 575.5 (green) and m/z 184 (blue) shows the spatial separation of the two isobaric lipids.

3.3.2. Ion Abundance and Quantification

Once the lipid species is identified, the next major hurdle is quantifying it. A variety of factors contribute to ion signal intensity. Equation 3.2 attempts to elucidate the complex relationship between molecular ion signal intensity and concentration.

$$I_{m/z} = f([Lipid] \times [ionization\ cross\ section] \times [local\ environment] \times [ion\ stability] \times instrument\ factors \times \dots) \text{ Equation 3.2}^{16}$$

Hankin and coworkers recently attempted to quantify various lipid species using a MALDI mass spectrometry image.¹⁶ The relationship between intensity and

quantity was ascertained by comparing relative ion intensities and their corresponding concentration, obtained from the LC-MS analysis of lipid extracts. The researchers found that phosphocholine lipid molecules exhibited a strong agreement between quantity and signal intensity. Unfortunately, this agreement does not carry through for other classes of glycerophospholipids such as GPEthn and GPSe.

The discrepancy between the GPEthn molecular ion signal and its actual concentration may be due to the fragile nature of the molecule. GPEthn has the propensity to decompose, losing its phosphoethanolamine headgroup and producing a DAG-like ion in the 550-650 Da range. A ToF-MS spectrum of a GPEthn(16:0/16:0) thin film shows a relatively small molecular ion signal compared the high mass DAG-like fragment ion at m/z 551 (see Appendix). Unfortunately, as seen in the previous section, this high mass ion is not unique to GPEthn lipids. Several lipids contribute to the signal intensity in this region, including endogenous DAG molecules, decomposed glycerophospholipids and decomposed TAGs.

Tandem MS provides a useful platform for evaluating lipid stability. For simplicity, only GPCho and GPEthn are compared here. The protonated-molecular-ion-to-major-fragment ratios for GPCho and GPEthn obtained in product ion mode are plotted as a function of collision energy in Figure 3.5. In addition, in an effort to evaluate the effects of salt adducts on the physical properties of fragmentation, the molecular ion-to-fragment (M/F) ratio for sodiated GPCho was acquired as a function of collision energy and plotted in Figure 3.6.

Lipid Fragmentation dynamics in Tandem MS

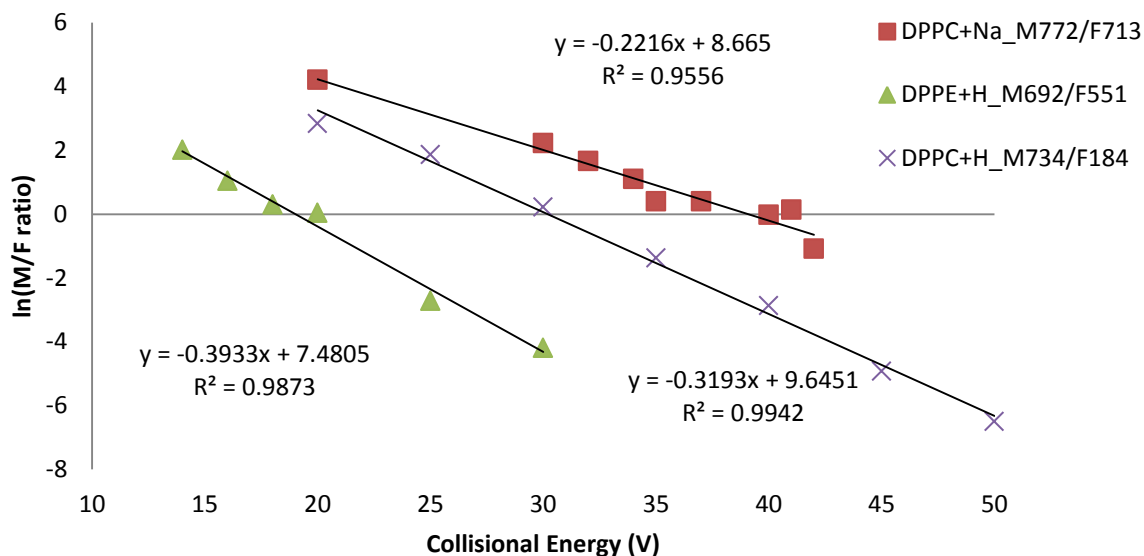


Figure 3.6. Tandem MS spectra were obtained at various collision energies; the variation in integral count of the main fragments— m/z 551 for GPEthn(16:0/16:0), m/z 184 for GPCho(16:0/16:0) and m/z 713 for potassiated GPCho(16:0/16:0)—is plotted.

It is clear from Figure 3.5 that GPCho requires more energy to initiate fragmentation than GPEthn does. In addition, GPEthn has a steeper slope, indicating that the molecule is more sensitive to energy. Based upon this experiment, it also appears that sodium adducts stabilize the lipid species. Sodiated lipids required more energy to initiate fragmentation and are less sensitive to input energy than are the protonated molecular ion species.

$$E_{\text{internal}}^{\text{trans}} = E_{CE} \frac{M_t}{M_i + M_t} \quad \text{Equation 3.3}$$

In an attempt to quantify fragility, the energy at maximum fragment intensity is compared for GPEthn and GPCho. The intensity for GPEthn(16:0/16:0) and GPCho(16:0/16:0) is achieved at 18 and 30 volts of collision energy, respectively.

Based on equation 3.3, the E_{\max} for GPCho(16:0/16:0) and GPEthn(16:0/16:0) is 1.1 eV and 0.7 eV, respectively.

Several factors affect their decomposition, including static hindrance and vibrational modes. GPEthn is structurally similar to GPCho, except that GPEthn exhibits a smaller, less sterically hindered headgroup. This may play a key role in the lower activation energy needed to dissociate the headgroup of a GPEthn lipid. In addition, GPCho lipids are heavier than GPEthn lipids, allowing for more vibrational modes to absorb relatively more energy before thermally decomposing.

3.4. Conclusions

In this chapter, we demonstrate the ability of C_{60} -QSTAR to analyze lipids with ToF-MS, tandem MS, and imaging acquisitions. Although the presence of biological salts hampers quantification efforts, the salts themselves may be employed to elucidate valuable structural information in the positive ion mode that allows for the unequivocal identification of the lipid species. This chapter also examined some of the factors that impede *in situ* quantification. In addition, C_{60} -QSTAR was shown to be able to separate isobaric lipids by combining imaging and tandem MS capabilities. In conclusion, the C_{60} -QSTAR instrument is recommended as a respectable platform with valuable aspects that will benefit lipid analyses.

3.5. Reference

1. Ostrowski, S. G.; Szakal, C.; Kozole, J.; Roddy, T. P.; Xu, J. Y.; Ewing, A. G.; Winograd, N., Secondary ion MS imaging of lipids in picoliter vials with a buckminsterfullerene ion source. *Analytical Chemistry* **2005**, *77* (19), 6190-6196.
2. Matsubara, T.; Hayashi, A., FAB mass-spectrometry of lipids. *Prog. Lipid. Res.* **1991**, *30* (4), 301-322.
3. Milne, S.; Ivanova, P.; Forrester, J.; Brown, H. A., Lipidomics: An analysis of cellular lipids by ESI-MS. *Methods* **2006**, *39* (2), 92-103.
4. Han, X. L.; Gross, R. W., Shotgun lipidomics: Electrospray ionization mass spectrometric analysis and quantitation of cellular lipidomes directly from crude extracts of biological samples. *Mass Spectrom. Rev.* **2005**, *24* (3), 367-412.
5. Han, X. L.; Gross, R. W., Shotgun lipidomics: multidimensional MS analysis of cellular lipidomes. *Expert Review of Proteomics* **2005**, *2* (2), 253-264.
6. Merrill, A. H.; Sullards, M. C.; Allegood, J. C.; Kelly, S.; Wang, E., Sphingolipidomics: High-throughput, structure-specific, and quantitative analysis of sphingolipids by liquid chromatography tandem mass spectrometry. *Methods* **2005**, *36* (2), 207-224.
7. Houjou, T.; Yamatani, K.; Imagawa, M.; Shimizu, T.; Taguchi, R., A shotgun tandem mass spectrometric analysis of phospholipids with normal-phase and/or reverse-phase liquid chromatography/electrospray ionization mass spectrometry. *Rapid Communications in Mass Spectrometry* **2005**, *19* (5), 654-666.
8. Hsu, F. F.; Turk, J., Charge-driven fragmentation processes in diacyl glycerophosphatidic acids upon low-energy collisional activation. A mechanistic proposal. *Journal of the American Society for Mass Spectrometry* **2000**, *11* (9), 797-803.
9. Hsu, F. F.; Turk, J., Charge-remote and charge-driven fragmentation processes in diacyl glycerophosphoethanolamine upon low-energy collisional activation: A mechanistic proposal. *Journal of the American Society for Mass Spectrometry* **2000**, *11* (10), 892-899.
10. Hsu, F. F.; Turk, J., Studies on phosphatidylglycerol with triple quadrupole tandem mass spectrometry with electrospray ionization: Fragmentation processes and structural characterization. *Journal of the American Society for Mass Spectrometry* **2001**, *12* (9), 1036-1043.
11. Hsu, F. F.; Turk, J., Electrospray ionization/tandem quadrupole mass spectrometric studies on phosphatidylcholines: The fragmentation processes. *Journal of the American Society for Mass Spectrometry* **2003**, *14* (4), 352-363.
12. Hsu, F. F.; Turk, J., Studies on phosphatidylserine by tandem quadrupole and multiple stage quadrupole ion-trap mass spectrometry with electrospray ionization: Structural characterization and the fragmentation processes. *Journal of the American Society for Mass Spectrometry* **2005**, *16* (9), 1510-1522.

13. Hsu, F. F.; Turk, J., Studies on phosphatidylserine by tandem quadrupole and multiple stage quadrupole ion-trap mass spectrometry with electrospray ionization: Structural characterization and the fragmentation processes (vol 16, pg 1510, 2005). *Journal of the American Society for Mass Spectrometry* **2006**, *17* (4), 640-640.
14. Hsu, F. F.; Turk, J., Characterization of phosphatidylinositol, phosphatidylinositol-4-phosphate, and phosphatidylinositol-4,5-bisphosphate by electrospray ionization tandem mass spectrometry: A mechanistic study. *Journal of the American Society for Mass Spectrometry* **2000**, *11* (11), 986-999.
15. Hsu, F. F.; Bohrer, A.; Turk, J., Formation of lithiated adducts of glycerophosphocholine lipids facilitates their identification by electrospray ionization tandem mass spectrometry. *Journal of the American Society for Mass Spectrometry* **1998**, *9* (5), 516-526.
16. Hankin, J. A.; Murphy, R. C., Relationship between MALDI IMS Intensity and Measured Quantity of Selected Phospholipids in Rat Brain Sections. *Analytical Chemistry* **2010**, *82* (20), 8476-8484.

Chapter 4

The Characterization of Lipid Directly off the Surface of Tissue with Cluster SIMS Imaging and Tandem MS analyses

Abstract:

In this investigation, the SIMS technique was used to simultaneously acquire chemical and spatial information directly from the surface of a biological tissue section. The molecular-specific secondary ion images reveal the distribution of a variety of lipid species across the surface of the tissue. Tandem MS protocols are used to identify the molecular ion lipid species from the lipid profile of the tissue. The unique chemistry of various anatomical regions in the brain was examined. Due to the complex nature of the sample, principal component analysis (PCA) is used to reduce the dataset and highlight variances in the chemical composition of each anatomical region. SIMS images of the brain tissue shows that cholesterol and galactoceramides species are localized in the white matter regions, glycerophosphocholine and sphingomyelin species are localized to the gray matter regions, and ceramides are localized to the ventricle regions in the tissue.

SIMS was used not only to analyze the chemical profile and distribution of lipids, but also to analyze the efficacy of the MeSIMS technique in the analysis of tissue samples. The presence of the exogenous chemical matrix selectively enhances the signals of galactoceramides and ceramide-lipid species. In addition, the solvent-free

sublimation matrix application protocol (common in MALDI IMS investigations) used to apply the matrix does not degrade the lateral resolution.

4.1 Introduction

Imaging mass spectrometry (IMS) is emerging as a powerful tool in biochemistry for its ability to study chemical processes *in situ*. Matrix-assisted laser desorption ionization (MALDI), desorption electrospray ionization (DESI) and secondary ion mass spectrometry (SIMS)—the three leading IMS techniques—have all proven successful in the analysis of lipids.¹⁻⁴ SIMS is currently the only one capable of achieving micron lateral resolution; this condition has limited the use of MALDI and DESI techniques for single cell investigations. However, to obtain lateral resolution appropriate for tissue investigations, these techniques are often complementary. A coronal rodent brain section is an established tissue model system commonly used for IMS-based lipidomic investigations, and it has been examined previously using DESI^{4, 5} and MALDI⁶⁻⁸ methodologies. In this report, the chemical profile and distribution of lipids derived from this tissue model system is obtained using SIMS.

Although IMS-based lipidomic investigations provide valuable spatial information, they may prevent exogenous separation techniques that can facilitate identification and quantification efforts. Since the proper identification of lipid molecules is crucial in lipidomics-based investigation, a series of tandem MS-related lipid analysis strategies (developed in Chapter 3) were utilized in this study to help

identify various lipid molecules in a standard tissue section. While these strategies are routinely employed in MALDI and DESI investigations to identify lipids *in situ*, this report is the first to use them in a SIMS-based analysis.

One advantage of SIMS is its ability to interrogate native samples without requiring modifications such as labels or the addition of a matrix. However, when sensitivity issues are hampering an investigation, the addition of a matrix has been shown to be beneficial.¹⁶⁻¹⁸ SIMS analysis can be used to study the effects of an exogenous matrix on the lipid profile obtained directly off a tissue section. In addition, SIMS can be used to evaluate the efficacy, uniformity and chemical displacement associated with the matrix application technique.

MeSIMS is a common methodological approach employed to improve *in situ* lipid molecular ion sensitivity. In using this method, an exogenous matrix is applied to the surface of the sample. This matrix facilitates the ionization of the surrounding surface molecules by donating protons. In some cases, the presence of a matrix can lead to the protonation of molecules typically observed as anionic species.⁹

Careful consideration is needed when choosing a matrix and an application method to ensure minimal molecular displacement and aberrant spectral convolution. A variety of MALDI matrices have been used previously to test this technique, however unlike MALDI, MeSIMS is not limited to organic matrices with high absorbance in the UV and IR wavelengths. Ionic liquids¹⁰, vapors¹¹, water^{12, 13} and liquid matrices¹⁴ have also been tested. Nevertheless, MALDI matrices have an added advantage: since they are able to absorb energy efficiently, it is theorized that they can absorb excess energy from the impinging primary ion beam and improve molecular ion

yields by reducing thermal-related fragmentation. In this technique, the nature of the matrix selected is crucial because it influences the quality and chemical signature of the resulting spectra.

Matrix application is also a crucial step in the sample preparation protocol, especially for imaging investigations. A variety of application methods have been developed, including dry-dropping, sieving, spin coating, airbrushing and inkjet printing. A majority of these involve a wet solvent and require a tradeoff between lateral resolution and sensitivity. Recently, Hankin and coworkers developed a solvent-free, sublimation-based matrix application protocol.¹⁵ Due to the low analyte displacement associated with this method, it is well suited for imaging acquisitions and is routinely used in MALDI IMS investigations. In this research work, the lateral resolution and spectral characteristics of the tissue sample are examined before and after the application of a matrix via sublimation.

4.2 Methods/ Procedures

4.2.1. Materials

Alpha-cyano-4-hydroxycinnamic acid (CHCA) was obtained from Sigma-Aldrich. Chemicals obtained from commercial sources were used without further purification efforts. The coronal slices of rat brain tissue were sectioned directly onto an indium tin-oxide slide using a cryostat at $-20\text{ }^{\circ}\text{C}$ and stored in a $-80\text{ }^{\circ}\text{C}$ freezer. To avoid

condensation contamination, the tissue section was acclimated to ambient temperature under vacuum before analysis.

4.2.2. Matrix application

The CHCA matrix was applied to the samples using a sublimation technique describes by Hankin and coworkers.¹⁵ This solvent-free matrix application method produced uniform microcrystalline films on the sample with minimal analyte displacement. Briefly, the sample was attached to a cold finger with thermally conductive tape while 200 mg of matrix was placed on the bottom of the sublimation chamber. A vacuum pump evacuated the sublimation chamber as a heating mantle heated the matrix reservoir to 190 °C for 20 minutes.

4.2.3. Instrumentation

Sample analyses were performed on a QSTAR XL mass spectrometer modified to allow SIMS ionization (described in detail in Chapter 2). The C_{60}^+ ion fluence was 3×10^{-12} ions/cm² for native tissue samples and 2.28×10^{-13} ions/cm² for the matrix-coated tissue. Imaging acquisitions were obtained using the TV raster flyback pattern. The C_{60} primary ion source was operated with a dc beam current mode of 243 ms per 50 μm^2 pixel. Tandem MS experiments were carried out using N₂ collision gas

with a residual gas pressure of 4×10^{-5} torr, 20-60 eV collisional energy, and the mass filter set to unit resolution. MALDI Images were acquired with an N₂ laser at 100 shots per pixel. Data collection and analysis was conducted using Analyst QS 2.0 software and oMALDI Server 5.1 software (Applied Biosystems/MDS Sciex). Further image processing and PCA analysis were performed using BIOMAP software (www.maldi-msi.org) and MATLAB, respectively.

4.3.0 Results and Discussion

4.3.1. High resolution imaging

The flexible imaging capability of the C₆₀-QSTAR instrument allows for both whole tissue analysis and high resolution images to elucidate the finer structures within the tissue. In the SIMS image of the whole tissue, anatomical regions could easily be recognized and their unique chemistry extracted. In Figure 4.1, the chemical distribution of the phosphocholine headgroup at m/z 184 is mapped. The intensity of this signal is abundant enough to provide a high contrast image of the whole tissue section. In the image (Figure 1a), anatomical portions of the brain including the cerebral cortex, the hippocampus, the corpus callosum (cc), the thalamus, the third (V3) and lateral (VL) ventricles as well as the hypothalamus are easily distinguishable. A particular anatomical region can be selected and imaged at a higher spatial resolution. In Figure 1b, the hippocampus region is examined. The individual folds are easily visible in this image,

including the pyramidal layer traversing through the CA1, CA2 and CA3 regions of the hippocampus and the granule layers in the dentate gyrus (DG). The superior lateral resolution associated with SIMS allows for the visualization of anatomical features with micron resolution, as demonstrated in Figure 4.1c. In this SIMS image, the alveus (alv) and corpus callosum (cc) can easily be distinguished from each other based on their chemical composition.

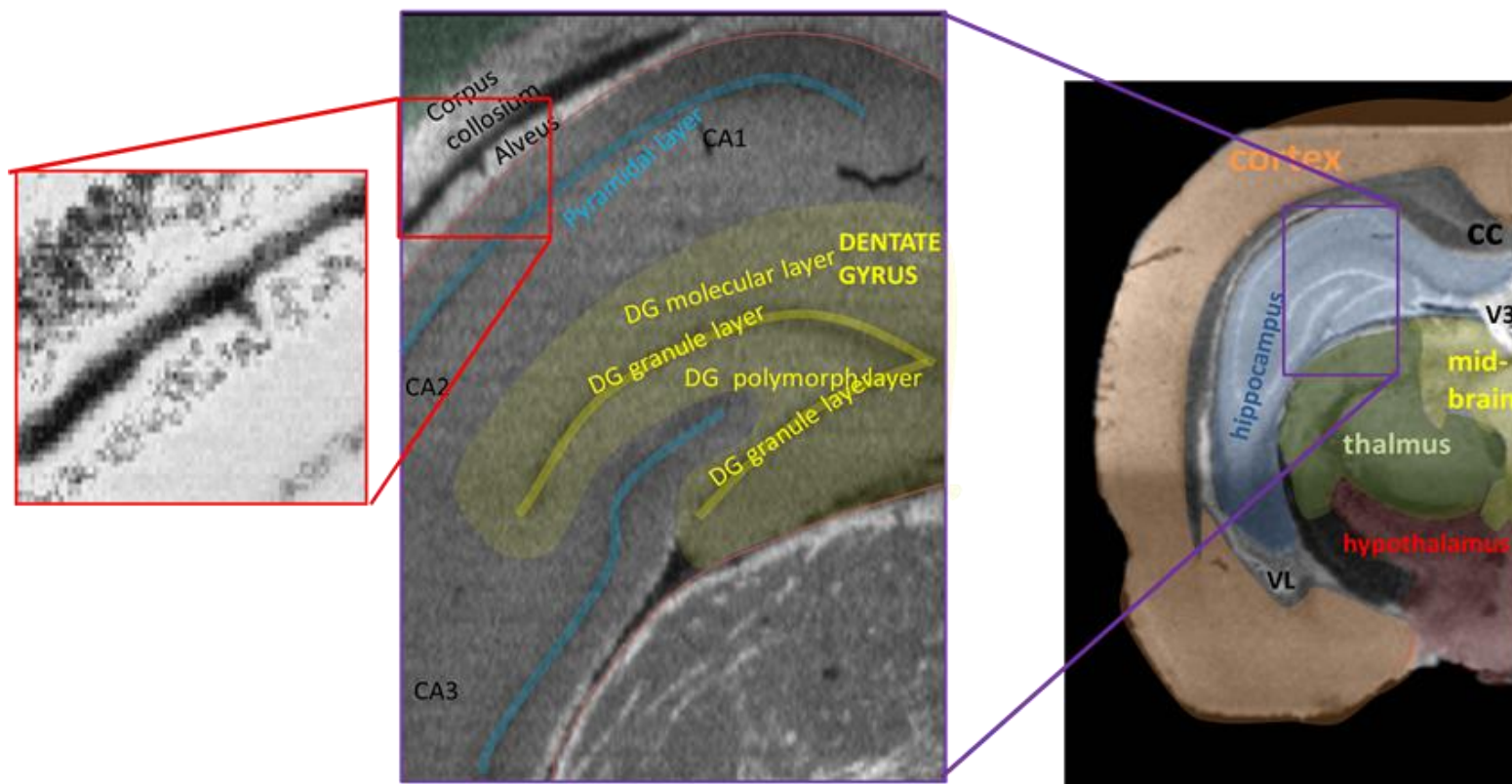


Figure 4.1. ToF-SIMS image of phosphocholine signal at m/z 184 across the surface of a coronal rat brain section. Three images at varying lateral resolutions were obtained; each pixel in the whole tissue images are $50 \mu\text{m}^2$ ($8.2 \times 11.6 \text{ mm}$) (a), the hippocampus region image are $10 \mu\text{m}$ ($4.5 \text{ mm} \times 2 \text{ mm}$) (b) and the pixels in the image of the corpus colosium are $10 \mu\text{m} \times 1.5 \mu\text{m}$ ($500 \mu\text{m} \times 350 \mu\text{m}$) (c).

4.3.2. The Analysis of lipids on tissue using Hybrid QSTAR instrument

In the analysis of the coronal rat brain tissue, a number of intact lipid species were detected using positive ion mode C_{60} -SIMS and MeSIMS (see Table 4.1). The identities of the most intense peaks were confirmed using tandem MS. Due to the high mass resolution and the ToF calibration of the instrument, the calculated mass accuracy for all lipids was less than 50 ppm. Glycerophospholipids and sphingolipids were the major lipid constituents observed *in situ* using positive mode imaging. The sterol lipid cholesterol was also observed. Glycerophosphocholines were the only subclass of glycerophospholipids detected. Conversely, a variety of molecules from three different sub-classes of sphingolipids were detected, including sphingomyelin, galactoceramides and ceramides. Diacylglycerols from the glycerolipids were also detected; however, it is unknown whether the peaks attributed to these lipids were due to the presence of these species in the tissue or to the degradation of intact lipid species from SIMS-based fragmentation.

4.3.3. Lipid distributions

The tissue could be divided into three main chemical environments; white matter, gray matter, and ventricle regions. In general, regions of white matter contained higher intensities of cholesterol and galactoceramides species when compared to regions of gray matter, which contained glycerophosphocholine species. In addition, a number of

ceramides were localized to the ventricle system of the tissue. The lipid profiles of each anatomical region are examined in detail below.

Table 4.1. Lipid species detected from the surface of a coronal tissue section using SIMS.

Sub-class [LM_ID]	Label (C:DB)	Formula	Exp. Mass	Actual mass	Mass acc	Species	Localiz ation
Glycerophospholipids Glycerophosphocholin es/ Diacylglycerophospho holines/ [GP0101]	PC(32:0)	C ₄₀ H ₈₁ NO ₈ P	734.569982	734.5700	0	[M+H] ⁺	gray matter
			756.551927	756.5504	2	[M+Na] ⁺	
			772.525865	772.5074	24	[M+K] ⁺	
			697.478428	697.4684	14	[M+Na-TMA] ⁺	
			713.452366	713.4569	6	[M+K-TMA] ⁺	
	PC(32:1)	C ₄₀ H ₇₉ NO ₈ P	732.554331	732.5804	36	[M+H] ⁺	gray matter
			754.536276	754.5312	7	[M+Na] ⁺	
			770.510215	770.5716	80	[M+K] ⁺	
			695.462778	695.5198	82	[M+Na-TMA] ⁺	
			711.436715	711.4861	69	[M+K-TMA] ⁺	
	PC(34:0)	C ₄₂ H ₈₅ NO ₈ P	762.601282	762.5927	11	[M+H] ⁺	gray matter
			784.583227	784.5633	25	[M+Na] ⁺	
			800.557164	800.5343	29	[M+K] ⁺	
			725.509728	725.5113	2	[M+Na-TMA] ⁺	
			741.483666	741.4675	22	[M+K-TMA] ⁺	
	PC(34:1)	C ₄₂ H ₈₃ NO ₈ P	760.585632	760.5967	15	[M+H] ⁺	gray matter
			782.567577	782.5779	13	[M+Na] ⁺	
			798.541515	798.5425	1	[M+K] ⁺	
			723.494078	723.4839	14	[M+Na-TMA] ⁺	
			739.468016	739.4584	13	[M+K-TMA] ⁺	
PC(36:1)	C ₄₄ H ₈₇ NO ₈ P	788.616932	788.6097	9	[M+H] ⁺	white matter	
		810.598877	810.5846	18	[M+Na] ⁺		
		826.572815	826.5354	45	[M+K] ⁺		
		751.525378	751.5541	38	[M+Na-TMA] ⁺		
		767.499316	767.4899	12	[M+K-TMA] ⁺		
Glycerolipids/ Diradylglycerols/ Diacylglycerols/ [GL0201]	DAG(32:0)	C ₃₅ H ₆₇ O ₄	551.503935	551.5047	1	[M+H-OH] ⁺	gray matter
	DAG(34:0)	C ₃₇ H ₇₁ O ₄	579.535235	579.533	4	[M+H-OH] ⁺	
	DAG(34:1)	C ₃₇ H ₆₉ O ₄	577.519585	577.5125	12	[M+H-OH] ⁺	
	DAG(34:2)	C ₃₇ H ₆₇ O ₄	575.503935	575.4864	30	[M+H-OH] ⁺	

	DAG(34:3)	C ₃₇ H ₆₅ O ₄	573.488285	573.4764	21	[M+H-OH] ⁺	gray matter
	DAG(34:4)	C ₃₇ H ₆₃ O ₄	571.472635	571.5171	78	[M+H-OH] ⁺	
	DAG(36:0)	C ₃₉ H ₇₅ O ₄	607.566534	607.5872	34	[M+H-OH] ⁺	
	DAG(36:1)	C ₃₉ H ₇₃ O ₄	605.550885	605.5461	8	[M+H-OH] ⁺	
	DAG(36:2)	C ₃₉ H ₇₁ O ₄	603.535235	603.5362	2	[M+H-OH] ⁺	
	DAG(36:3)	C ₃₉ H ₆₉ O ₄	601.519585	601.502	29	[M+H-OH] ⁺	
	DAG(36:4)	C ₃₉ H ₆₇ O ₄	599.503935	599.4896	24	[M+H-OH] ⁺	
Sphingolipids/ Phosphosphingolipids Ceramide Phosphocholines (sphingomyelins) [SP0301]	SM(d18:1/1 8:0)	C ₄₁ H ₈₄ N ₂ O ₆ P	731.606701	731.5510	76	[M+H] ⁺	gray matter
			753.588645	753.5796	12	[M+Na] ⁺	
			769.562584	769.5889	34	[M+K] ⁺	
			694.515147	694.5167	2	[M+Na-TMA] ⁺	
			710.489085	710.4917	4	[M+K-TMA] ⁺	
Sphingolipids/ Neutral glycosphingolipids/ Simple Glc series [SP0501]	GalCer (d18:1/22:1)	C ₄₆ H ₈₇ NO ₈	804.632939	804.6155	22	[M+Na] ⁺	White matter
	GalCer (d18:1/22:0)	C ₄₆ H ₈₉ NO ₈	806.648589	806.6425	8	[M+Na] ⁺	
	GalCer (d18:1/22:1(2-OH))	C ₄₆ H ₈₇ NO ₉	820.627854	820.6327	6	[M+Na] ⁺	
	GalCer (d18:1/22:0(2-OH))	C ₄₆ H ₈₉ NO ₉	822.643504	822.6519	10	[M+Na] ⁺	
	GalCer (d18:1/ 24:1(2-OH))	C ₄₈ H ₉₂ NO ₉	826.677209	826.5354	172	[M+Na] ⁺	
	GalCer (18:1/24:1)	C ₄₈ H ₉₂ NO ₈	810.682294	810.5846	121	[M+H] ⁺	
	GalCer (18:1/24:1)	C ₄₈ H ₉₁ NO ₈	832.664239	832.644	24	[M+Na] ⁺	
	GalCer (18:1/24:0)	C ₄₈ H ₉₃ NO ₈	834.679889	834.6452	42	[M+Na] ⁺	
	GalCer (d18:1/24:2 (2-OH))	C ₄₈ H ₈₉ NO ₉	846.643504	846.6849	49	[M+Na] ⁺	
	GalCer (d18:1/ 24:1(2-OH))	C ₄₈ H ₉₁ NO ₉	848.659154	848.6557	4	[M+Na] ⁺	
	GalCer(d18:1/24:0(2-OH)) and GalCer(d18:0/24:1(2-OH))	C ₄₈ H ₉₃ NO ₉	850.674804	850.6871	14	[M+Na] ⁺	
	GalCer (d18:1/26:0)	C ₅₀ H ₉₇ NO ₈	862.711189	862.6831	33	[M+Na] ⁺	
	GalCer (d18:0/26:0)	C ₅₀ H ₉₉ NO ₈	864.726839	864.6648	72	[M+Na] ⁺	
	Sphingolipids/ ceramides/ N-Acylsphingosines (ceramides) [SP0201]	Cer(d18:1/24:0)	C ₄₂ H ₈₂ NO ₂	632.634554	632.5946 ^a	63	
C ₄₂ H ₈₀ NO			614.623989	614.5956 ^a	46	[M-2H ₂ O+H] ⁺	
C ₂₆ H ₅₀ NO			392.389239	392.3772 ^a	31	[M-C ₁₆ H ₃₂ O] ⁺	
Cer(d18:1 /22:0)		C ₄₀ H ₇₈ NO ₂	604.603254	604.57 ^a	55	[M-H ₂ O+H] ⁺	
		C ₄₀ H ₇₆ NO	586.592689	586.5482 ^a	76	[M-2H ₂ O+H] ⁺	
			626.585199	626.5641 ^b	34	[M-H ₂ O+Na] ⁺	
	C ₂₄ H ₄₆ NO	364.357939	364.3484 ^a	26	[M-C ₁₆ H ₃₅ O ₂] ⁺		

Cer(d18:1 /20:0)	C ₃₈ H ₇₄ NO ₂	576.571954	576.556 ^a	28	[M-H ₂ O+H] ⁺		
	C ₃₈ H ₇₂ NO	558.561389	558.5281 ^a	60	[M-2H ₂ O+H] ⁺		
		598.553899	598.5307 ^b	39	[M-H ₂ O+Na] ⁺		
	C ₂₂ H ₄₂ NO	336.326639	336.3211 ^a	16	[M-C ₁₆ H ₃₅ O ₂] ⁺		
Cer(d18:1 /18:0)	C ₃₆ H ₇₀ NO ₂	548.540654	548.5402 ^a	1	[M-H ₂ O+H] ⁺	gray	
	C ₃₆ H ₆₈ NO	530.530089	530.5167 ^a	25	[M-2H ₂ O+H] ⁺		
	C ₂₀ H ₃₈ NO	308.295339	308.3098 ^a	47	[M-C ₁₆ H ₃₅ O ₂] ⁺		
Sterol Lipids/ Cholesterol and derivatives/ [ST0101]	CH	C ₂₇ H ₄₅	369.352125	369.3409	30	[M+H-H ₂ O] ⁺	white
		C ₂₇ H ₄₆ O	386.354865	386.3713	43	[M-H] ⁺	

4.3.4. Lipid chemistry in the white matter

White matter consists of bundles of myelinated neural fibers. These fibers are an essential feature in neural communication because they transduce signals throughout the brain and body. The chemical composition of these regions is important to their proper function. A number of galactoceramides and 2-hydroxylated-galactoceremides were co-localized with cholesterol and distributed in the myelin-rich white matter regions of the brain (see Figure 4.2). Although a number of these molecules have been observed previously in the cerebral white matter using ToF-SIMS analysis, additional galactoceramides were found in this analysis, including GalCer(d18:1/26:0) at m/z 862.68, GalCer(d18:0/26:0) at m/z 864.68, GalCer(d18:0/22:0) at m/z 808.6, and GalCer(d18:1/22:0) at m/z 806.6.

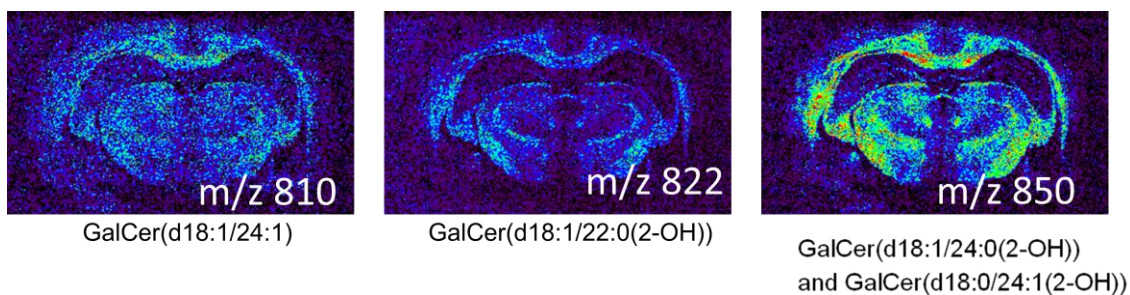
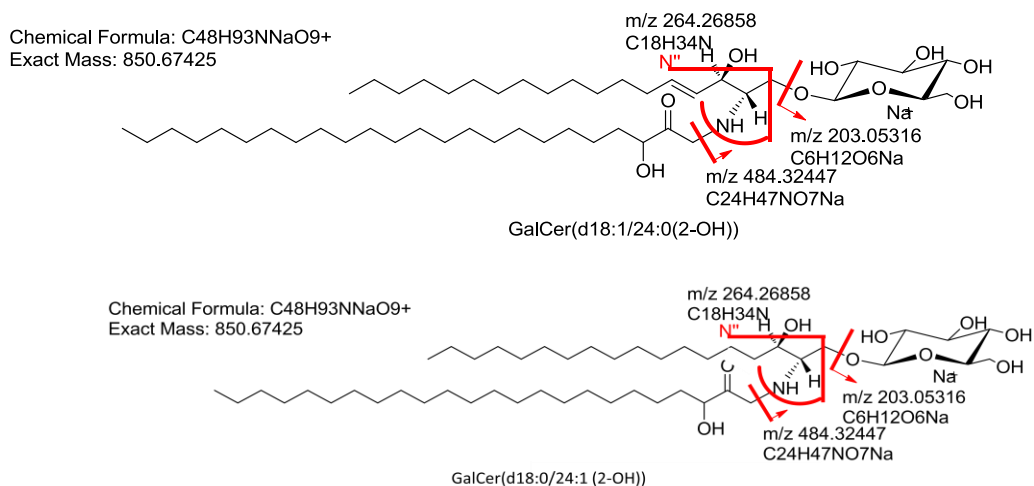


Figure 4.2. MeSIMS images of galactoceramides in the coronal brain tissue.

Nygren and coworkers previously reported finding a handful of sodium cationized galatocerbrosides in the white matter of the cerebellum tissue using SIMS.¹⁹ Six galactoceramides with 4-sphingenine (d18:1) backbones were detected, two of which had 24:0 and 24:1 fatty acid groups at m/z 834.6 and 832.5, and four of which had 2-hydroxy functionalized 22:0, 24:0, 24:1 and 23:0 fatty acid chains at m/z 822.5, 850.6, 848.6, and 836.6, respectively. In this investigation, the identifications were made based on mass accuracy (~6 ppm) of the peak obtained from a ToF-MS spectrum and from prior knowledge of the samples' biochemical properties. However, stereoisomers could not be distinguished in this detection mode due to isobaric interference. For instance, galactoceramides having sphinganine (d18:0) backbones spectrally interferes with those having 4-sphingenine (d18:1) backbones. The contribution of galactoceramides with sphinganine (d18:0) backbones to these peaks has not been addressed in previous investigations. However, in this research, tandem MS analyses performed directly on the surface of the tissue section was used to distinguish these isobaric stereoisomers.



Tandem MS Spectrum of m/z 850.5 (positive ion mode)

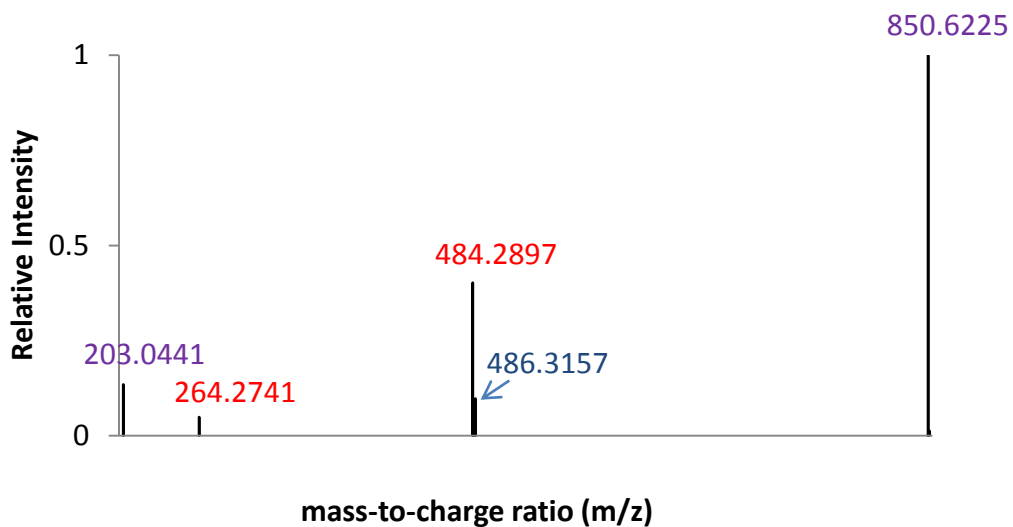


Figure 4.3. The tandem MS spectrum reveals that more than one lipid is detected at m/z 850.5. The peak at m/z 486, which is 2 Da mass units higher than the m/z 484 peak that represent galactoceramides with d18:1 backbone, confirms the presence of

glactocerbrosides with sphinanine (d18:0) backbones. The lipid structures were created using Chemdraw 12.0 software.

Tandem MS was used *in situ* to separate isobaric lipids at m/z 850.5, GalCer(d18:1/24:0(2-OH)) and GalCer(d18:0/24:1(2-OH)) (see Figure 4.3). The tandem MS spectrum of the m/z 850 peak revealed four major fragment ions: m/z 486.3, 484.2, 203.0 and 264.3. The fragment at m/z 203.0 represents the sodiated galactose headgroup, common to both lipids. The fragment at m/z 264.3 represents the 4-sphingenine (d18:1) backbone characteristic of the GalCer(d18:1/24:0(2-OH)) lipid. Fragment peaks m/z 484 and m/z 486 correlate to the neutral loss of the 24:0 and 24:1 fatty acid functional group for GalCer(d18:1/24:0 (2-OH)) and GalCer(d18:0/24:1(2-OH)), respectively. The presence of peaks m/z 484 and m/z 486 indicate that both lipids are, in fact, present in the tissue, and both lipids are contributing to the intensity of the m/z 850 obtained in the ToF-MS spectrum.

Galactoceramides and sulfatides are the most abundant lipids in myelin, representing about 27% of the lipid composition.²⁰ Galactoceramides are not only important structural components in myelin but are also believed to help regulate cell differentiation in neural support cells (oligodendrocytes).²¹ The ability to characterize and determine the distribution of these molecules is important for understanding complex neural functions and dysfunctions resulting from diseases. Therefore, the spatial and chemical information provided by ToF-SIMS imaging of lipids in the brain provides a potential platform for studying neurological diseases.

Galactoceramides are important lipids in the structure and function of myelin. In the absence of these lipids, neural conduction is greatly impaired. In humans, the inability to synthesize Galactoceramides is known as Krabbe disease, a debilitating genetic disorder. Galactoceramides are also building blocks for complex ganglioside lipids, whose aberrant metabolism is responsible for debilitating neurologic diseases such as Tay-Sachs, Sandhoff disease, and Gullain-Barré syndrome.

4.3.5. Lipid chemistry in the gray matter

A number of glycerophosphocholine species were detected in the gray matter regions, the majority of which were adducted to biological salts. Their characteristic high mass fragments associated with the loss of a trimethylamine functional group were also detected. The tandem MS strategies established in Chapter 3 were used to identify the individual lipid species. With this method, sufficient structural information was provided to make unequivocal identification. The glycerophosphocholine content obtained matched that from previously reported ToF-SIMS datasets. One notable observation in this dataset and previously reported datasets is the lack of glycerophosphocholine species with polyunsaturated fatty acid (PUFA) moieties. PUFAs are essential to neural processes such as learning and vision processing. These molecules are stored in glycerophospholipids (e.g., GPCho) and should be present in the tissue, but remain undetected. Currently, the physics governing the SIMS-based ionization of PUFA containing glycerophospholipids is not well understood and further studies are needed to elucidate this matter.

Only one sphingomyelin species was detected in both the gray matter and white matter regions: SM(d18:1/18:0). Although derived from very different biochemical pathways, sphingomyelin and glycerophosphocholine have similar structural components. Sphingomyelin has a ceramide core, consisting of a sphingosine backbone linked to a fatty acid with an amide bond, and a phosphocholine headgroup. As a result, similar fragmentation patterns are observed among sodiated and potassiated adducted sphingomyelin and their glycerophospholipid analogues. It has been proposed that the high ion yields associated with glycerophosphocholine in positive ion mode is due to the species' ability to stabilize the positive charge in the tri-methylamine moiety. However, this does not seem to apply to the sphingomyelin species, since its detection *in situ* has been elusive.

The relative intensity of SM(d18:1/18:0) can be used to evaluate the chemical integrity of the tissue sample. During tissue degradation, sphingomyelin such as SM(d18:1/18:0) was metabolized via sphingomyelinase into its ceramide core, Cer(d18:1/18:0), and phosphocholine. The distribution and relative intensity of the intact SM(d18:1/18:0) and its degraded metabolite Cer(d18:1/18:0) are shown in Figure 4. The SIMS image shows that SM(d18:1/18:0) (the blue portion) had a uniform distribution in both the gray and white matter regions, except for a slight signal depression corresponding to regions with high Cer(18:1/18:0) signals. Signature peaks for Cer(18:1/18:0) at m/z 548.5, m/z 530.5 and m/z 308.2 were localized to the left cerebrum (anatomical direction) and the hippocampus. The high lateral resolution of the image reveals Cer(18:1/18:0) was present in the hippocampus formation but absent in both the

granule layer of the dentate gyrus and the pyramidal layer, where intact SM(d18:1/18:0) molecules were still present.

Cer(d18:1/18:0) is a well-known biomarker for apoptotic cell death and tissue degradation. Recently, Hankin and co-workers identified and chemically mapped Cer(d18:1/18:0) formed as a result of ischemia reperfusion and traumatic brain injury with MALDI-IMS.²² The ability to detect this molecule directly from the surface of a tissue shows that ToF-SIMS imaging is a potential platform for studying more severe brain injuries.

The degradation detected in this tissue sample most likely occurred during the analysis. Although the sample was prepared and stored at cryogenic temperature, the SIMS analysis was performed at room temperature. The long acquisition time and the lack of a cryogenically compatible sample stage were most likely responsible for the degradation. Efforts to improve the acquisition time of SIMS imaging in the C₆₀-QSTAR instrument are discussed in Chapter 2. In addition, the development of the C₆₀-QSTAR cryogenic stage and sample handling protocols that would preserve the integrity of the tissue during analysis is discussed in Chapter 6.

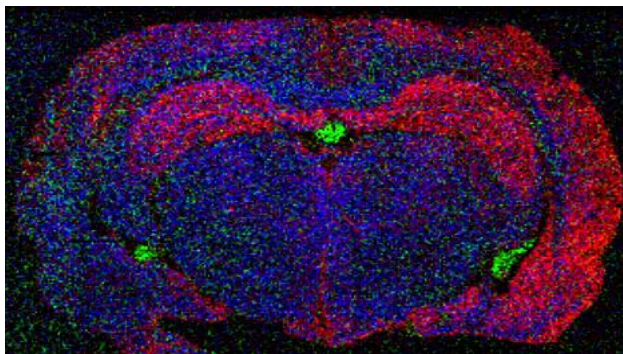


Figure 4.4. MeSIMS image overlaying Cer(18:1/18:0) at m/z 548.5 (red), SM(d18:1/18:0) at m/z 694.5 (blue) and Cer(d18:1/22:0) at m/z 604.4 (green).

4.3.6. Lipid chemistry in the ventricles

Other ceramide species detected in the MeSIMS—including Cer(d18:1/22:0) at m/z 604.4, 586.5 and 364.3, Cer(18:1/20:0) at m/z 576.5, 558.5 and 336.3, and Cer(18:1/24:0) at m/z 632.5, 614.5 and 392.3—were localized to the ventricular system. These signature peaks for ceramides were not visible in the native SIMS image or spectra, although the sodiated-adducts of Cer(d18:1/20:0) and Cer(d18:1/22:0) were detected.

The ventricular system plays a pivotal role in protecting the brain during traumatic brain injuries. The ventricle is filled with cerebrospinal fluid (CSF), which cushions the brain and minimizes the impact of head trauma. The CSF also functions as a circulation system, transporting hormones and metabolites to and from various part of the brain. The exact reason for the accumulation of these degradation products in the ventricle regions is currently unclear. However, this pathway is often used to excrete excess metabolites produced from the surrounding neural tissue.

4.3.7. PCA analysis

Due the complexity of the dataset, the mathematical procedure known as principal component analysis (PCA) was used to simplify the data. In PCA analysis, the data is simplified by extracting spectral and spatial variances. PCA analysis is routinely

coupled to ToF-SIMS datasets.²³⁻²⁵ It is frequently used to distinguish variances in chemistry between health control tissue and disease tissue, with successful applications in obesity²⁶, cancer²⁷ and myocardial infarctions²⁸ studies. In this experiment, PCA was performed on the ToF-SIMS data obtained from imaging the native tissue section before matrix application. The first components focused on the variances between the organic tissue and the inorganic substrate. Eventually, the 5th loading (0.24% variance error), shown in Figure 4.5, was able to successfully separate and compile the unique chemical signatures of the white matter and gray matter.

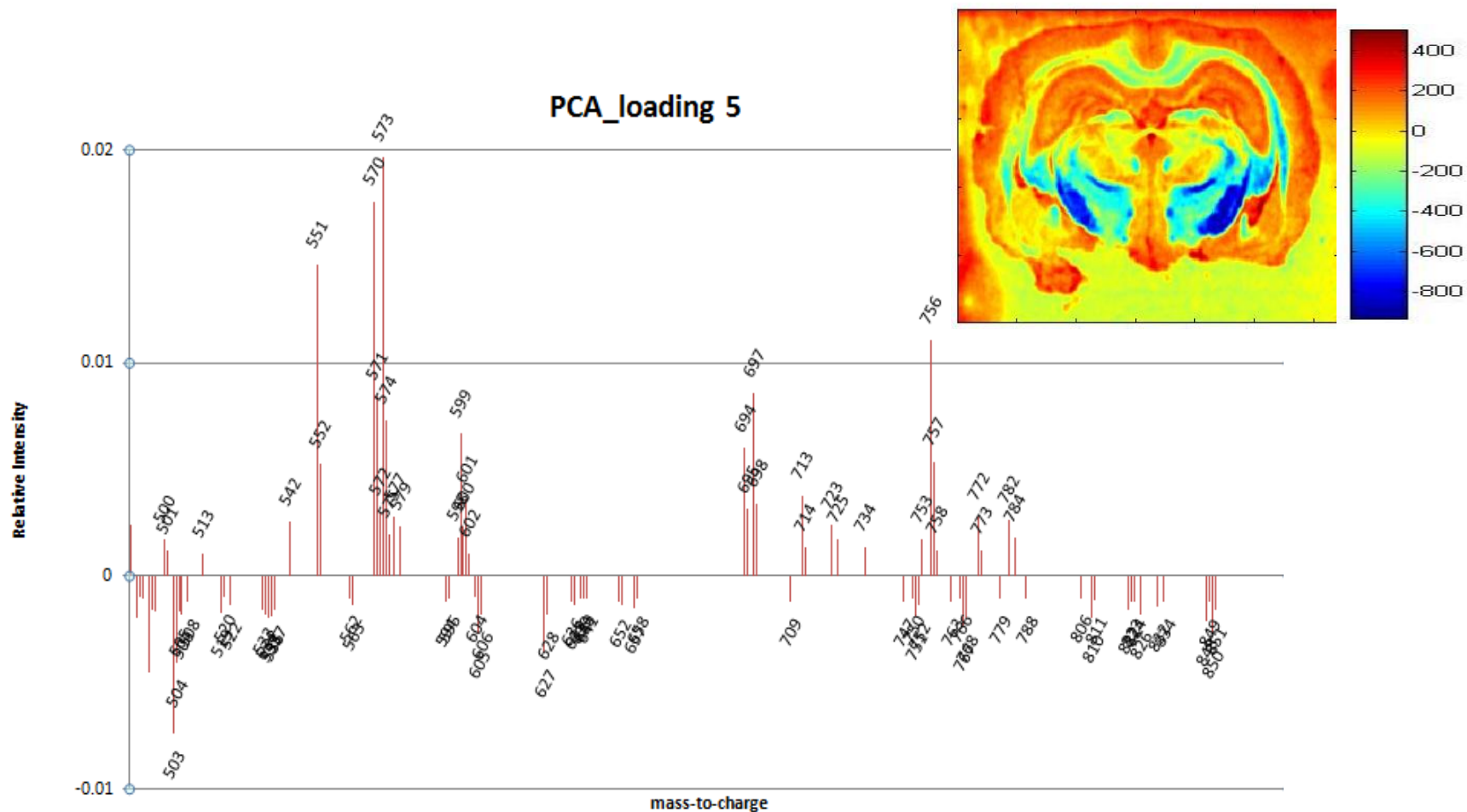


Figure 4.5. Principle component analysis of the lipid region obtained from a native tissue analyzed with ToF-SIMS (Loading 5, 0.24 percent variance). In this analysis, the chemical signature of the gray matter (positive loadings) was separated from the chemical signature of the white matter (negative loadings). In general, the gray matter contained glycerophospholipids related species and the white matter contained galactoceramide related lipid species. For clarity, peaks with relative intensity less than 0.001 in both the positive and negative direction were filtered out.

Site-specific PCA was used to extract the ceramide-related signals from the complex dataset. In the PCA analysis of the entire dataset, some significant features with minute chemical difference were overlooked. This is common when analyzing complex samples. However, when anatomical regions were isolated and PCA analyses were performed on each region, site specific chemical characteristics were extracted from the truncated datasets. When spectral and spatial data from the third ventricle region were isolated and analyzed with PCA, ceramide-related peaks were revealed (see Figure 4.6). This PCA loading was then applied to the entire dataset, revealing similar chemistry in both the right and left lateral ventricles (see Figure 4.4, green portions).

PCA was also used to extract spectral information lost during the image processing procedure. Due to the large file size associated with mass spectrometric images, current data is binned to reduce the image file to a manageable size. During this process, mass resolution is greatly diminished and chemical information is lost. In this case, PCA analysis was able to successfully extract these ceramide-related peaks from the binned dataset. New data processing and data management methods are being developed that will help to overcome this challenge.

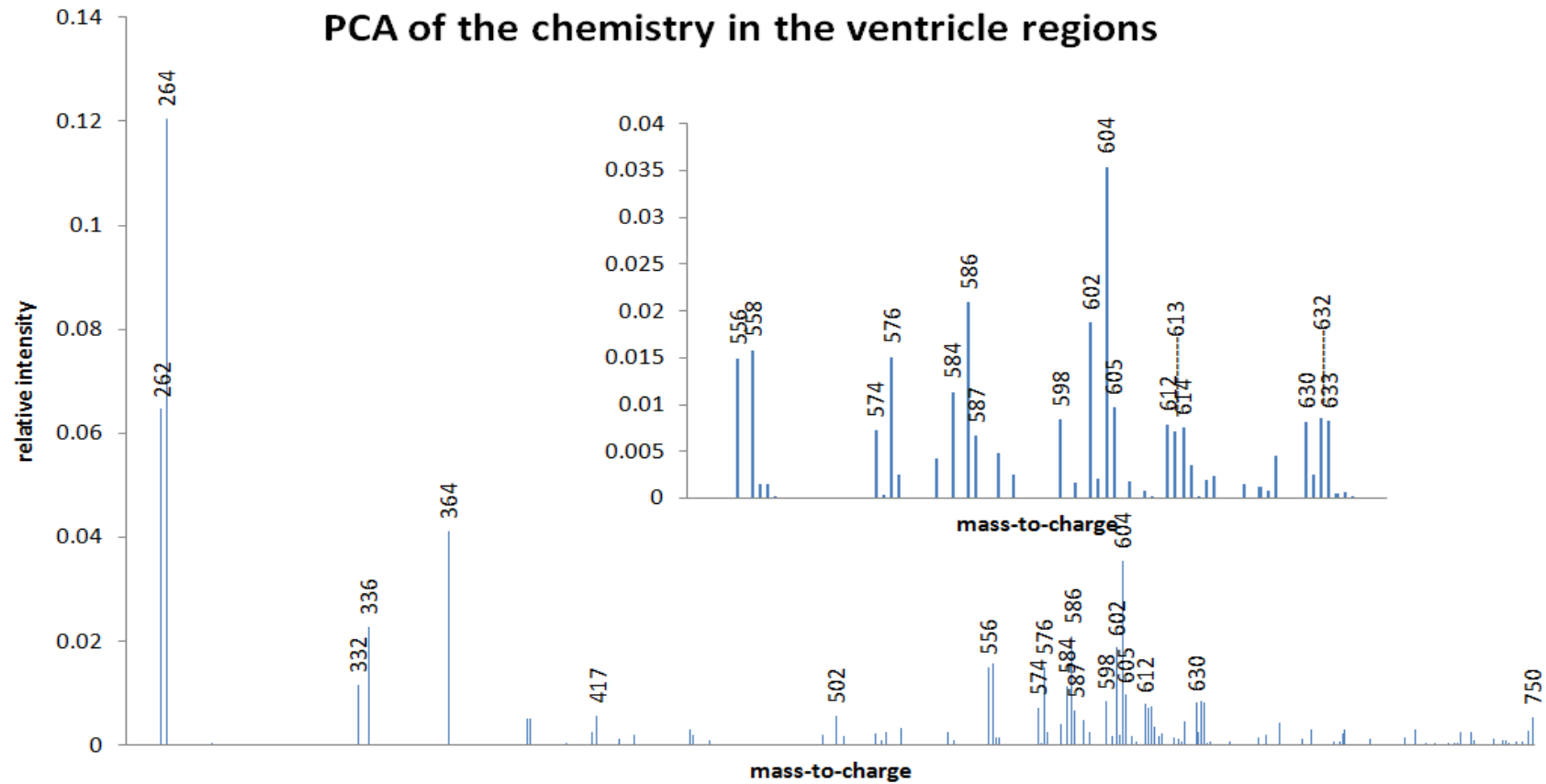


Figure 4.6. Principle component analysis of the isolated third ventricle region obtained from the matrix-coated tissue analyzed withToF-SIMS (Loading 2, 4.5 % variance). Peaks in the positive regime are localized to the ventricle region and have been identified as ceramides.

4.3.8. The effects of matrix on the image and spectral quality of SIMS analysis

MeSIMS is a routine technique employed to improve the ion yields of various compounds. During the course of this investigation, the effect a matrix had on the molecular ion intensity of various lipids in the tissue sample was determined by comparing the lipids profiles from both a native and a matrix-coated tissue section. The normalized lipid profiles obtained from the native and matrix coated tissue are compared directly in Figure 4.7. Neither the molecular ion nor the high mass fragment associated with glycerophosphocholine species was influenced by the presence of the matrix in the sample.

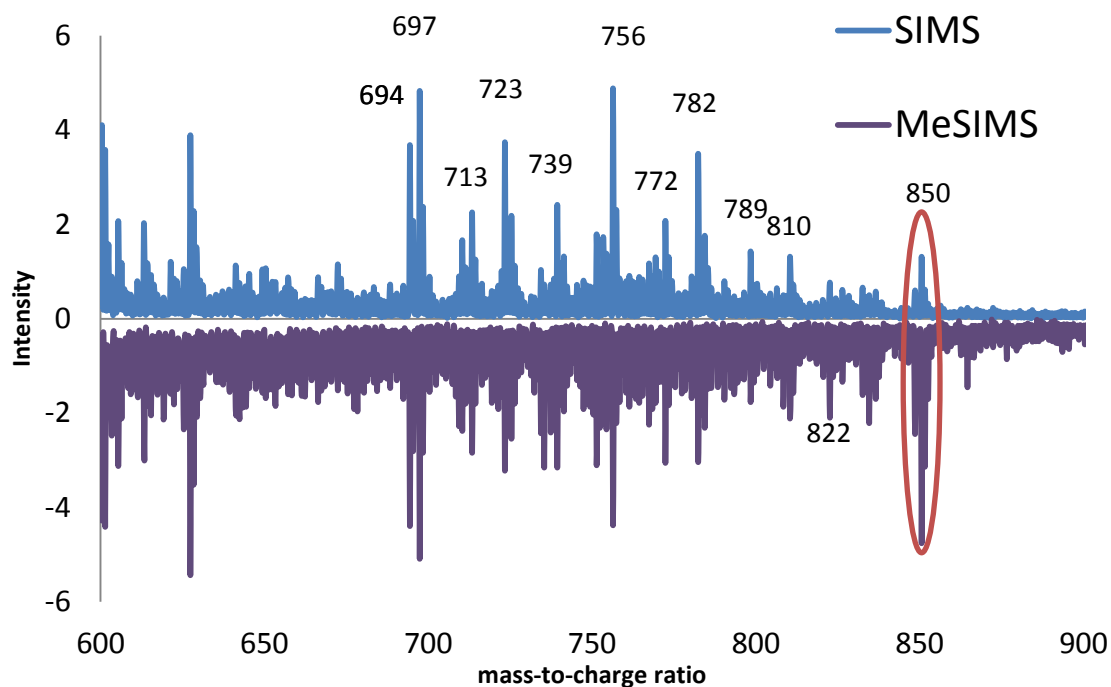


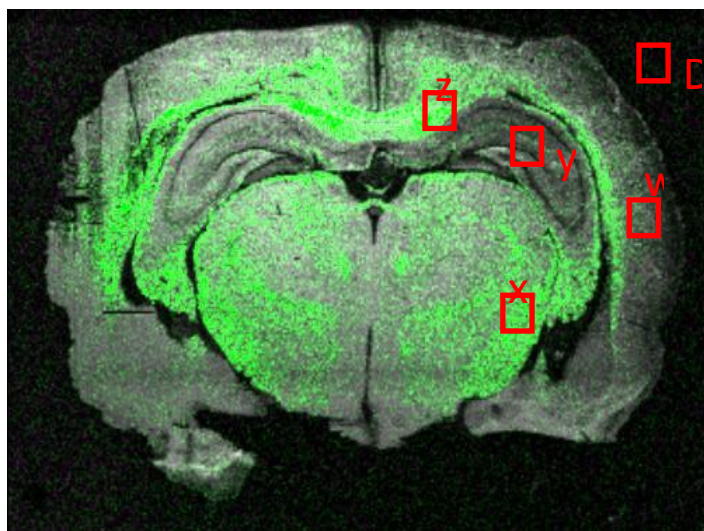
Figure 4.7. The SIMS (blue) and MeSIMS (purple) spectra of the lipid region have the same lipid peaks with similar relative intensities for the glycerophosphocholine-related peaks. However, the molecular ion intensity of galactoceramides related peaks at m/z 810, 822 and 850 are enhanced in the presence of the matrix (circle).

Four regions representing different anatomical features in the brain—corpus callosum (area Z), cerebral cortex (area W), hippocampus (area Y), and the thalamus (area X)—were selected and their chemical signatures were compared (see Table 4.2). The ion yield for both glycerophospholipid and galactoceramides species were enhanced in the white matter (regions Z and X). The degree of enhancement for the galactoceramides was three times greater than that for the glycerophospholipids in the same region, suggesting a preferential ionization favoring this class of lipid. Surprisingly, the presence of the matrix did not enhance the desorption and ionization of glycerophospholipids in regions associated with gray matter (regions Y and W), making glycerophospholipid enhancement site specific. This experiment shows that the surrounding chemical environments are highly influential during desorption and ionization. The addition of the matrix changed the chemical environments, altering the dynamics of both processes. The benefit of improved molecular sensitivity was countered with tradeoffs, including increased spectral complexity and skewed quantification.

SIMS was not used solely to analyze the effect of the sample preparation method on molecular displacement in the sample. In this investigation, the SIMS analysis of the matrix-coated tissue section also showed that the matrix had no aberrant effect on the lateral resolution. At resolutions appropriate for probing large tissue sections (e.g., 25-100 μm), the lateral displacement typically observed with solvent-based matrix application methods was avoided (see Figure 4.8).

ToF-SIMS was also used to evaluate the homogeneity and uniformity of the matrix layer applied to the tissue sample using the solvent-free sublimation technique.

After the matrix application, signals related to the matrix were examined to elucidate chemical interaction between it and the sample. Various regions on and off the tissue were selected (area = 13 pixels²), and the intensities of matrix-related peaks were averaged and compared. The experiment showed a significantly higher matrix signal on the substrate (175.1 ± 13.7 counts per pixel) compared to regions on the tissue (80.8 ± 10.0 counts per pixel). The lower matrix signal on the tissue suggests that the matrix may have penetrated or been absorbed into the tissue during the sublimation process.



Region	m/z 850	m/z 756
Z	15.2 ± 2.8	5.6 ± 2.0
Y		1.0 ± 1.1
X	7.8 ± 2.1	4.7 ± 2.3
W		0.8 ± 1.0

Figure 4.8. ToF-SIMS image of a coronal rat brain section with alpha-cyano matrix, an overlay of lipid fragment phosphocholine at m/z 184 (black and white) and sodiated galactoceramide at m/z 850.5. Tissue section 16.4 x 11.6 mm

Although the solvent-free sublimation matrix application technique had no aberrant effect on the lateral resolution, the presence of the matrix changed the relative intensity of some lipid species; however, the effect was dependent on the region and the lipid class.

4.4. Conclusions

In this investigation, the high lateral resolution of ToF-SIMS in combination with tandem MS capabilities provided a powerful analytical platform for the characterization of lipids directly off the surface of tissue. The distribution and identification of various lipid species, including glycerophospholipids, sphingolipids, cholesterol and vitamin E, was performed on this model at both the macroscopic and the microscopic scale. The ability of the C₆₀-QSTAR to separate isobaric stereoisomers was used to distinguish and identify unsaturated galactoceramides lipids with sphingosine (d18:1) and monosaturated galactoceramides lipids with sphinganine (d18:0) backbones in the tissue sample. This method is also applicable for both hydroxy and non-hydroxy functionalized subclasses of galactoceramides whose detection is convoluted by isobaric interference.

Recent advances in instrumentation and sample preparation protocols are pushing the limits of spatial resolution and sensitivity in order to expand the analytical capabilities of SIMS. In this study, matrix-assisted SIMS was utilized to increase the sensitivity of the technique; however, findings confirm that the process is environmentally selective and species dependent. Nonetheless, the solvent-free sample preparation technique successfully incorporated the MALDI matrix into the tissue without disturbing the original location of chemicals on the surface. In the future, we hope to obtain both the lateral resolution and instrumental sensitivity needed to detect sub-cellular localizations in order to further elucidate biological processes *in situ*.

4.5. References

1. Fuchs, B.; Suss, R.; Schiller, J., An update of MALDI-TOF mass spectrometry in lipid research. *Prog. Lipid. Res.* **2010**, *49* (4), 450-475.
2. McDonnell, L. A.; Heeren, R. M. A., Imaging mass spectrometry. *Mass Spectrom. Rev.* **2007**, *26* (4), 606-643.
3. Murphy, R. C.; Hankin, J. A.; Barkley, R. M., Imaging of lipid species by MALDI mass spectrometry. *J. Lipid Res.* **2009**, *50*, S317-S322.
4. Dill, A. L.; Ifa, D. R.; Manicke, N. E.; Zheng, O. Y.; Cooks, R. G., Mass spectrometric imaging of lipids using desorption electrospray ionization. *Journal of Chromatography B-Analytical Technologies in the Biomedical and Life Sciences* **2009**, *877* (26), 2883-2889.
5. Manicke, N. E.; Wiseman, J. M.; Ifa, D. R.; Cooks, R. G., Desorption electrospray ionization (DESI) mass Spectrometry and tandem mass spectrometry (MS/MS) of phospholipids and sphingolipids: Ionization, adduct formation, and fragmentation. *Journal of the American Society for Mass Spectrometry* **2008**, *19* (4), 531-543.
6. Hankin, J. A.; Murphy, R. C., Relationship between MALDI IMS Intensity and Measured Quantity of Selected Phospholipids in Rat Brain Sections. *Analytical Chemistry* **2010**, *82* (20), 8476-8484.
7. Jackson, S. N.; Ugarov, M.; Egan, T.; Post, J. D.; Langlais, D.; Schultz, J. A.; Woods, A. S., MALDI-ion mobility-TOFMS imaging of lipids in rat brain tissue. *Journal of Mass Spectrometry* **2007**, *42* (8), 1093-1098.
8. Jackson, S. N.; Wang, H. Y. J.; Woods, A. S., In situ structural characterization of phosphatidylcholines in brain tissue using MALDI-MS/MS. *Journal of the American Society for Mass Spectrometry* **2005**, *16* (12), 2052-2056.
9. Adriaensen, L.; Vangaever, F.; Lenaerts, J.; Gijbels, R., Matrix-enhanced secondary ion mass spectrometry: the influence of MALDI matrices on molecular ion yields of thin organic films. *Rapid Communications in Mass Spectrometry* **2005**, *19* (8), 1017-1024.
10. Fitzgerald, J. J. D.; Kunnath, P.; Walker, A. V., Matrix-Enhanced Secondary Ion Mass Spectrometry (ME SIMS) Using Room Temperature Ionic Liquid Matrices. *Analytical Chemistry* **2010**, *82* (11), 4413-4419.
11. Nygren, H.; Malmberg, P., High-resolution imaging and proteomics of peptide fragments by TOF-SIMS. *Proteomics* **2010**, *10* (8), 1694-1698.
12. Roddy, T. P.; Cannon, D. M.; Ostrowski, S. G.; Ewing, A. G.; Winograd, N., Proton transfer in time-of-flight secondary ion mass spectrometry studies of frozen-hydrated dipalmitoylphosphatidylcholine. *Analytical Chemistry* **2003**, *75* (16), 4087-4094.
13. Wucher, A.; Sun, S.; Szakal, C.; Winograd, N., Molecular depth profiling in ice matrices Using C-60 projectiles. *Applied Surface Science* **2004**, *231*, 68-71.
14. Murayama, Y.; Komatsu, M.; Kuge, K.; Hashimoto, H., Enhanced peptide molecular imaging using aqueous droplets. *Applied Surface Science* **2006**, *252* (19), 6774-6776.

15. Hankin, J. A.; Barkley, R. M.; Murphy, R. C., Sublimation as a method of matrix application for mass spectrometric imaging. *Journal of the American Society for Mass Spectrometry* **2007**, *18*, 1646-1652.
16. Schwartz, S. A.; Reyzer, M. L.; Caprioli, R. M., Direct tissue analysis using matrix-assisted laser desorption/ionization mass spectrometry: practical aspects of sample preparation. *Journal of Mass Spectrometry* **2003**, *38* (7), 699-708.
17. Liu, Q.; He, L., Ionic Matrix for Matrix-Enhanced Surface-Assisted Laser Desorption Ionization Mass Spectrometry Imaging (ME-SALDI-MSI). *Journal of the American Society for Mass Spectrometry* **2009**, *20* (12), 2229-2237.
18. Yang, H. J.; Sugiura, Y.; Ishizaki, I.; Sanada, N.; Ikegami, K.; Zaima, N.; Shrivastava, K.; Setou, M., Imaging of lipids in cultured mammalian neurons by matrix assisted laser/desorption ionization and secondary ion mass spectrometry. *Surface and Interface Analysis* **2010**, *42* (10-11), 1606-1611.
19. Nygren, H.; Borner, K.; Hagenhoff, B.; Malmberg, P.; Mansson, J. E., Localization of cholesterol, phosphocholine and galactosylceramide in rat cerebellar cortex with imaging TOF-SIMS equipped with a bismuth cluster ion source. *Biochimica Et Biophysica Acta-Molecular and Cell Biology of Lipids* **2005**, *1737* (2-3), 102-110.
20. Cammer, W. T. N. a. W., *Chemical Pathology of Disease Involving Myelin*. Plenum Press: New York, 1984.
21. Bansal, R.; Gard, A. L.; Pfeiffer, S. E., Stimulation of oligodendrocyte differentiation in culture by growth in the presence of a monoclonal-antibody to sulfated glycolipids. *Journal of Neuroscience Research* **1988**, *21* (2-4), 260-267.
22. Hankin, J. A.; Farias, S. E.; Barkley, R.; Heidenreich, K.; Frey, L. C.; Hamazaki, K.; Kim, H. Y.; Murphy, R. C., MALDI Mass Spectrometric Imaging of Lipids in Rat Brain Injury Models. *Journal of the American Society for Mass Spectrometry* **2011**, *22* (6), 1014-1021.
23. Henderson, A.; Fletcher, J. S.; Vickerman, J. C., A comparison of PCA and MAF for ToF-SIMS image interpretation. *Surface and Interface Analysis* **2009**, *41* (8), 666-674.
24. Pacholski, M. L., Principal component analysis of TOF-SIMS spectra, images and depth profiles: an industrial perspective. *Applied Surface Science* **2004**, *231*, 235-239.
25. Vaidyanathan, S.; Fletcher, J. S.; Henderson, A.; Lockyer, N. P.; Vickerman, J. C., Exploratory analysis of TOF-SIMS data from biological surfaces. *Applied Surface Science* **2008**, *255* (4), 1599-1602.
26. Magnusson, Y. K.; Friberg, P.; Sjoval, P.; Malm, J.; Chen, Y., TOF-SIMS Analysis of Lipid Accumulation in the Skeletal Muscle of ob/ob Mice. *Obesity* **2008**, *16* (12), 2745-2753.
27. Park, J. W.; Cha, M. J.; Shon, H. K.; Kim, S. H.; Lee, T. G.; Moon, D. W.; Hwang, K. C., ToF-SIMS analysis of myocardial infarcted tissue. *Surface and Interface Analysis* **2011**, *43* (1-2), 350-353.
28. Park, J. W.; Shon, H. K.; Yoo, B. C.; Kim, I. H.; Moon, D. W.; Lee, T. G., Differentiation between human normal colon mucosa and colon cancer tissue using ToF-SIMS imaging technique and principal component analysis. *Applied Surface Science* **2008**, *255* (4), 1119-1122.

Chapter 5

Characterization Lipids on a cell model with Imaging Cluster SIMS

Abstract:

An isolated R2 neuron obtained from *aplysia californica*, an organism with a well-define neural network, was imaged with C₆₀-SIMS and its lipid content analyzed *in situ*. A major lipid component of the neuron membrane at m/z 746.6 was identified as 1-O-hexadecyl-2-oleoyl-*sn*-glycero-3-phosphocholine (GPCho (16:0e/18:1)) using tandem MS. Normal phase LC-MS was also used to confirm this assignment. SIMS images reveal heterogeneous distributions of intact lipid species GPCho (16:0e/18:1), vitamin E and cholesterol on the surface of a single neuron. GPCho (16:0e/18:1) and vitamin E have been previous linked to the biosynthesis of platelet activating factor (PAF) an important cellular mediator; therefore the presence and relative distribution of these molecules on a single cell are potentially valuable in studying this biochemical pathway.

5.1. Introduction

In this investigation, SIMS and MALDI methodologies were used together to characterize the lipid content of a single neuron. Since C_{60} -SIMS is currently the only mass spectrometry based technique capable of detecting sub-cellular localization of intact lipid in a single cell, this technique was used to map the localization of various lipid species across the surface of a single neuron. For single cell imaging experiments, molecular ion sensitivity is often a major challenge due to the limited amount of material in the sample. When sensitivity issues hamper lipid identification efforts, MALDI was used to provide additional spectral information. The two complimentary datasets were used to make lipid assignments and map their respective distribution across the surface of a single neuron.

In an attempt to understand complex neurological processes such as learning and memory storage, the neural network of *aplysia californica* is often utilized as a model system. *Aplysia californica* are the subject of several electrochemical-based neurobiological investigations, the majority of which focus on the learned behavior surrounding the gill and siphon withdrawal reflex (GSWR).¹ The GSWR is a defense mechanism, in which the animal retracts its gills and siphon in response to external stimuli. The sensory and motor neurons needed to accomplish this task are well characterized. Although extensive electrochemical investigations have been conducted to characterize the uptake and release of neurotransmitters, there are limited mass spectrometry-based experiments and few lipidomic investigations.

The simplicity and relative size of the individual neuron in the aplysia's neurologic system is the reason this system is popular in neurobiological studies. The nervous system of high ordered mammals are composed of over a billion neurons with cell bodies ranging from 10 -100 μm in size. In contrast, the nervous system of an aplysia has a few thousand neurons (~20,000) and can be up to 1 mm in size.¹ The size of the individual neurons allows dissection the ganglia and extraction of individual cells by hand with the assistance of a light microscope. Its simplicity allows for the characterization of the aplysia's nervous system, by examining the morphology, intra-neural associations and stimulated response of individual neurons. Over 30 cells in the abdominal ganglia have been identified and characterized by Frazier and coworkers.²

In this study the R2 cell was isolated for SIMS studies. The R2 neuron is easily identified since it is the largest and most deeply pigmented neuron in the right hemiganglia of the abdominal ganglia (see Figure 5.1). Characteristically, the R2 cell has a translucent appearance due to the lack of granules in the cytoplasm. R2 cells are described as silent, unlike other cells that fire spontaneously or rhythmically, since the R2 cell responds only when stimulated. From gross dissection and stimuli response studies, connections within the abdominal neural circuitry are mapped. The R2 neuron is one of three neurons (e.g. L1 and R1) in the abdominal ganglia that are connected to the right pleural ganglia and therefore able to communicate with other ganglia. The R2 neuron also has a dendrite that terminates at a gland in the skin. Therefore, the R2 cell is unique in that it is the only neuron that is connected to both the periphery and the adjacent neural ganglia. The early appearance of the R2 cell during the development process and its

presence within similar species, hints to its significance in the function of neural networks.^{3,4}

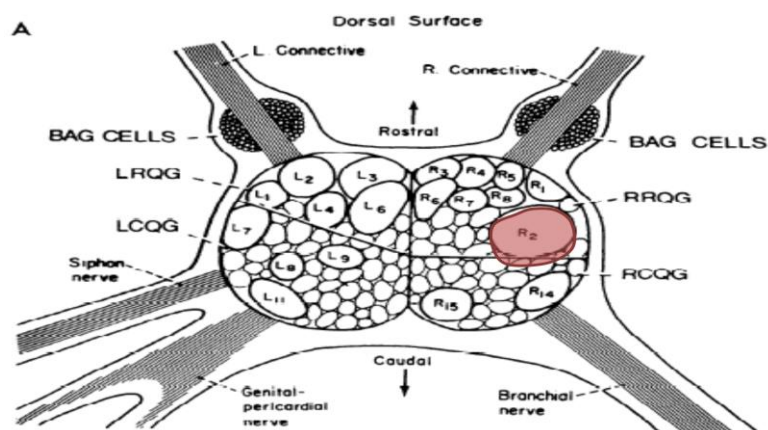


Figure 5.1. The topographical distribution of identified neurons in the abdominal ganglia as view from the dorsal surface is illustrated. The R2 neuron is the largest cell in the right hemisphere (red), its axons extend into the right connective tissue and the branchial nerve.

Although lipids represent about half of the dry weight of a mammalian brain, there are a limited number of neural lipidomic investigations. The role of lipids in the function of the brain is still not fully understood. Although an integral component of cell membranes, some lipid species also participate in cellular signaling. Since the function of neurons depends upon the transmission of signals, understanding the role of lipids in this process is needed.

The lipid content of the aplysia's neural ganglia has been previously characterized.⁵ From this study it was determined that more than half of the glycerophospholipid content (51%) was composed of GPCho. The second half of the lipid composition was split between GPEth (28%), GPSer and GPIIns (10 %) and the glycerophosphosphingolipid, ceramide-2-amino ethylphosphonate (CAEPn) (11%). CAEPn is commonly found in invertebrate animals and is considered to be homologous

to sphingomyelin found in higher order mammals. The extraction and separation methods utilized in this investigation are crude based upon modern standards. Here we examine the lipid content of the same system with imaging mass spectrometry at a single cell level.

5.2 Experimental

5.2.1. Sample preparation

The *aplysia californica* sea slugs were euthanized with magnesium chloride. The ganglia were extracted and incubated in a protease solution for 10 minutes. Individual cells were extracted and placed upon silicon substrates. Lipids were extracted from aplysia ganglia using a modified version of the protocol established by Folch and coworkers.⁶ Due to the high salinity of the aplysia's native environment, deionized water was substituted for the salt solution (NaCl) typically employed in the phase separating step of a Folch extraction.

5.2.2. Instrumentation

The C₆₀-QSTAR instrument was used to image and analyze the lipid content of the aplysia neuron. Images were obtained in ToF-MS mode and each pixel was bombarded with a 10 pA C₆₀ beam for 1 second. The dimensions for the R2 neuron image were 1.91x 0.81 mm at 10 micron resolution. Tandem MS analyses were

performed *in situ* using 50 μ J nitrogen MALDI laser. In this analysis the precursor ion was selected with unit resolution in the Q_1 mass filter and fragmented using 40 eV of collision energy. MALDI spectral data was summed over 300 laser shots (15 Hz, 20s) for tandem MS mode and 900 laser shots (15 Hz, 60s) for ToF-MS acquisitions. A 10 mg/ml solution of 2,5-dihydroxy benzoic acid (DHB) in methanol was used as the MALDI matrix and applied using the dry-drop method.

5.3. Results and discussion

5.3.1 Lipid identification

The SIMS lipid profile obtained from the surface of a single neuron is shown in Figure 5.2a. The major peaks in the SIMS lipid profile were m/z 709.5, 719.5, 725.5, 768.5 and 784.5. For comparison purposes, a MALDI spectrum of a collection of neurons is shown in Figure 5.2b. The two spectra exhibit similarities and differences, as discussed below.

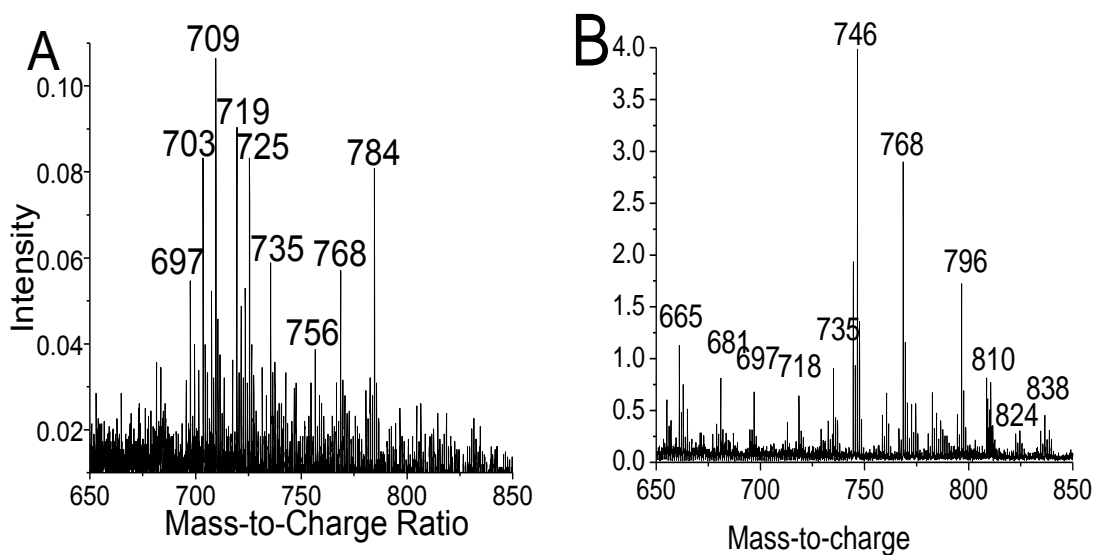


Figure 5.2. ToF-SIMS spectrum (A) obtained from a single aplysia neuron and MALDI spectrum (B) taken from a collection of aplysia neurons.

Table 5.1. Summary of lipids found on the surface of a single neuron from an *aplysia californica*.

Sub-class [LM_ID]	label(C:DB)	Exp. Mass	Species	SIMS	MALDI
Glycerophospholipids /	GPCho(18:1e/16:0)	746.6	[M+H] ⁺		x
Glycerophosphocholines/		768.5	[M+Na] ⁺	x	x
1-alkyl, 2-acylglycerophosphocholines		709.5	[M+Na-N(CH ₃) ₃] ⁺	x	
[GP0102]		784.6	[M+K] ⁺	x	x
		725.5	[M+K- N(CH ₃) ₃] ⁺	x	
	GPCho (18:1e/18:1)	772.5	[M+H] ⁺		x
		794.5	[M+Na] ⁺		x
		735.5	[M+Na- N(CH ₃) ₃] ⁺	x	x
		810.5	[M+K] ⁺		x
		751.5	[M+K- N(CH ₃) ₃] ⁺	x	
Glycerophospholipids /	GPCho (16:0/16:0)	756.5	[M+Na] ⁺	x	x
Glycerophosphocholines/		697	[M+Na-N(CH ₃) ₃] ⁺	x	x
Diacylglycerophosphocholines/	GPCho (18:1/16:0)	760	[M+H] ⁺		x
[GP0101]		798.5	[M+K] ⁺		x
		723.5	[M+K- N(CH ₃) ₃] ⁺		x
	VIT E	430.3	[M*] ⁺	x	x
	CH	369.352125	[M+H-H ₂ O] ⁺	x	x

	386.354865	[M-H] ⁺	x	x
Unknown	719.5		x	x
	726.5		x	
	759.5		x	
	721.5		x	
	703.5		x	
GPCho	184	Fragment	x	x
CAEPn	126	Fragment	x	x
GPEthn	142	Fragment	x	x

Tandem MS strategies developed in Chapter 3 were used to identify the lipids detected in the SIMS image. This task was initially performed *in situ* without the use of extraction, derivatization and chromatographic separation techniques. Biological salts are typically a challenge for *in situ* mass spectrometric investigations due to their detrimental effect on quantification. However, in this investigation, salt adducted lipids were used to identify the major lipid component in the cell membrane of an R2 neuron.

The tandem MS spectra of the molecular ion, sodiated adducted, and high mass fragments were combined to identify the exact structure of the major lipid component. (see Figure 5.3) The tandem MS spectrum of the unknown lipid at m/z 746 yields only one fragment at m/z 184, which represents the phosphocholine headgroup. With this information the identification of the unknown lipid at m/z 746 can be narrowed to three possible lipid species, GPCho (34e:1), GPCho(34p:0) and GPCho(33:1a). Lipids with an odd number of carbons in the fatty acid chains are typically rare since the major biosynthetic pathways predominately synthesize fatty acid chains with an even number of carbons. Therefore even though lipid GPCho 33a:1 has all the structural components detected in the tandem MS spectrum, it can be ruled out due to biological improbability.

The other possible lipids, 34e:1 GPCho and 34p:0 GPCho are ether lipids, a subclass of glycerophospholipids. Although structurally similar to acyl lipids, they are produced from different starting materials, e.g. fatty alcohols instead of fatty acids, and the biosynthetic pathway is distinct from acyl glycerophospholipids. Structurally the two ether lipids differ from typical glycerophospholipids by the linkage between the glycerol backbone and the fatty hydrocarbon. Plasmalogen are ether lipids with an O-alk-1-enyl glycerol – fatty alcohol linkage. In order to distinguish 34e:1 GPCho and 34p:0 GPCho lipid the location of the double bond needs to be determined. If the double bond is located on the acyl fatty acid moiety then the unknown lipid is 34e:1 GPCho. If the double bond is located on the ether linked moiety then the lipid is a plasmalogen, 34p:0 GPCho.

Tandem MS spectrum for the sodiated-adducted lipid reveals fragments at m/z 709.5, 627.5, 585.4, 563.4, 482.3, 464.3, 341.3 and 184.07 (see Figure 5.3). As expected the loss of the trimethylamine (TMA) group produces a high mass fragment at m/z 709, also seen in the ToF-MS spectrum. The lyso-related fragments at m/z 482.3 and 464.3 were created by the loss of the fatty acid moiety. In this case, the fatty acid moiety has a m/z value of 281.2, indicative of an 18:1 fatty acid. In addition, the 281.2 fragment representing the 18:1 fatty acid moiety was found in the tandem MS spectrum of the high mass fragment ion at m/z 709.5. Based upon this information the lipid is most likely GPCho(16:0e/18:1). This lipid has an *O*-alkyl ether linkage at the *sn*-1 position attaching a 16:0 fatty alcohol side-chain, a 18:1 fatty acid acyl chain at the *sn*-2 position, and a phosphocholine group at the *sn*-3 position of the glycerol moiety. This structure is shown in Figure 5.3

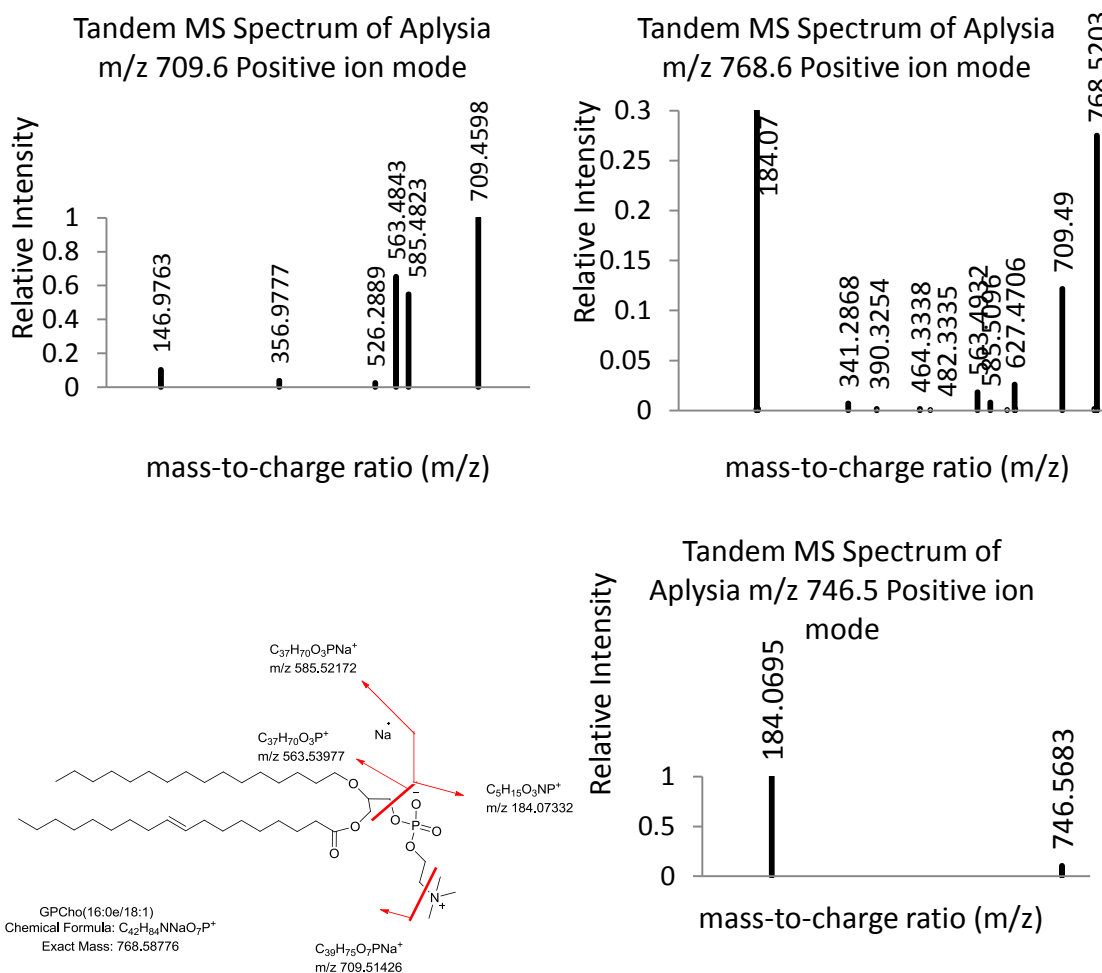


Figure 5.3. Tandem MS spectra of the protonated molecular ion, sodiated adducted and high mass fragment of the major membrane lipid of the R2 neuron. Based on the three spectra that lipid can be identifies as GPCho(16:0 e/ 18:1). Also the structure of GPCho(16:0 e/ 18:1) with locations of fragmentation marked.

In order to confirm the identity of the lipid at m/z 746.5, extraction, separation and reaction chemistry techniques were utilized. The lipid of interest was separated from the extract with normal phase LC/MS/MS (LC retention time = 27 min, see Figure 5.4). An ammonium acetate solution was used to promote ionization in the negative ion

mode, forming an acetate-lipid adduct at m/z 804. Tandem MS of the m/z 804 peak reveals one carboxylate anion (m/z 281.2) corresponding to an 18:1 fatty acid. The single carboxylate anion suggests that the fatty acid linkage in the *sn*-1 position is an ether or plasmalogen lipid. This analysis confirms the identity of the aplysia lipid at m/z 746 to be 1-O-hexadecyl-2-oleoyl-*sn*-glycero-3-phosphocholine 16:0e/18:1 GPCCho ($[M+H]^+$).

Aplysia sample NP-LC/MS/MS m/z 804 neg (m/z 746 + acetate)

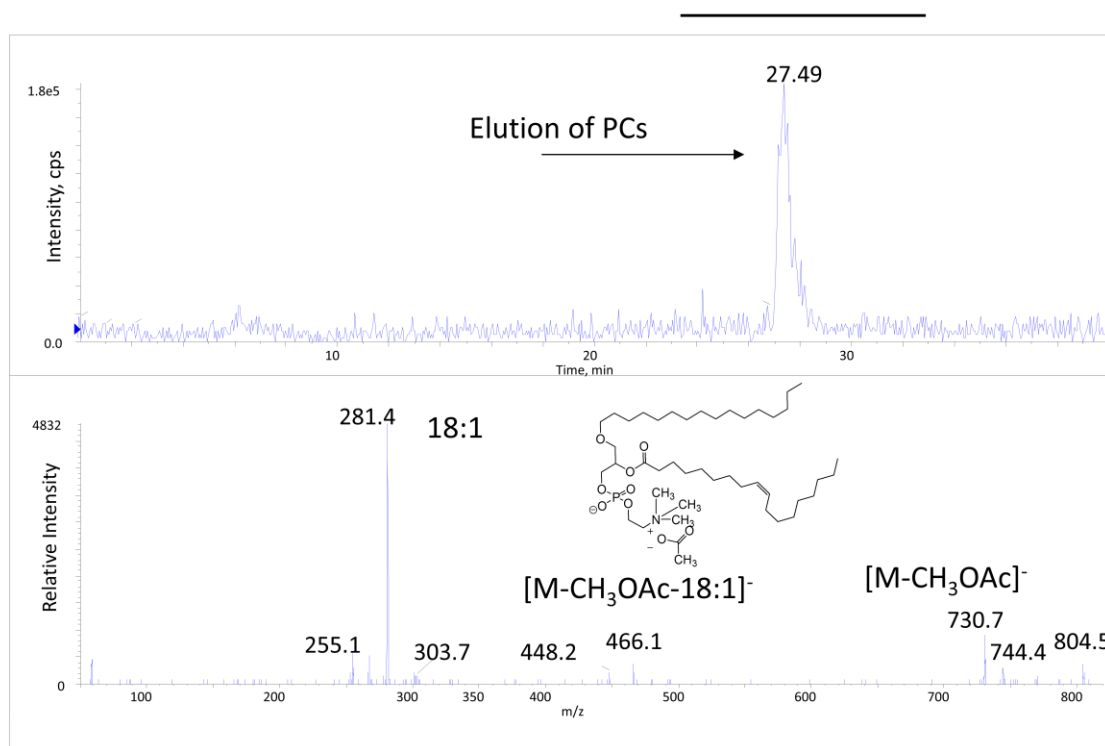


Figure 5.4. The glycerophosphocholine fractions were separated from the other lipids in the lipid extract using normal phase LC/MS/MS, retention time was 27 minutes. Tandem MS spectrum of the lipid acetate adduct at m/z 804 was obtained in the negative ion mode. The higher ratio of the 281.2 (18:1 fatty acid)

The ether lipid is the dominant lipid species detected in the SIMS spectrum of the cell membrane. Although generally minor components of the

mammalian lipidome, ether lipids are typically found in higher abundance in nervous tissue, macrophages, platelets and neutrophils.¹⁰ The exact biological significance of these ether lipids is currently unknown; however, possible structural, functional and evolutionary utilities are discussed below.

The lipid composition of the membrane influences its physical properties, i.e. fluidity and phase transition temperature, and the activity of membrane-dependent proteins. The presence of ether lipids in the cell membrane changes the physical properties of the membrane. Compared to diacyl lipid membranes, a membrane with ether lipids exhibit reduced ion permeability and membrane phase transition temperature, the temperature at which it retain fluidity.⁷⁻⁹ Since *aplysia californica* inhabit high salinity and cold environment these membrane characteristic are potential important to their survival.

Although lipids have important structural roles they are also involved in signaling. 1-O-alkyl-sn-glycero-3-phosphocholine lipids are known precursors to an important cellular mediator known as platelet-activating factor (PAF). PAF is multifunctional; it plays a role in immune response, blocks platelet aggregation and stimulates enzymatic activity for various biological processes. It has been shown that PAF is produced in the brain when subjected to stimuli.¹⁰⁻¹² This research suggests that ether lipid may play an active and important role in the function of neurons. Therefore future imaging experiments of stimulated and non-stimulated neurons may provide valuable information of the neuron functionality.

Thompson and co-workers found that two species of terrestrial slug, the *Arionater* and *Ariolimax columbianus*, also have higher levels of alpha-glyceryl ether

phospholipids.¹³⁻¹⁶ In this lipidomics study, almost half of the phosphocholine species were ether lipids and almost all (94%) of the ether linked fatty acid chains were 16 carbons in length. Based on the similarities in the lipid composition of related species it is possible that evolutionary aspects influence the lipidome of these organisms. It is possible that the biosynthetic pathway for ether lipids is favored in these lower order organisms, resulting in the strong representation of ether lipids in the lipidome. This pathway is still present in higher order organism, but less dominate.

5.3.2. Lipid imaging with C₆₀-SIMS

The SIMS mass spectrum provides a rich array of molecules for imaging; the total ion image is shown in Figure 5.5b. Some molecules can be detected intact (Figure 5.5c-f), but for others sensitivity issues demand that fragment ions be monitored (Figure 5.5g-i).

It is routine for SIMS-based imaging experiments to establish a baseline, a molecule that is homogeneously distributed over the entire sample and whose relative signal intensity can be used to normalize the relative intensity of other detected molecules. In the past, the C₅H₉⁺ ion at m/z 69 has been utilized¹⁷, however, since this ion is below the mass range collected, a new baseline standard was found. In this investigation the unknown ion at m/z 128 was used as the baseline, its homogeneous distribution is seen in Figure 5.5d-f (blue).

The protonated molecular ion of GPCho(16e:0/18:1) at m/z 746.6 was not observed in the SIMS image of the aplysia neuron. However, biological salt adduct at m/z 768.6 $[M+Na]^+$ and 784.6 $[M+K]^+$ were observed in the *in situ* SIMS spectrum. The high mass fragment ion of these adducts, formed due to the loss of the TMA moiety, is observed at m/z 709.5 and m/z 725.5, respectively. All the peaks related to the newly identified GPCho(16e:0/18:1) lipid were summed in Figure 5.5c, including the $[M+Na]^+$, $[M+K]^+$, $[M+Na-N(CH_3)_3]^+$ and $[M+K-N(CH_3)_3]^+$ at m/z 768.5, 784.6, 709.5 and 725.5, respectively. The peak at m/z 709.5 had enough signal intensity to map its distribution across the neuron, Figure 5.5f. This ether lipid has a heterogeneous distribution within the soma. The higher relative intensity of GPCho(16e:0/18:1) in the upper portion of the soma is consistent with the mapped distribution of the phosphocholine headgroup at m/z 184.

Cholesterol and vitamin E were also found in abundance in the R2 neuron. The heterogeneous distribution of cholesterol (m/z 369.3) and vitamin E (m/z 430.3) on the surface of an aplysia neuron is shown in Figure 5.5d-e, respectively. Both molecules have a high intensity region in the upper portion of the soma, however their distribution is not identical to the ether lipid GPCho(16e:0/18:1). Instead the vitamin E localization corresponds to the high pigmentation region observed under the light microscope, Figure 5.5a.

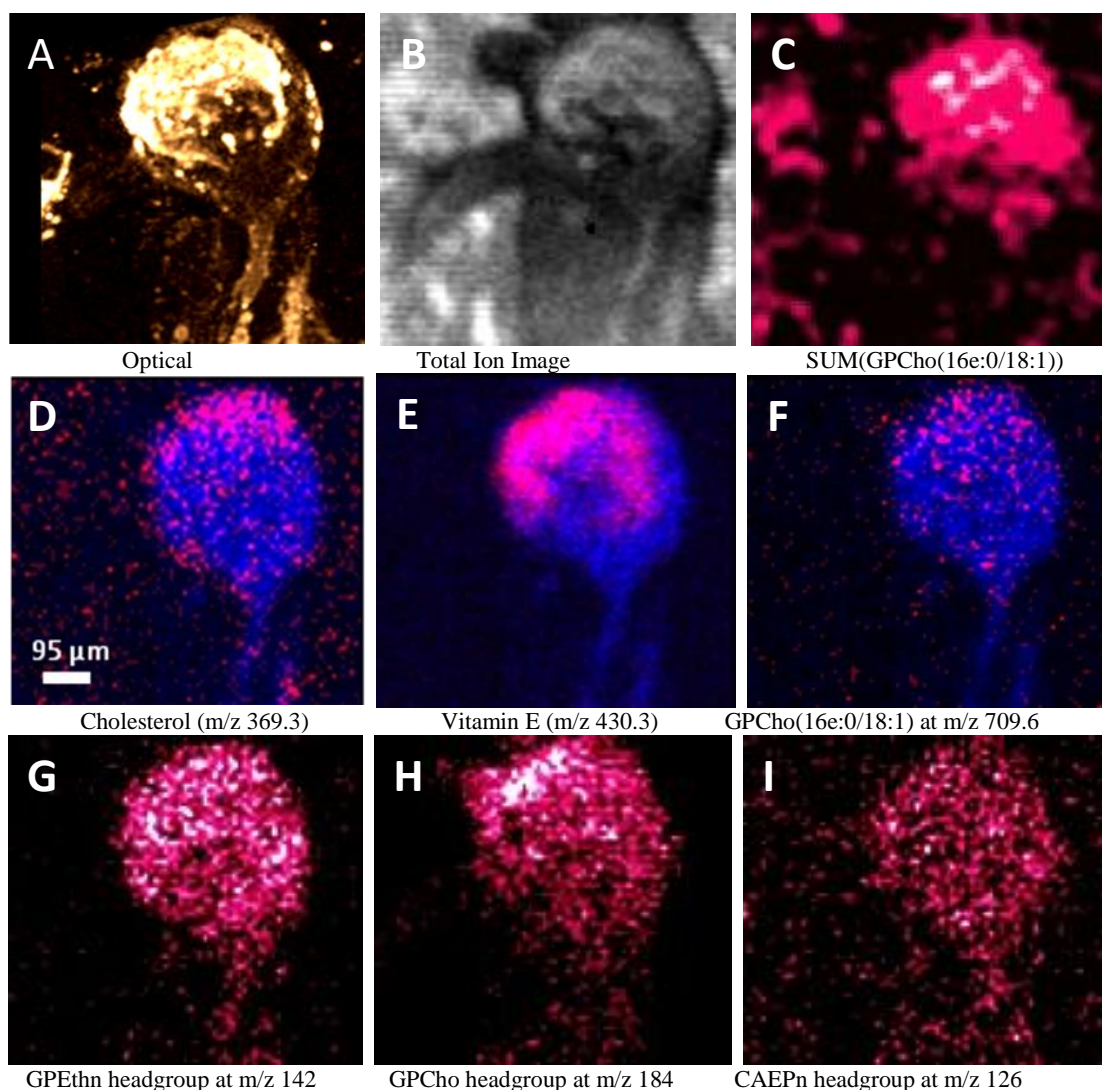


Figure 5.5. ToF-SIMS images of an isolated aplysia R2 neuron from the abdominal ganglia are examined. The optical(a) image was taken at 20 x magnification with a dissecting microscope. The SIMS total ion image is also shown, the soma is approximately 450 x 380 micron (l x w) in size. (b). The summed intensity of all the peaks related to the newly identified ether lipid, GPCho(16e:0/18:1), were overlaid using MatLab (d). Unknown fragment ion at m/z 128 was homogenously distributed across the surface of the neurons soma and axon (blue, d-f). The distribution of cholesterol at m/z 369.3 (d), Vitamin E at 430.3 (e) and high mass fragment of GPCho(16:0e/18:1) at m/z 709.5 (f) was overlaid with the m/z 128 species using TissueView. In the bottom row are the ToF-SIMS images showing the distribution of the lipid headgroup's for GPEthn at m/z 142(g) , GPCho at m/z 184 (h) and CAEPn at m/z 124(i).

Monroe and coworkers have previously shown localization of vitamin E in aplysia with ToF-SIMS imaging.¹⁸ In this study vitamin E (m/z 430) was localized to the junction of the cell soma and neurite. Due to its localization it is hypothesized that vitamin E assists in the transportation of chemical from the soma to the axon. Neurotransmitters and other important biomolecules are synthesized in the neurons soma and transported through the axons to effector sites in the dendrites. The disturbance of this transportation inhibits cellular signaling.

Vitamin E may also play an important role in the biosynthesis of the observed ether lipid. Tran and coworkers have found that Vitamin E enhances the acylation of 1-o-alkyl-sn-glycero-3-phosphocholine, PAF.¹⁹⁻²² In this experiment, increased levels of ether lipids were detected in cell incubated with vitamin E compared to control cells. It was proposed that vitamin E indirectly stimulates the activity of the enzyme that converts PAF(alkyl) into ether lipids (alkylacyl) by enhancing the release of fatty acid from diacyl PC. The ability to visualize the relative distributions of these two molecules on the surface of a single cell is only possible due to the high spatial resolution of C₆₀-SIMS.

Based on the lipidomic analysis performed by Komai and coworkers, previously discussed, 38% of the total lipid content was from GPEthn and CAEPn lipids. In this investigation, intact GPEthn and CAEPn lipids were not detected *in situ*. However, the distribution of their signature headgroups, m/z 142 and m/z 126, are shown in Figure 5.5, along with the phosphocholine headgroup, m/z 184. Since sphingomyelins are not present in this species, the 184 peak represents only the glycerophosphocholine lipids. The CAEPn headgroup (m/z 126) has a uniform distribution throughout the soma,

while GPEth (m/z 142) and GPCho (m/z 184) exhibit heterogenous distributions. In order to fully characterized the GPEthn and CAEPn the intact molecular ion species would need to be observed. At this point, there is not enough sensitivity to observe these ions in imaging mode.

5.4. Conclusions

The results presented here are intended to show that the C₆₀-QSTAR is a useful platform for studying lipids on a cellular level. The high lateral resolution associated with C₆₀-SIMS was used in conjunction with MALDI and tandem MS capabilities to characterize the lipid content of an aplysia neuron. This model system provides a good starting point for future neural lipidomics investigations on mammalian cells which are significantly smaller.

5.5. Reference

1. Kandel, E. R., Neuroscience - The molecular biology of memory storage: A dialogue between genes and synapses. *Science* **2001**, *294* (5544), 1030-1038.
2. Frazier, W. T.; Kandel, E. R.; Kupferma.I; Waziri, R.; Coggesha.Re, Morphological and functional properties of identified neurons in abdominal ganglion of aplysia californica. *Journal of Neurophysiology* **1967**, *30* (6), 1288-&.
3. Kriegstein, A. R., Development of nervous-systems of aplysia-californica. *Proceedings of the National Academy of Sciences of the United States of America* **1977**, *74* (1), 375-378.
4. Kandel, E. R.; Kriegstein, A.; Schacher, S., Development of the central nervous-system of aplysia in terms of differentiation of its specific identifiable cells. *Neuroscience* **1980**, *5* (12), 2033-2063.
5. Komai, Y.; Matsukaw.S; Satake, M., Lipid composition of nervous-tissue of invertebrates aplysia-kurodai (gastropod) and cambarus-clarki (arthropod). *Biochimica Et Biophysica Acta* **1973**, *316* (3), 271-281.
6. Folch, J.; Lees, M.; Stanley, G. H. S., A simple method for the isolation and purification of total lipids from animal tissues. *Journal of Biological Chemistry* **1957**, *226* (1), 497-509.
7. Mukherjee, S.; Chattopadhyay, A., Influence of ester and ether linkage in phospholipids on the environment and dynamics of the membrane interface: A wavelength-selective fluorescence approach. *Langmuir* **2005**, *21* (1), 287-293.
8. Shinoda, K.; Shinoda, W.; Baba, T.; Mikami, M., Comparative molecular dynamics study of ether- and ester-linked phospholipid bilayers. *Journal of Chemical Physics* **2004**, *121* (19), 9648-9654.
9. Yeo, Y. K.; Park, E. J.; Lee, C. W.; Joo, H. T.; Farkas, T., Ether lipid composition and molecular species alterations in carp brain (*Cyprinus carpio* L.) during normoxic temperature acclimation. *Neurochem. Res.* **1997**, *22* (10), 1257-1264.
10. Bito, H.; Nakamura, M.; Honda, Z.; Izumi, T.; Iwatsubo, T.; Seyama, Y.; Ogura, A.; Kudo, Y.; Shimizu, T., Platelet-activating-factor (PAF) receptor in rat-brain - PAF mobilizes intracellular Ca²⁺ in hippocampal - neurons. *Neuron* **1992**, *9* (2), 285-294.
11. Shimizu, T.; Honda, Z.; Nakamura, M.; Bito, H.; Izumi, T., Platelet-activating-factor receptor and signal transduction. *Biochemical Pharmacology* **1992**, *44* (6), 1001-1008.
12. Bito, H.; Honda, Z.; Mutoh, H.; Shimizu, T., Function and expression of platelet-activating-factor (PAF) receptor in rat central-nervous-system. *Journal of Cellular Biochemistry* **1993**, 249-249.
13. Thompson, G. A.; Hanahan, D. J., identification of alpha-glyceryl ether phospholipids as constituents in 2 species of terrestrial slug. *Journal of Biological Chemistry* **1963**, *238* (8), 2628-&.
14. Thompson, G. A., Biosynthesis of ether-containing phospholipids in slug arion ater. I. Incorporation studies in vivo. *Journal of Biological Chemistry* **1965**, *240* (5), 1912-&.

15. Thompson, G. A., Biosynthesis of ether-containing phospholipids in slug arion ater. II. Role of glyceryl ether lipid as plasmalogen precursors. *Biochemistry* **1966**, 5 (4), 1290-&.
16. Thompson, G. A., Biosynthesis of ether-containing phospholipids in slug arion ater. III. Origin of vinylic ether bond of plasmalogens. *Biochimica Et Biophysica Acta* **1968**, 152 (2), 409-&.
17. Ostrowski, S. G.; Van Bell, C. T.; Winograd, N.; Ewing, A. G., Mass spectrometric imaging of highly curved membranes during Tetrahymena mating. *Science* **2004**, 305 (5680), 71-73.
18. Monroe, E. B.; Jurchen, J. C.; Lee, J.; Rubakhin, S. S.; Sweedler, J. V., Vitamin E imaging and localization in the neuronal membrane. *Journal of the American Chemical Society* **2005**, 127 (35), 12152-12153.
19. Tran, K.; Dangelo, A. F.; Choy, P. C.; Chan, A. C., Vitamin-e enhances the acylation of 1-O-alkyl-sn-glycero-3-phosphocholine in human endothelial-cells. *Biochemical Journal* **1994**, 298, 115-119.
20. Fukuzawa, K.; Kurotori, Y.; Tokumura, A.; Tsukatani, H., Increased platelet-activating factor (PAF) synthesis in polymorphonuclear leukocytes of vitamin-E-deficient rats. *Annals of the New York Academy of Sciences* **1989**, 570, 449-454.
21. Fukuzawa, K.; Kurotori, Y.; Tokumura, A.; Tsukatani, H., Vitamin-E-deficiency increases the synthesis of platelet-activating factor (PAF) in rat polymorphonuclear leukocytes. *Lipids* **1989**, 24 (3), 236-239.
22. Kakishita, E.; Suehiro, A.; Oura, Y.; Nagai, K., Inhibitory effect of vitamin-E (alpha-tocopherol) on spontaneous platelet-aggregation in whole-blood. *Thrombosis Research* **1990**, 60 (6), 489-499.

Chapter 6

Conclusions and Future Directions of C₆₀-SIMS

Abstract:

This thesis has described the development of a new C₆₀-SIMS instrument and its ability to characterize the lipids in cells and tissue. Its tandem MS capabilities have been shown to be a powerful tool for the *in situ* identification of lipids. The technique's ability to provide valuable spatial information gives it an edge over traditional ESI-lipid analyzes and its high lateral resolution gives it an advantage of MALDI and DESI imaging. However, sensitivity issues at high lateral resolution are a constant challenge for this high lateral resolution technique. This chapter explores the methods used to improve the sensitivity of SIMS, particularly molecular depth profiling and the use of cryogenic-based analyzes.

6.1. Depth profiling

Molecular depth profiling is a powerful bio-analytical tool unique to C₆₀ SIMS. In this method chemical information is obtained as a function of depth. The advantage of molecular depth profiling in regards to sensitivity, is its ability to turn a pixel into a voxel, a three dimensional pixel. In this process, ion fluences above the static limit are used to remove the surface layer, exposing the subsurface molecules for analysis. With atomic sources this method provides only fragments of organic species

and elemental information. The unique properties of C_{60} , discussed in Chapter 2, greatly reduce the accumulation of damage and allows for the retention of molecular information under dynamic conditions.

For depth profiling, ion beam fluences over the static limit are achieved with a dc ion beam. Unfortunately, conventional ToF-based instruments with coaxial ToFs and pulsed primary ion beams are unable to collect spectra information while the ion beam is continuously running. Therefore, in these instruments depth profiles are collected by continuously alternating between data acquisition using a pulsed beam and sputtering using a dc ion beam. Since spectral information is not collected during the sputtering processes this acquisition method is inefficient. These dynamic duty cycle losses can be recovered in the C_{60} -QSTAR instrument, since its orientation allows it to be compatible with a continuous ion beam. The C_{60} -QSTAR instrument needs additional improvements in order to fully capitalize on its unique ability to retain high mass resolution with a continuous ion beam. The full potential of this function has not been fully investigated. However, some preliminary data has been obtained and is presented here.

Trehalose thin films are an established model system for molecular depth profiling.¹⁻³ These samples are typically prepared by spin coating a solution of trehalose (0.5 M, DI) on piranha etched silicon wafers. In a typical depth profile, shown in Figure 6.1, the intensity of a trehalose ion is plotted as a function of ion fluence. The depth profile consists of three distinct regions; the surface signal, steady state and the interface region. At the surface, the ion signal is often the most intense. As fluence surpasses the static limit, an exponential decay of signal, known as the disappearing cross-section (σ_{eff}),

is observed. The disappearing cross section, equation 6.1, combines the signal lost from the sputtering event and ion beam induced damaged cross section (σ_D).

$$\sigma_{eff} = \frac{Y^{tot}}{nd} + \sigma_D \quad \text{Equation 6.1}$$

In this equation, Y_{tot} is total sputtering, d represents the thickness of the altered layer and n is the molecular density of the analyte. The signal intensity eventually levels out into a steady state, as the removal of secondary ions and damage accumulation reaches equilibrium. The ratio of molecular ion signal at steady state (S_{ss}) and the molecular ion signal before high fluence sputtering (S_o) is proportional to the concentration of analyte at the surface (c_s) and in the bulk (c_b). This equation expresses the relationship between signal, concentration and sputter yields.

$$\frac{S_{ss}}{S_o} = \frac{Y^{tot}}{Y^{tot} + nd\sigma_D} = \frac{c_s}{c_b} \quad \text{Equation 6.2}$$

The trehalose signal remains at steady state until the interface is reached. At this point, the trehalose signals disappear and substrate-related ion signals, m/z 28 and m/z 87, are detected. The slope of the interface is used to determine the depth resolution of the system.

The depth profile obtained on the C₆₀-QSTAR looks similar to the established model system, except for one obvious difference, the lack of a steady state (see Figure 6.2). The inability to reach a steady state indicates continuous damage accumulation. The high pressure in the sample region may be linked to this issue. Fragments produced by collisions between the C₆₀ projectile and inert nitrogen sweeping gas, may damage the surface of the sample. Further investigation into the effects of pressure on molecular depth profiling is needed to fully understand this issue.

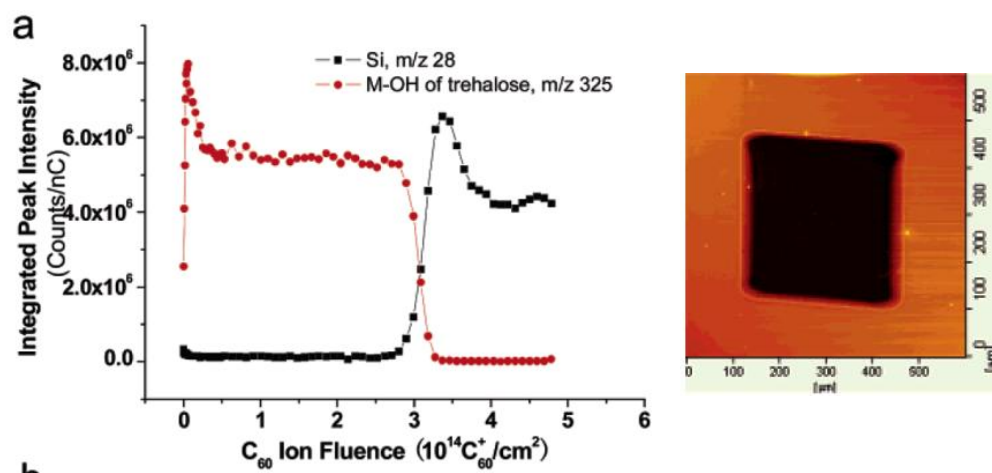


Figure 6.1. The molecular depth profile analysis of trehalose. The intensity of the molecular ion of trehalose at m/z 325 and a silicon peak at m/z 28 are plotted as a function of C_{60}^+ ion fluence. Based on atomic force microscope measurements, the crater's dimensions were approximately $300 \mu\text{m} \times 300 \mu\text{m} \times 240 \text{nm}$, (length \times width \times depth).

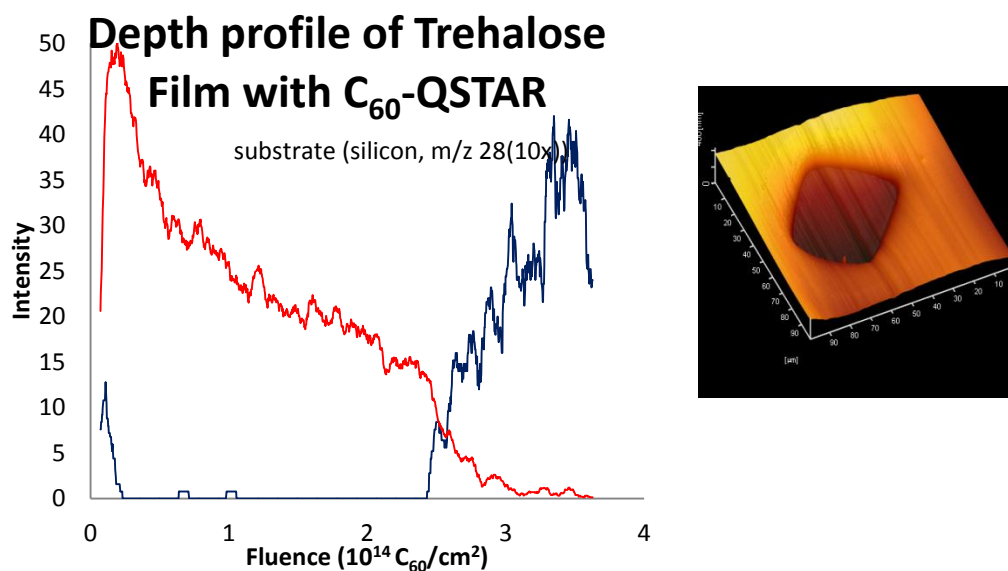


Figure 6.2. Molecular depth profile of Trehalose film on a silicon wafer. The intensity of the sodiated-molecular ion of trehalose at m/z 365 and a silicon oxide peak at m/z 87 (Si_2O_2^+) are plotted as a function of primary ion fluence. An atomic force microscope (AFM) was used to measure the dimensions of the crater produced during the analysis. The film was approximately $44.8 \mu\text{m} \times 48.2 \mu\text{m} \times 171.8 \text{nm}$, 5pA beam current.

6.2. Cold stage for the C₆₀-QSTAR instrument

Recent improvement made to the C₆₀-QSTAR instrument's imaging capabilities, discussed in Chapter 2, was enough to allow for analyses at the single cell level. Unfortunately, interfacing cells with the biologically unfavorable vacuum conditions is a major challenge. Careful consideration is needed to maintain the chemical and spatial integrity of the sample throughout the analysis. Analyzing cell in a frozen hydrated state is a widely accepted sample preparation technique.^{4,6} However, the sample region of the C₆₀-QSTAR instrument is not equipped to analyze frozen hydrated cells.

In addition to preserve the integrity of the sample, two additional advantages associated with cryogenic analyses have been found. Piwovar and coworkers found enhanced molecular ion signals for various organic compounds, including phospholipids when analyzing thin films at cryogenic temperature for both static and dynamic analyses⁷. Under static conditions, studies reveal that a proton transfer between the water matrix and the lipid molecules is responsible for the enhanced phospholipid signals observed at cryogenic temperatures. During depth profiling, damage accumulation is responsible for reduced ion signals and degraded depth resolution at increased depths³. Cooling the sample to liquid nitrogen temperatures has been found to reduce the damage accumulation. The molecular depth profile of a 1,2-dipalmitoyl-sn-glycero-3-phosphocholine (GPCho(32:0)) thin film, Figure 6.3, demonstrates the advantage of cryogenic temperatures in both static and dynamic analyzes.⁷

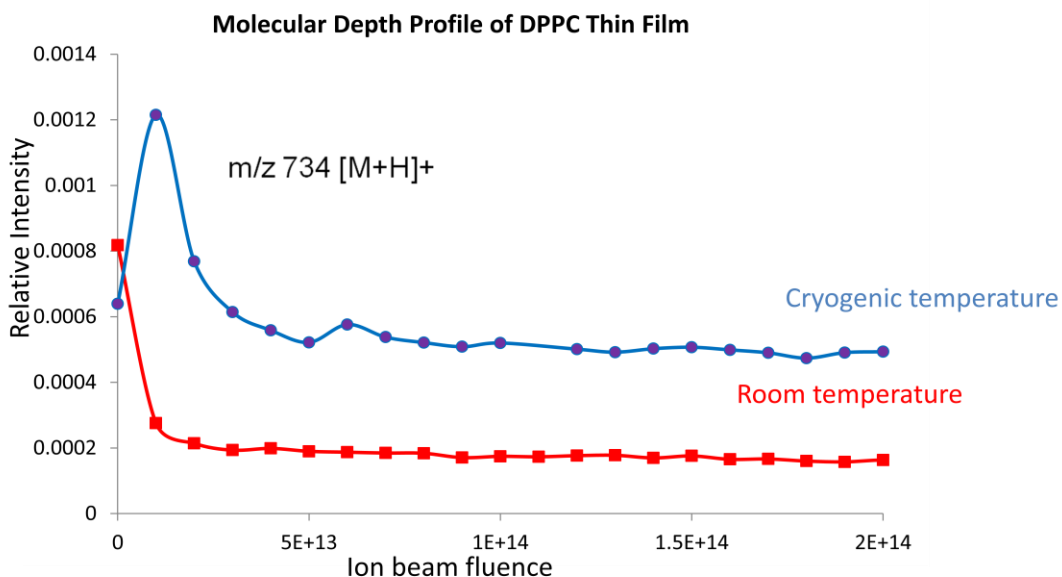


Figure 6.3. Molecular depth profile of a thin film of lipid standard DPPC at room temperature and at cryogenic temperatures. The secondary ion yields of the GPCho(32:0) protonated molecular ion was higher for films examined under cryogenic conditions compared to a film analyzed at room temperature for both static and dynamic analyzes.

In order to benefit from the advantages associated SIMS analyzes at cryogenic conditions, a prototype cold stage for the C₆₀-QSTAR, Figure 6.4, is currently being developed that would allow for analyzing biological samples in a frozen hydrated state. In this design the sample is attached to a copper stage cooled with liquid nitrogen (77 K). A thermocouple probe was added to monitor the stage temperature during analyses.

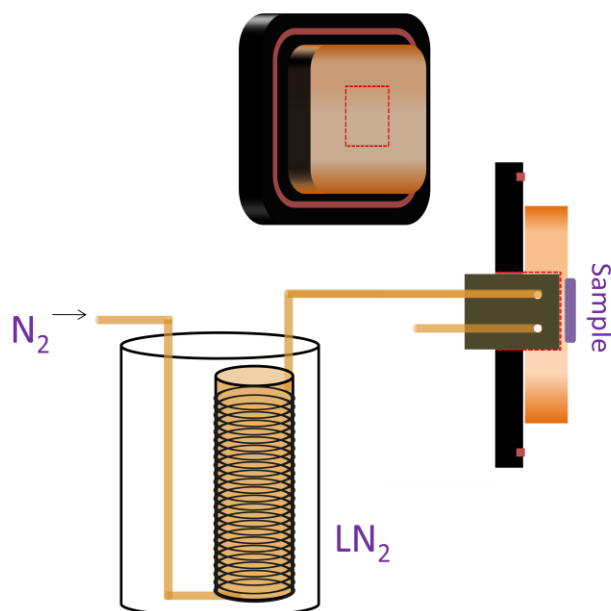


Figure 6.4. The schematic depicts the prototype cold stage for the C_{60} -QSTAR instrument. The sample is cooled via a copper cold finger that is inserted into the back of the sample stage. In this device, nitrogen gas (initially at room temperature) is cooled as it travels through a coil of copper tubing submerged in a dewar of liquid nitrogen. After the nitrogen is cooled it travels to the cold finger attached to the stage.

A thin film of lipid, 1,2-dihexadecanoyl-sn-glycero-3-phosphocholine (GPCCho(16:0/16:0)), and a tissue section obtained from Dr. Joe Hankin at the University of Colorado were used to test the efficacy of the prototype stage. The lipid standard was obtained from Avanti and used without further purification. The lipid was dissolved in 2:1 chloroform: methanol to produce 2 μ M concentration standard solution. A spin-coater was used to deposit the standard solution on a piranha etched 5 mm² silicon wafer. For both samples, the SIMS analysis was performed in the ToF-MS imaging mode using a continuous ion beam with a fluence of 3×10^{13} ions/cm². For both the thin film and the tissue section, the analysis started at room temperature. The stage was continuously cooled throughout the image acquisition. The temperature at the end of the analysis was 15 °C for the thin film and -50 °C for the tissue section.

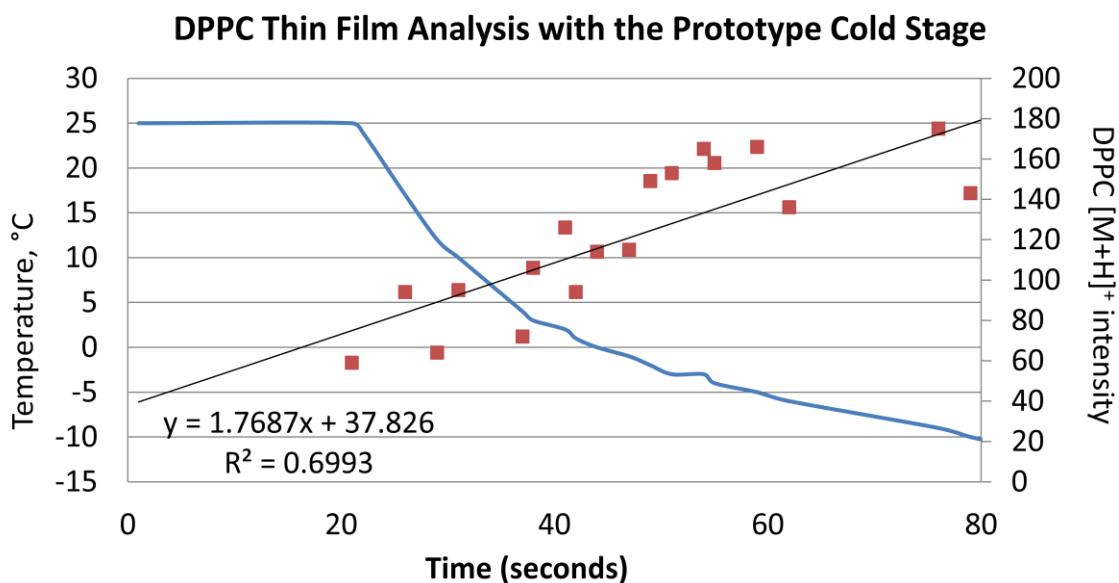


Figure 6.5. The prototype C₆₀-QSTAR cold stage was tested using a thin film of GPCho (16:0/16:0). The temperature and the integral intensity of the GPCho (16:0/16:0) protonated molecular ion peak at m/z 734.5 were recorded as a function of time. In approximately 1 minute, the stage temperature was reduced by 40 °C and the intensity of GPCho (16:0/16:0) was more than doubled.

In this investigation, the effect of temperature on the molecular ion sensitivity was tested using a single component lipid film. In Figure 6.5, the integral intensity of the GPCho (16:0/16:0) protonated molecular ion peak at m/z 734.5 and the stage temperature is plotted as a function of time. For the first 20 seconds, the stage and sample were at room temperature and the average molecular ion signal was approximately 80 counts per second. As the temperature of the sample was reduced, the molecular ion signal of GPCho (16:0/16:0) increased. At the end of the image acquisition, the average molecular ion signal more than doubled compared to the intensities obtained at room temperature. The increased sensitivity at low temperature

will be advantageous for future lipid and cell-based analyzes. However, more work is needed to achieve sample temperatures below $-150\text{ }^{\circ}\text{C}$ and obtain the full benefits associated with cryogenic-based investigations.

The prototype cold state was also used to image a coronal rat brain tissue section. The ToF-MS image in Figure 6.6 was acquired using the high resolution imaging stage rastering acquisition, discussed in Chapter 2. The left hemisphere of the brain section was imaged at room temperature and serves as an internal control. The stage cooling was initiated half way through the image acquisition, therefore the tissue was progressively cooled from room temperature ($25\text{ }^{\circ}\text{C}$) at the center of the tissue to $-50\text{ }^{\circ}\text{C}$ at the right edge of the tissue section.

The effects of cooling can be extrapolated by comparing the relative molecular ion intensity in the right and left hemisphere. All the glycerophospholipids, sphingomyelin and galactocerebrosides characterized in Chapter 4 were detected and their relative signal intensities were not significantly altered by the temperature change. However, the observed loss of the cholesterol signal during cooling was unexpected (see Figure 6.6, bottom left). Although the cholesterol signal localized to the white matter regions of the tissue section was greatly reduced by the cold temperature, the galactocerebrosides colocalized to these regions were not affected. In addition, a slight reduction in the intensity of the phosphocholine headgroup at m/z 184 was detected, despite a uniform distribution of the intact molecular ion species in the gray matter region. It would be interesting to see if the lost cholesterol signal intensity can be recovered when the tissue is brought back to room temperature.

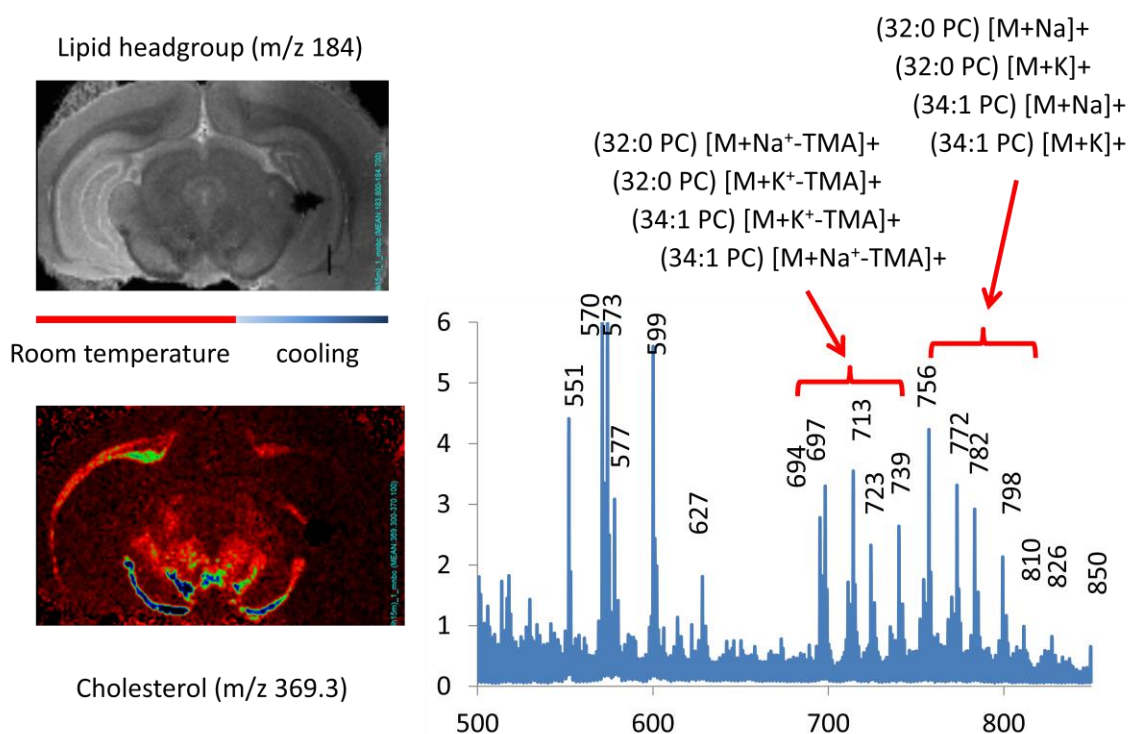


Figure 6.6. Preliminary data obtained analyzing a tissue section using the prototype C₆₀-QSTAR cold stage. The left hemisphere was acquired at room temperature; the right hemisphere was acquired at temperatures below 25 C. Below room temperature, the cholesterol signal disappeared.

Currently, ambient condensation occurring during the transfer of the sample to the mass spectrometer is problematic. This was avoided in these preliminary experiments since the samples were at room temperature at the start of the analyses then cooled. The seamless transmission of frozen sample into the instrument is needed for cellular samples. A glove box would provide a controlled environment, reduce any condensation related contamination and allow for the insertion of cryogenically fixed samples. The future installation of a glove box in the sample region of the C₆₀-QSTAR instrument should be beneficial in preserving cellular samples.

It is clear that cryogenic temperatures are needed to preserve the integrity of biological samples during SIMS analyzes. However, the effect of cold temperatures on

complex biological sample, not just single component films of select compounds, requires further investigation. The complex chemistry in various tissue microenvironments may alter relative ion intensities under cryogenic temperatures. The development of the cold stage and molecular depth profiling technique with regards to the C₆₀-QSTAR instrument is needed to improve the instrument's cell imaging capabilities.

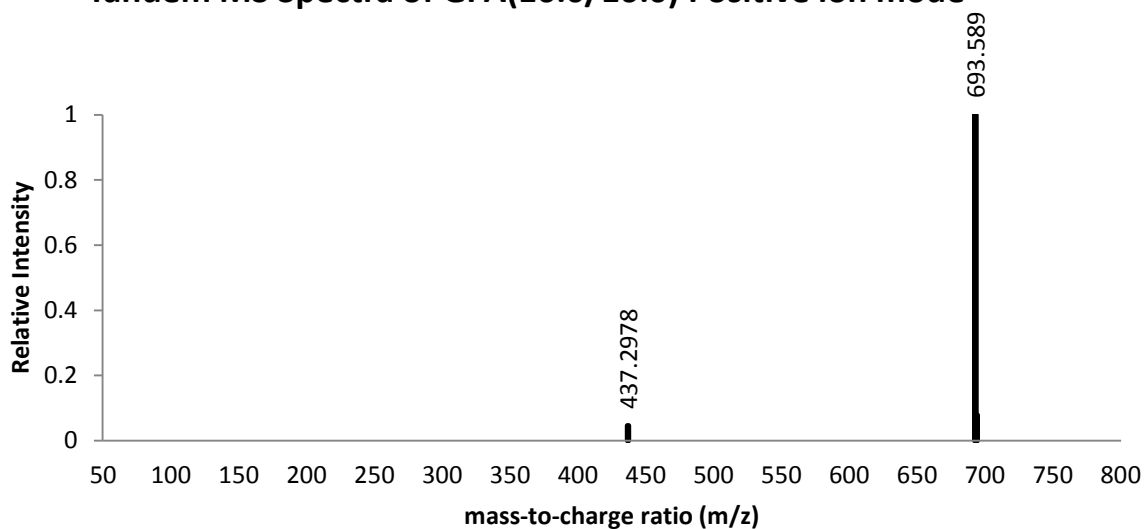
6.3. References

1. Cheng, J.; Kozole, J.; Hengstebeck, R.; Winograd, N., Direct comparison of Au-3(+) and C-60(+) cluster projectiles in SIMS molecular depth profiling. *Journal of the American Society for Mass Spectrometry* **2007**, *18* (3), 406-412.
2. Cheng, J.; Winograd, N., Depth profiling of peptide films with TOF-SIMS and a C-60 probe. *Analytical Chemistry* **2005**, *77* (11), 3651-3659.
3. Cheng, J.; Wucher, A.; Winograd, N., Molecular depth profiling with cluster ion beams. *Journal of Physical Chemistry B* **2006**, *110* (16), 8329-8336.
4. Chandra, S.; Bernius, M. T.; Morrison, G. H., Intracellular-localization of diffusible elements in frozen-hydrated biological specimens with ion microscopy. *Analytical Chemistry* **1986**, *58* (2), 493-496.
5. Chandra, S., Challenges of biological sample preparation for SIMS imaging of elements and molecules at subcellular resolution. *Applied Surface Science* **2008**, *255* (4), 1273-1284.
6. Kurczy, M. E.; Piehowski, P. D.; Parry, S. A.; Jiang, M.; Chen, G.; Ewing, A. G.; Winograd, N., Which is more important in bioimaging SIMS experiments-The sample preparation or the nature of the projectile? *Applied Surface Science* **2008**, *255* (4), 1298-1304.
7. Piwowar, A. M.; Fletcher, J. S.; Kordys, J.; Lockyer, N. P.; Winograd, N.; Vickerman, J. C., Effects of Cryogenic Sample Analysis on Molecular Depth Profiles with TOF-Secondary Ion Mass Spectrometry. *Analytical Chemistry* **2010**, *82* (19), 8291-8299.

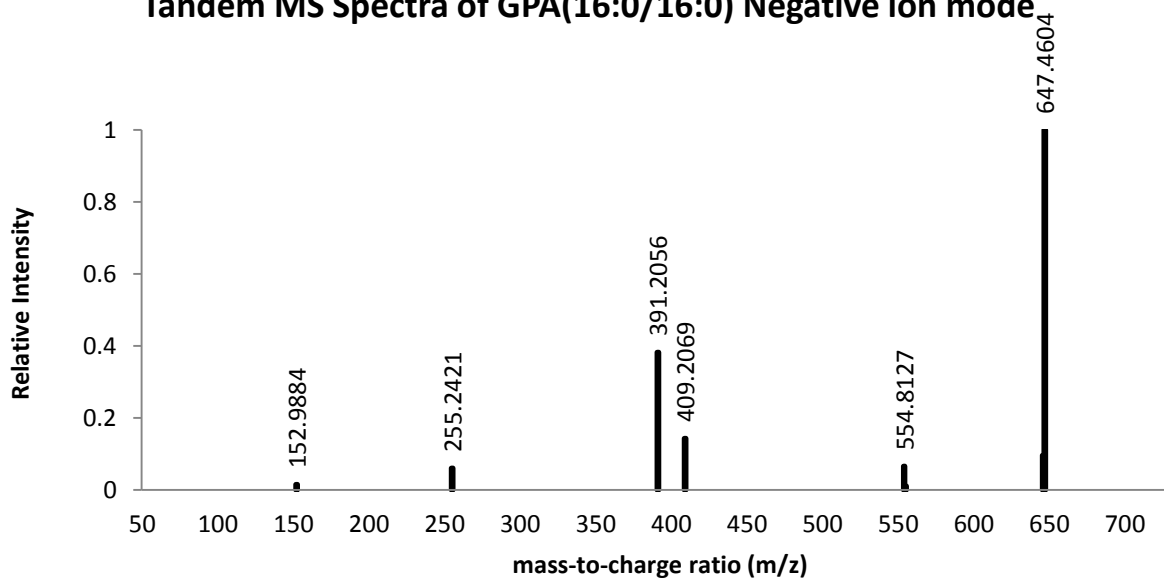
Appendix

Glycerophosphocholine Reference Spectra

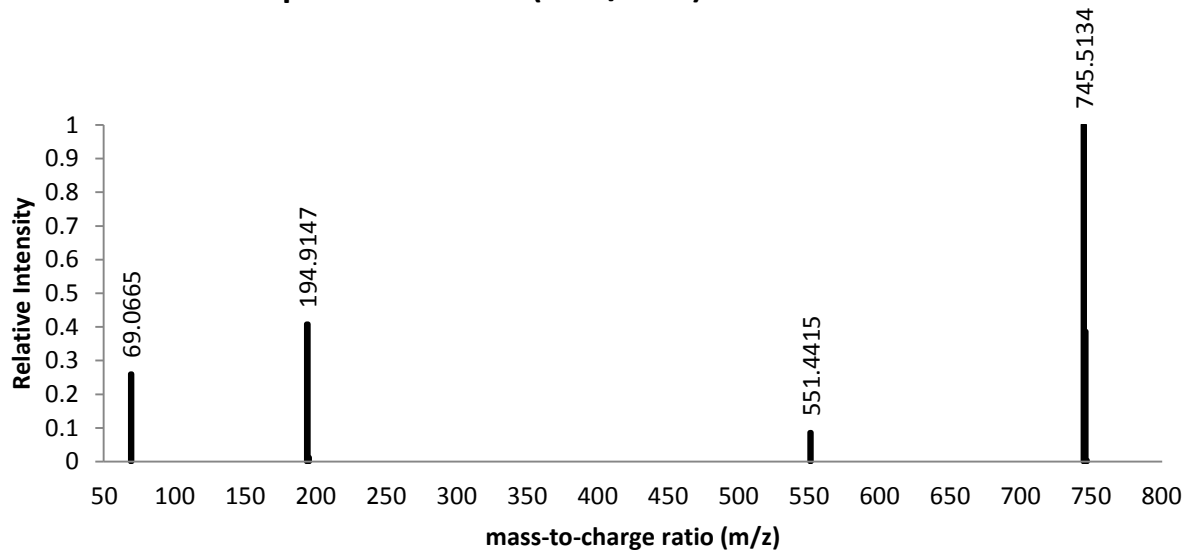
Tandem MS Spectra of GPA(16:0/16:0) Positive ion mode



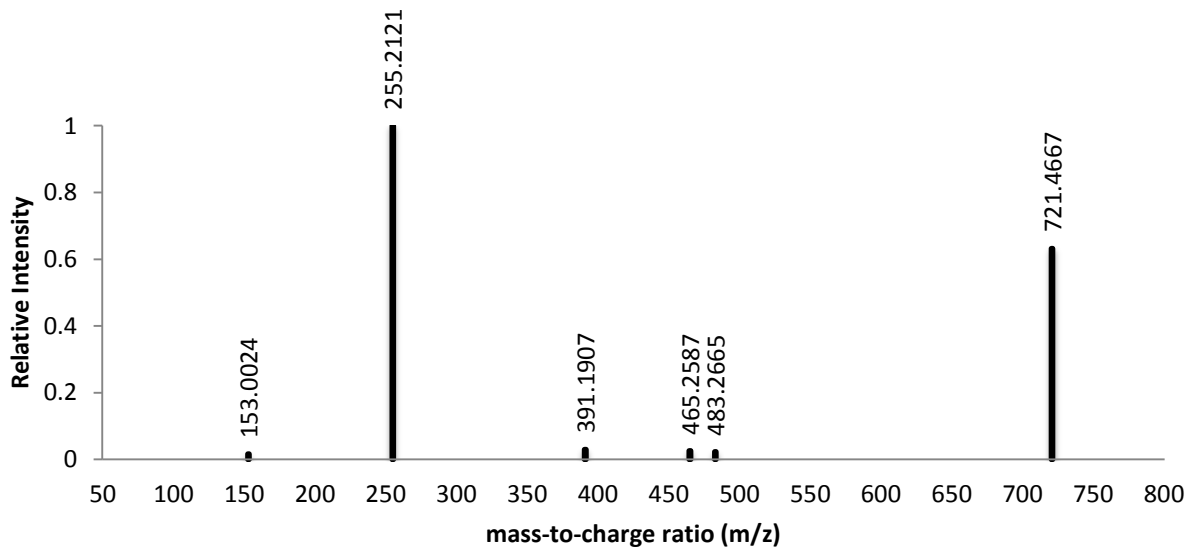
Tandem MS Spectra of GPA(16:0/16:0) Negative ion mode



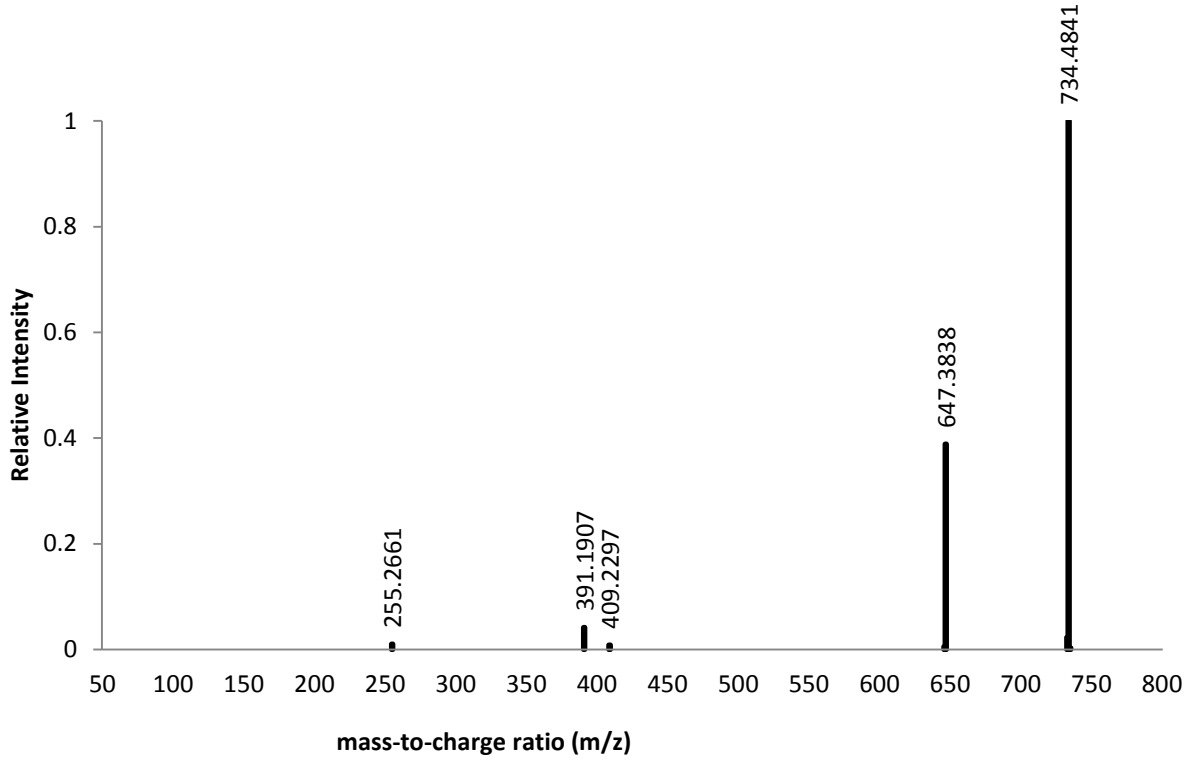
Tandem MS Spectra of GPGro(16:0/16:0) Positive ion mode



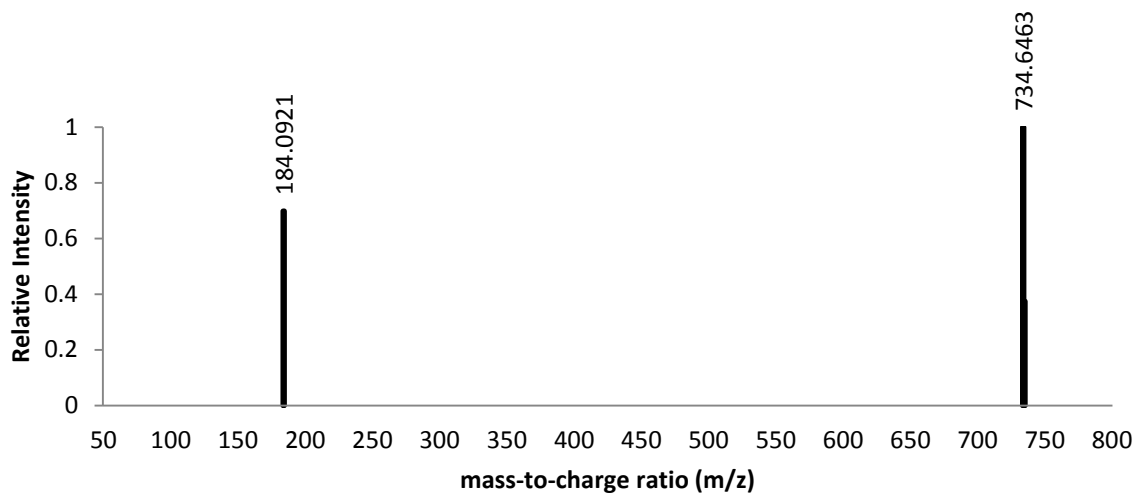
Tandem MS Spectra of GPGro(16:0/16:0) Negative ion mode



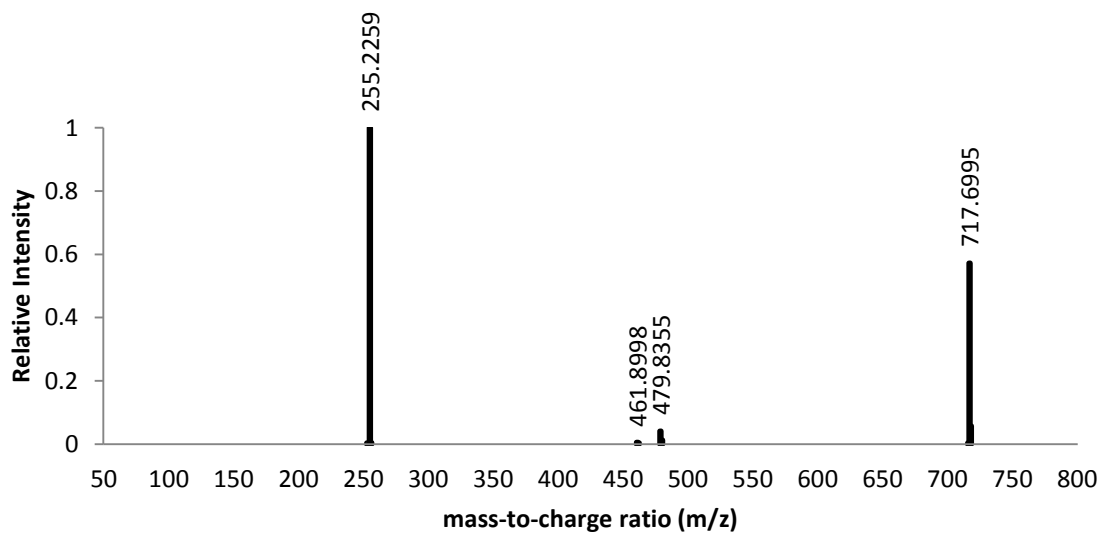
Tandem MS Spectra of GPSer(16:0/16:0) Negative ion mode



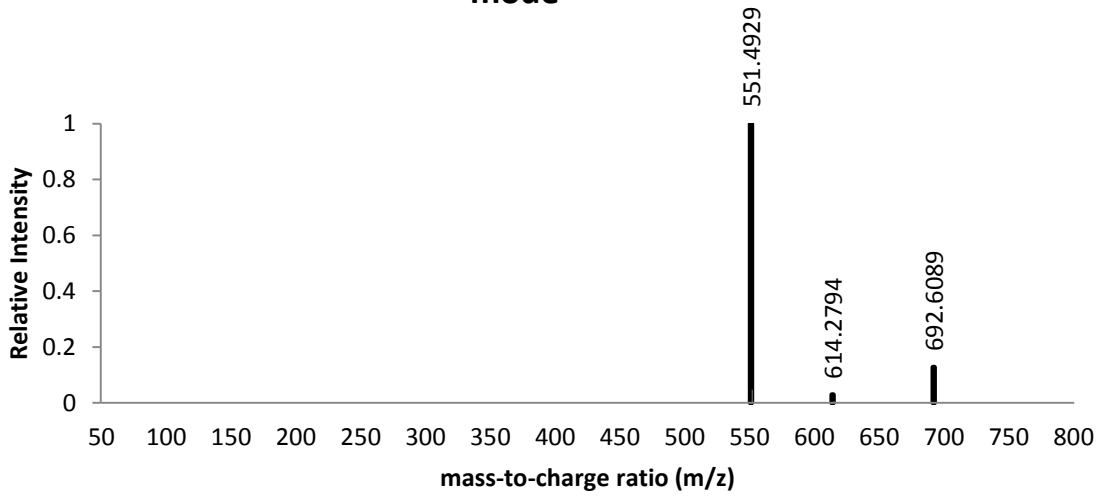
Tandem MS Spectra of GPCho(16:0/16:0) Positive ion mode



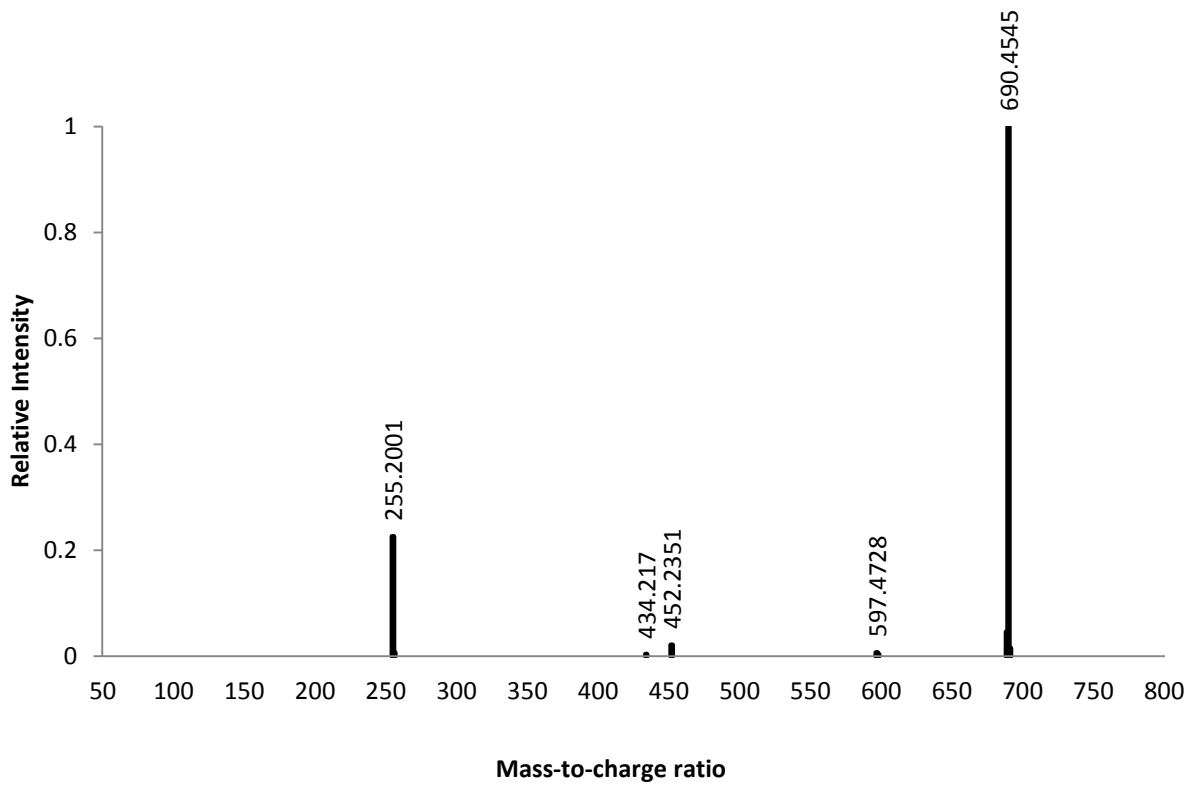
Tandem MS Spectra of GPCho(16:0/16:0) Negative ion mode



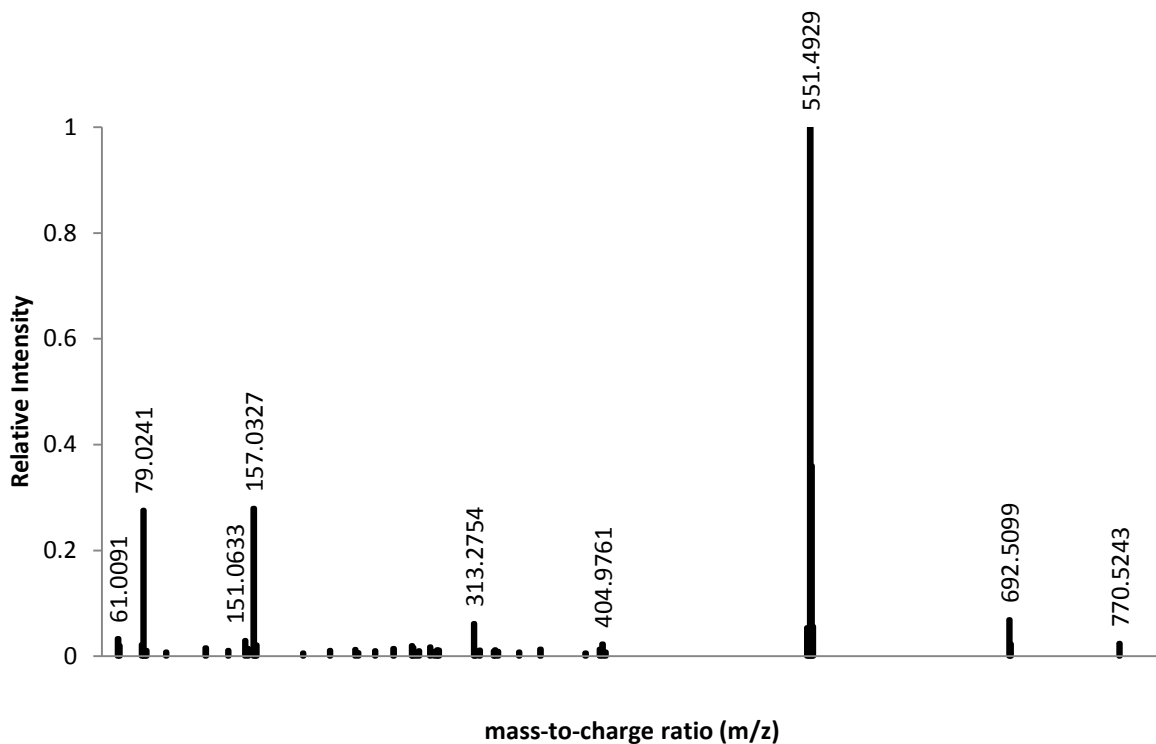
Tandem Spectrum of GPEthn(16:0/16:0) Positive ion mode



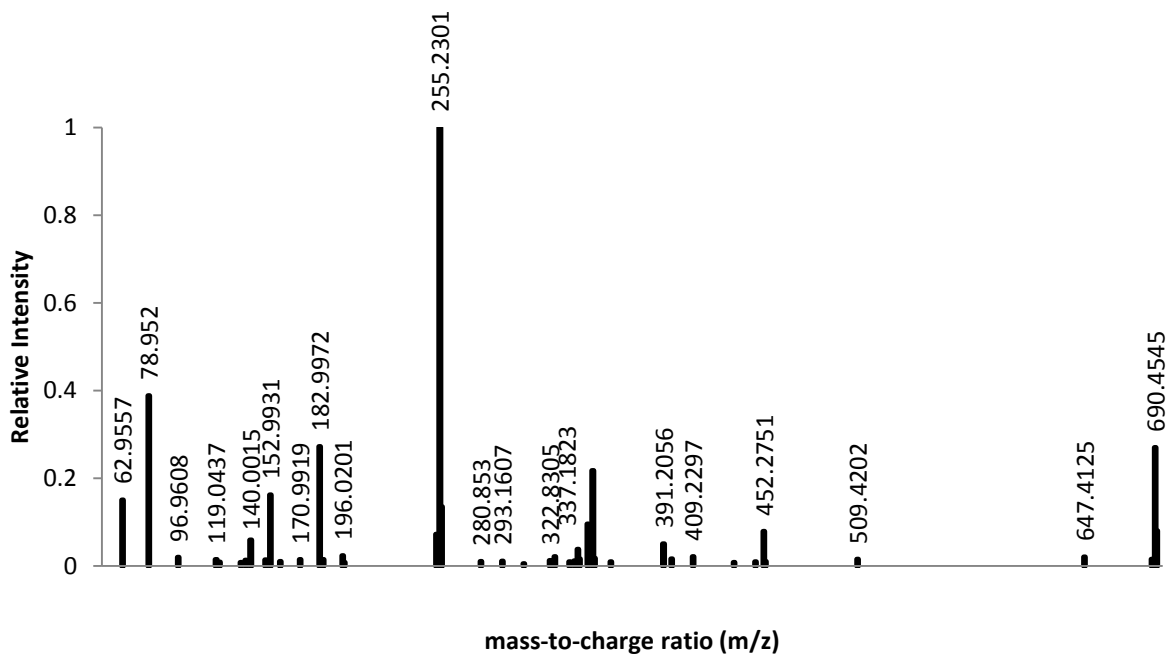
Tandem MS Spectra of GPEthn(16:0/16:0) Negative ion mode



ToF- MS Spectra of GPEthn(16:0/16:0) Positive ion mode



ToF- MS Spectra of GPE(16:0/16:0) Negative ion mode



VITA

Melissa Kathleen Passarelli

Melissa Passarelli, daughter of Nicholas and Kathleen Passarelli, was born and raised in Syracuse, NY. Graduated from Liverpool High School in 2001, she matriculated at Union College in Schenectady NY, where she earned a Bachelor of Science degree in Chemistry in 2005. She proceeded to The Pennsylvania State University in the summer of 2005 to conduct graduate research in the area of Analytical Chemistry with Professor Nicholas Winograd, and attained her Ph.D. in Chemistry in the Fall of 2011.